universität wien

DISSERTATION / DOCTORAL THESIS

Titel der Dissertation / Title of the doctoral thesis

"Biomimicry nano- and microparticles:
applications for peptide/protein delivery and encapsulation"

verfasst von / submitted by
Manuel Pascal Ernst Hafner MSc

angestrebter akademischer Grad / in partial fulfilment of the requirements for the degree of
Doktor der Naturwissenschaften (Dr.rer.nat.)

Wien, 2016 / Vienna 2016

Studienkennzahl lt. Studienblatt / Degree program code as it appears on the student record sheet:	A 796 605 419
Dissertationsgebiet lt. Studienblatt / Field of study as it appears on the student record sheet:	Chemie
Betreut von / Supervisor:	Univ.-Prof. Dr.rer.nat. Christian F.W. Becker

1 Summary

Nanoparticles for medical as well as biotechnological purposes have gathered an increasing amount of attention over the last 20 years. Nanoparticles are used for a multitude of applications such as drug delivery, enzyme stabilization and imaging. In this work we look at different variants of particle-peptide or -protein interaction to generate stabilized particle enzyme conjugates and understand the structural changes proteins undergo when interacting directly with nanoparticle surfaces.

Current biotechnological immobilization techniques are not suitable for most enzymes. Immobilization of enzymes on solid, removable supports often hampers the enzymes activity due to steric hindrances or negative effects on enzyme structure. We evaluated magnetic nanoparticles as a solid support for cellulase immobilization. Cellulase attached to nanoparticles would allow for pseudo-homogeneous catalysis while the magnetic properties of the nanoparticle material will provide an elegant possibility to remove the enzyme from the reaction. Attachment of the enzyme to the nanoparticle would be done by a small peptide with high affinity to magnetite nanoparticle surfaces. A number of peptides, covering the sequence of the magnetosome protein Mms6 found in the bacterium *magnetospirillum gryphiswaldense* was synthesized. Affinity of the peptides towards magnetite particles was tested in order to find the most promising candidate for an enzyme linker system. In addition to that attempts to produce recombinant variants of linker-cellulase conjugates were made.

In order to further the understanding of enzyme – nanoparticle interactions we designed a test system using cellulase and inorganic nanoparticles (magnetite and silica) of different sizes. Cellulase was directly adsorbed on the particles using a non-covalent method based on the protein corona effect. The protein corona effect describes the near irreversible adsorption of proteins and lipids to nanostructures. Cellulase adsorbing on nanoparticles is changed structurally resulting in a change of activity depending on nanoparticle material and size. Adsorbed cellulase interacts with free cellulase via protein-protein interactions, changing the free enzymes structure and activity. The extent of changes to cellulase structure and activity after adsorption on or interaction with nanoparticles is evaluated using several activity assays for different aspects of cellulase activity as well as circular dichroism to observe structural changes in the enzyme.

In addition to enzymatic adsorption on nanoparticles, the encapsulation of sample molecules in silica particles via a self-assembly method mimicking the shell formation of diatoms was evaluated. Using a silaffin derived synthetic peptide, R5-Cys, it is possible to precipitate silica microparticles from neutral solutions at room temperature and entrap the peptide within providing an elegant method to load particles with molecules at mild conditions in a controlled manner. Here we designed fluorescent labeled variants of the R5-Cys peptide to test internalization and release of R5-Cys in HT-29 colon cancer cells.

2 Zusammenfassung

Nanopartikel für biotechnologische sowie medizinische Anwendungen sind in den letzten 20 Jahren zunehmend in den Fokus der Forschung gerückt. Nanopartikel werden für gezielte Wirkstofffreisetzung, Enzymstabilisierung sowie die bildgebende Diagnostik verwendet. In dieser Arbeit untersuchen wir die verschiedenen Einflüsse, welche diese Partikel auf Proteine und Peptide haben, um stabilisierte Partikel-Enzym Konjugate zu produzieren sowie die strukturellen Veränderungen zu verstehen, die Proteine durchführen wenn sie mit Nanopartikeln interagieren. Zusätzlich werden wir dieses Wissen einsetzen um ein etabliertes Verfahren zur Produktion von Silicamikropartikeln mit eingeschlossenen Peptiden zu optimieren und seine Nutzbarkeit für eine gezielte Wirkstofffreisetzung zu zeigen.

Aktuelle Immobilisierungsverfahren in der Biotechnologie sind für die meisten Enzyme ungeeignet. Systeme zur Immobilisierung von Enzymen um diese Festphasen wiederholt verwenden zu können sind auf wenige Enzyme beschränkt die durch die Anheftung an solche Systeme keine negativen sterischen Effekte erfahren die sie in ihrer Aktivität einschränken. Ein Beispiel für eine mögliche Lösung dieses Problems findet sich in der Immobilisierung von Zellulase auf Nanopartikeln. Mit diesem System wird pseudo-homogene Katalyse ermöglicht. Immobilisierung des Enzymes auf magnetischen Nanopartikeln erlaubt eine einfache Entfernung des Enzyms aus der Reaktionslösung und somit ein elegantes System zu ihrer Wiederverwendung. Anbindung des Enzyms soll durch ein kleines Ankerpeptid ermöglicht werden, welches eine hohe Affinität für Magnetitoberflächen besitzt. Eine Reihe von Peptiden, welche die Sequenz des Magnetosom Membranproteins Mms6 aus *Magnetospirillum Gryphiswaldense* abdecken, wurde synthetisiert. Um den besten Kandidaten für ein Enzym-Linker System zu finden wurde die Affinität dieser Peptide zu Magnetit Nanooberflächen untersucht. Vielversprechende Kandidaten aus diesem Pool würden mit einem Zellulase Enzyme gekoppelt und Rekombinant als Testsystem exprimiert.

Um die Interaktion zwischen Enzymen und Nanopartikeln besser zu verstehen wurde ein Testsystem mit mehreren Nanopartikeln aus verschiedenen anorganische Materialen (Magnetit und Silica) und unterschiedlichen Größen entworfen. Unter Verwendung von Zellulase als Testenzym wurde ein Proteincorona basiertes Adsorptionssystem verwendet, um Zellulase auf verschiedenen Nanopartikeln zu immobilisieren. Zellulase welche auf diese Weise auf Nanopartikeln adsorbiert erfährt durch die hohe Oberflächenkrümmung der Partikel eine Veränderung der Struktur, was mit einer Veränderung der Aktivität einhergeht. Wie diese Änderung mit dem Material und der Größe der Partikel zusammenhängt, und ob die Änderung von Vorteil oder Nachteil für die Aktivität des Enzymes ist wurde mittels Zirkulardichroismus und verschiedenen Aktivitätsassays untersucht.

Zusätzlich zur Adsorption von Enzymen auf Nanopartikeln wurde die Verkapselung von Molekülen in Silicapartikeln mittels einer self-assembly Methode welche die Hüllenformierung der Kieselalge nachahmt untersucht. Unter Verwendung von R5-Cys, ein synthetisches Peptid welches auf dem Silaffin Protein der Kieselalge basiert ist es möglich Silicapartikel aus neutraler

Lösung zu präzipitieren und das R5-Cys Peptid dabei im Partikel einzuhüllen. Kovalente Anbindung des Wirkstoffs an das Peptid führt damit zu einem Einschluss des Wirkstoffs in die Partikel ohne komplexe Chemie unter voller Kontrolle der Aufnahme. In dieser Arbeit nutzten wir fluoreszenzmarkierte Partikel um die Internalisierung in HT-29 Darmkrebszellen zu zeigen, und einen gezielten Wirkstofftransport zeigen zu können.

Contents

2.1 Danksagung

Ich möchte diese Arbeit meiner Familie widmen, die mich in all den Jahren meines Studiums immer unterstützt hat, und besonders meinem Großvater Alois, der zu meinem großen Bedauern nur wenige Wochen vor der Fertigstellung dieser Arbeit verstarb und diesen Moment nicht mehr mit mir teilen konnte. Ich hoffe dass er und meine Großmutter nun an einem schöneren Ort mitfeiern.

Ich möchte zusätzlich meinen Dank all jenen Personen aussprechen die mir mit Rat und Tat zur Seite standen und mir unermüdlich ihr Ohr für offene Fragen und Sorgen liehen. Dr. Sophie Fröhlich, Dr. Helmuth Gehart, Dr. Zoraide Granchi, Dr. Florian Handle und Yasmin Fölser.

Ich möchte meinem Betreuer, Prof. Dr. Christian Becker für die Möglichkeit danken die spannenden und abwechslungsreichen Fragestellungen in dieser Arbeit verfolgen zu können. Darüber hinaus möchte ich mich für die Betreuung, die lehrreiche Zeit und die vielen Möglichkeiten die ich hatte bedanken. Mein Dank gilt auch meinen Kollegen die mich in der Zeit begleitet haben. Hier möchte ich besonders Dr. Manuel Brehs danken, der mit seinem Ratschlägen auch dann noch Hilfestellung leistete, als er schon eine neue Stelle in einem anderen Land angenommen hatte, Michaela Cherrier, ohne die ich die Wälder des Papierkrams an einer Universität sicherlich nicht sicher wieder verlassen hätte, und Prof. Christopher Gerner der immer ein offenes Ohr für meine Ideen hatte.

Mein Dank gilt außerdem der Firma Clariant GmbH & Co KG für die Unterstützung bei der Forschung der Mmms6 basierten Peptide, so wie den Kooperationspartnern Christian Roth, Patrick Schrepfer, Prof. Dr. Thomas Brück und Prof. Dr. Berensmeier für die gute Zusammenarbeit.

“If we knew what it was we were doing, it would not be called research, would it?”
- *Albert Einstein*

3 Cellulase adsorption on magnetite nanoparticles using new affinity tags derived from *magnetospirillum magneticum*

3.1 Introduction

3.1.1 Biotechnological Background

Even before understanding the concept of enzyme catalysis, humans took advantage of the catalytic power of enzymes, e.g. the ancient Egyptians who used different yeasts for beer fermentation and bread production or the Romans who used a similar concept to produce wine [2]. Today enzymes play an even larger role in biotechnology as potent biocatalysts, providing a high activity and specificity combined with a wide range of possible reactions. Using directed evolution and rational protein design it was possible to produce enzymes with higher activity more efficiently [3].

For many applications the use of enzymes in solution necessitates the removal of the enzyme after completion of catalysis. Methods that recover enzymes in high purity from complex reaction mixtures such as affinity chromatography or ultrafiltration are commercially not feasible for large scale production processes. In cases where the enzyme is used in solution the product is therefore separated and the remaining solution is discarded, requiring a new batch of enzyme for the next reaction. This is costly and time consuming. An alternative has been found in immobilization of enzymes on a solid support. This can be done using affinity based methods [4], via physical adsorption [5], covalent binding of enzyme to the solid support [6], by entrapment in a solid mesh [7] or affinity based methods [8]. Solid supports made of a large variety of materials such as natural polymers, synthetic polymers or inorganic materials (e.g. silica) are used as solids, gels or porous materials (Table 1). Immobilization of enzymes on a solid support offers several advantages depending on the method and the enzyme: heightened resistance to pH and temperature was reported [9], reusability of the enzyme is easily provided and even shortened reaction times have been seen for specific enzymes [10].

Enzymes with macromolecular substrates tend to loose activity after being immobilized on a solid support since the large substrate sterically challenges the immobilized enzyme. The attachment to a solid support that is several magnitudes larger than the enzyme itself introduces steric hindrances to the enzymes active site. Since the enzyme itself already needs to navigate along an already very large substrate an increase in steric hindrances results in a loss of activity [11]. This has prevented solid support based system from being implemented in reactions with large macromolecular substrates such as starch or hemicellulose-lignin-cellulose conversion. A possible new approach for enzyme recycling would therefore require to offer little to no steric hindrances and a property that will facilitate removal of the support. A possible candidate for this is magnetite nanoparticles with a peptide to enzyme anchor derived from the *magnetospirillum magneticum* bacteria.

Table 1: Overview of common enzyme immobilization systems in use

CATEGORY	MATERIAL	IMMOBILIZATION	ENZYME
NATURAL POLYMERS	*alginate*	entrapment	urease [12]
		entrapment	tannase [13]
	chitosan	covalent binding	endocellulase, pectinylase [14]
		affinity binding	hydantoinase [8]
	collagen	entrapment	tannase [15]
	carragen	entrapment	lipase [16]
	gelatin	entrapment	ß-D-galactosidase [17]
		entrapment	phenylalanine ammonia lyase [18]
	cellulose	covalent binding	fungi laccase [19]
		covalent binding	penicillin G acylase [20]
		covalent binding	glucoamylase [21]
		covalent binding	α-amylase [22]
		covalent binding	tyrosinase [23]
		covalent binding	lipase [24]
		covalent binding	ß-galactosidase [25]
	starch	entrapment	bitter gourd peroxidase [26]
		entrapment	urease [27]
		entrapment	fibrinolytic enzyme [28]
	pectin	entrapment	bitter gourd peroxidase [29]
		affinity binding	invertase [30]
	sepharose	physical adsorption	luciferase [31]
		physical adsorption	lactoperoxidase [32]
SYNTHETIC	*polyaniline*	physical adsorption	α – amylase [33]
POLYMERS	*PEG*	entrapment	activated sludge [34]
	polyurethane	physical adsorption	maltogenase [35]
	nylon-6	covalent binding	lipase [36]
	methacryl epoxy	covalent binding	α – amylase [37]
	PVC	covalent binding	cyclodextrin glucosyltransferase [38]
	PHBV	physical adsorption	lipase [5]
INORGANIC	*magnetite*	covalent binding	Streptokinase [39]
MATERIALS	*zeolites*	physical adsorption	α-chimotrypsin [40]
		physical adsorption	lysozyme [41]
	ceramics	physical adsorption	lipase [42]
	celite	entrapment	ω-transaminase [43]
		covalent binding	lipase [44]
	silica	entrapment	urease [45]
		physical adsorption	α - amylase[46]
		covalent adsorption	lignin [47]
	glass	entrapment	cytochrome cd_1 nitrite reductase [48]
		entrapment	urease [49]
	activated carbon	physical adsorption	cellulase [50]
		physical adsorption	acid protease [51]
	charcoal	physical adsorption	urease [52]
		physical adsorption	amyloglucosidase [53]
		physical adsorption	papain [54]

3.1.2 Magnetotactic Bacteria

Magnetotactic bacteria, such as *magnetospirillum magneticum*, are a polyphyletic group of aquatic prokaryotes first discovered 1963 by Salvatore Bellini [55] and rediscovered 1973 by P. Blakemore [56]. They are found at the oxic/anoxic interface of water columns with vertical chemical stratification in sediments of freshwater, brackish marine and hypersaline habitats around the world [1]. Occurrence and distribution of magnetotactic bacteria is linked to these chemical gradients as the bacteria mostly reside in thin layers at the chemical interface. Here they can find reductants and oxidants for growth in abundance [57]. Despite their polyphyletic nature they have some common features; they are exclusively gram negative, motile, show negative tactic/growth response to atmospheric levels of oxygen and possess a unique organelle called magnetosome [58]. The magnetosome consists of a crystalline magnetic core made from magnetite, an iron oxide with the formula $Fe^{II}(Fe^{III})_2O_4$, surrounded by a phospholipid bilayer containing a large number of unique membrane proteins. The majority of genetic information of these magnetosome proteins is arranged in clusters conserved throughout all magnetotactic bacteria [59]. The relative proximity of all these clusters advocate their arrangement in genomic islands used for horizontal gene transfer [60]. Early experiments suggest the development of the magnetosome as a single event that was spread via horizontal gene transfer to all magnetotactic bacteria [61]. This model is further underlined by the often observed spontaneous loss of magnetosomes of magnetotactic bacteria in culture [62].

Magnetotactic bacteria use the magnetosome to exert their common ability, magnetotaxis. Magnetotaxis describes the ability to orient and move oneself within the magnetic field of the planet earth [63]. The bacteria use this orientation to position themselves at optimal spots along the oxic/anoxic gradient, where the majority of the bacteria resides slightly below the oxic/anoxic interface while a minority can be found towards at comparatively anoxic conditions [57]. Contrary to the logical assumption that magnetotactic bacteria would seek iron rich environments to help magnetosome production, the preferred ratio of reductants/oxidants along the oxic/anoxic interface is a stronger drive than the available amount of iron [64]. Schüler et al. could show that contrary to what would be expected, magnetotactic bacteria can only tolerate extracellular iron concentrations from the micromolar to low millimolar range, suggesting that they accumulate iron against a large concentration gradient [65]. Magnetotactic bacteria could even be found in highly alkaline habitats such as in Mono Lake, California, where iron concentration is limited by its poor solubility at high pH [66].

Magnetotactic bacteria need to orient and migrate towards optimal conditions along the oxic/anoxic interface. This three-dimensional location problem can be reduced to a two-dimensional one by using magnetosomes to orient themselves along the earth's magnetic field lines. Except at the equator all magnetic field lines on earth are slightly tilted, going to as much tilt as 90° directly at the poles. Orientation along the field lines therefore means going up or down. Using its cilia the bacterium can now move up or down its aqueous environment along the oxic/anoxic gradient to its preferred gradient position [67]. Magnetic properties of the magnetosome align it perfectly parallel to the magnetic field lines. Observed preference of magnetotactic bacteria movement downwards could be verified by the predominantly north

seeking bacteria in the northern hemisphere and the equally predominantly south seeking bacteria in the southern hemisphere [67a, 68]. This preference alone however, offers an incomplete explanation for the optimal positioning of the bacterium along the oxic/anoxic gradient. Movement of the bacterium towards higher oxygen levels would lead to death, movement towards low oxygen levels reduces growth. A method of movement in both directions would be a more logical solution. The preferred movement hypothesis resulted from observation in the water droplet test. In this test a small water droplet is formed, containing enough bacteria to further analyze them under the light microscope. It could be shown that movement direction preference is strictly correct only under the oxic conditions of the water droplet test. Frankel et al. showed that exposure to reducing conditions reversed north seeking bacteria to south seeking and short wavelengths of light (<500 nm) could switch them back to north seeking [67c]. This led to the more refined polar magneto areotaxis model where flagellar rotation is adjusted depending on the oxygen and light levels to position the bacterium at the optimum gradient level for growth. This explanation is further strengthened by the observation that magnetotactic bacteria in culture with homogeneous oxygen levels loose this preference altogether [69].

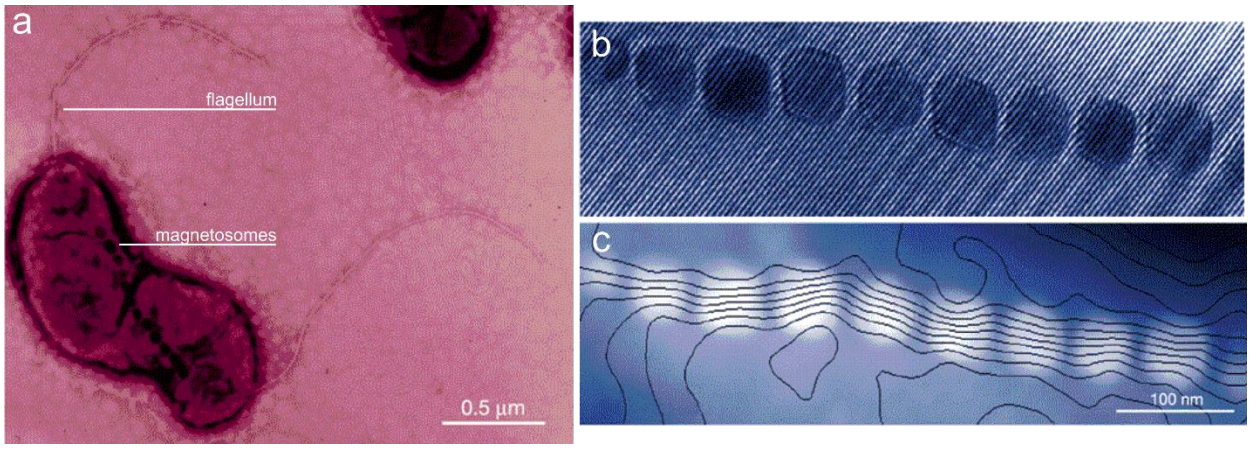

Figure 1: a) Transmission electron micrograph of a negatively stained cell of typical magnetotactic bacterium MV-4, a marine magnetotactic spirillium. It has a flagellum at each end of the cell and a chain of electron dense, magnetite-containing magnetosomes along the long axis of the cell. b) Close up of the magnetosome with electron interference pattern c) magnetic field lines derived from the interference pattern superimposed on the positions of the magnetosomes. The arrangement of the field lines within the magnetosomes is indicative of single magnetic domains and shows that the chain of magnetosomes acts as a single magnetic dipole. [1].

In order to orient themselves along the magnetic field lines against external forces, magnetotactic bacteria need to align their magnetosomes in a chain of organelles resembling a pearl necklace [63, 70]. This distribution aligns the magnetic dipole moments of each magnetosome parallel to the others in order to sum up the permanent magnetic dipole moments of the individual particles (Figure 1) [71]. With this enhanced magnetic dipole moment, the bacterium is able to surpass the thermal and kinetic forces of its aqueous surroundings by aligning itself strongly with the geomagnetic field. This does not accelerate or pull the cell towards the magnetic field but only orients it along it [67c]. Dead bacteria are still aligned along the magnetic field but do not move. One can therefore picture the bacterium as a self-propelled small compass needle. Since the magnetic properties of the bacteria organelles are not responsible for its movement the word magnetotaxis is indeed wrong and misleading.

3.1.3 Magnetosomes

Magnetosomes are organelles uniquely found in magnetotactic bacteria. They consist of a magnetic crystal that is encapsulated by a phospholipid membrane containing several unique magnetosome membrane proteins (Figure 2) [72]. The magnetic core of the magnetosome is either composed of magnetite $Fe^{II}(Fe^{III})_2O_4$ or, less frequent, greigite $Fe^{II}(Fe^{III})_2S_4$. Unlike magnetite found in rocks, the crystals found in magnetosomes have nearly perfect uniform crystallinity and size distribution depending on the specific bacterium between 35 and 120 nm and close to no variation within the species [73]. In order for them to function as magnetic organelles for orientation they need to be so called single magnetic domains.

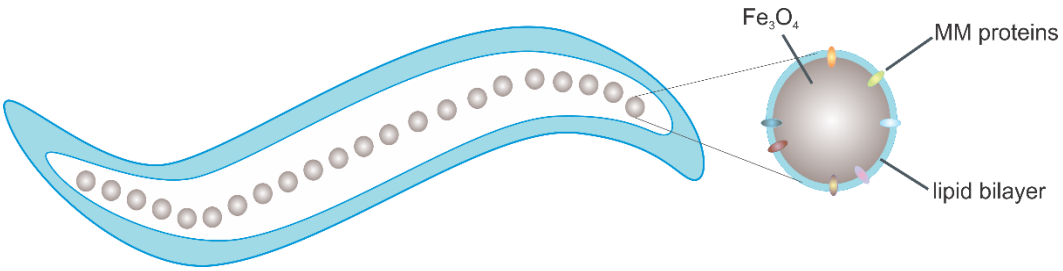

Figure 2: Schematic of a magnetospirillum magneticum bacterium with an enlarged view of a single magnetosome

A single magnetic domain is a term used in magnetism and describes a particle or object with only one single magnetic state. Change in magnetic orientation with a single magnetic domain is therefore only possible by rotating the whole object by 180 ° in the magnetic field. Single magnetic domains have a very high coercivity; the resistance of a permanent magnet to cancellation of its magnetic properties in a given magnetic field [74]. This safeguards the magnetosomes from being demagnetized as well as making them universally useful regardless of the orientation of the magnetic field. Using single magnetic domains the magnetotactic bacteria can move in both directions of the magnetic field easily. Objects being single magnetic domains need to be very small in diameter, 100 nm at max [75].

Single magnetic domains, as the smallest building block of a magnet, are rather weak by themselves. In order to maximize magnetic strength of the single domains, magnetosomes are aligned in a row. This arrangement allows the magnetotactic bacterium to combine the strength of all single magnetic domains. One single magnetic domain alone would not be sufficiently strong to allow the cell to orient itself in the geomagnetic field against other external forces.

The magnetite crystals in the magnetosome are tightly defined in size, morphology, crystal structure and their chainlike arrangement in the cell [72a]. To achieve this uniform particle shapes, crystal formation must be tightly controlled in a complex mineralization process. More than 20 different membrane proteins have been identified as players here [72a, 76]. The encoded proteins have been named using different nomenclatures, the most prominent ones magnetosome membrane proteins (Mam), magnetite proteins (Mps or Mag) and magnetic particle membrane specific proteins (Mms).

The current state of research provides the following picture of the general formation process of the magnetosome (Figure 3): The proteins Mms 16, MpsA and Mms24 are part of a cascade that initiates invagination of the inner membrane to start formation of a magnetosome [60, 77]. These newly formed invaginations are aligned and fixed using the actin-like protein MamK

as chain and MamJ as the anchor protein [78]. MagA and MamN work as proton transport proteins that adjust pH in the magnetosome upon particle formation in the case of MamN and organize the transport of Fe^{2+} in the vesicle in the case of MagA[77a]. Mms6 is then starting the formation of the actual magnetic single domain within the fully formed vesicle [79]. Mms6 is not only reported to have a large role in crystallization control but also as a protein found tightly attached to the particle itself [79-80]. This led to the assumption that certain sequence motifs of the protein might have a heightened affinity towards magnetite surfaces

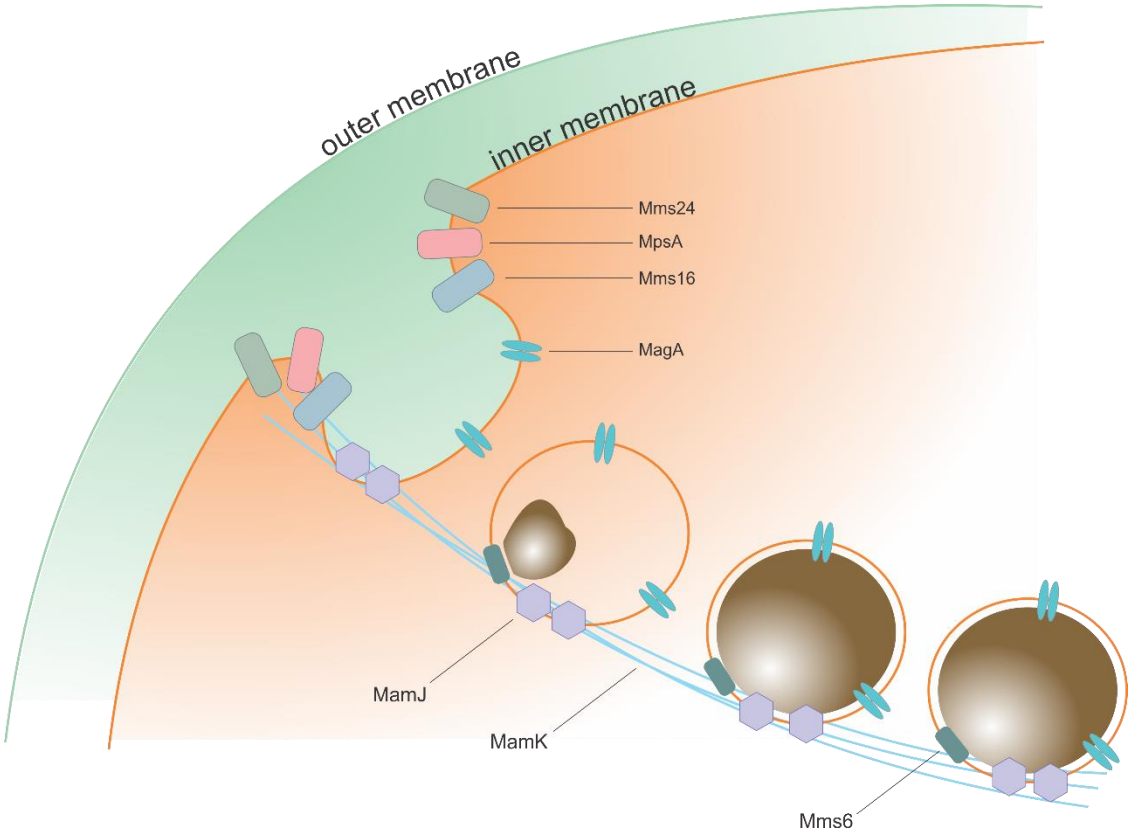

Figure 3: Schematic of hypothesized magnetosome bio-mineralization. Mms24, MpsA and Mms16 start the invagination of the inner membrane forming a new magnetosome hull. MagA starts accumulating iron ions in the vesicle, MamJ attaches it to the MamK chain and Mms6 starts formation of magnetic single domains in the formed vesicle.

3.1.4 Mms6 protein

The Mms6 protein was first discovered by Arakaki et al. in 2002 while examining the crystal membrane of the magnetospirillum magneticum AMB-1 strain [79]. It is an amphiphilic protein consisting of a hydrophobic N-terminal region and a highly acidic hydrophilic C-terminal region. It was discovered along two very similar proteins called Mms5 and Mms7 and encoded close to a third protein Mms13 with little sequence similarity to the other three [79]. All of them are located in the *magnetospirillum magneticum* magnetosome island [76, 81]. Mms5, 6 and 7 have a common sequence motif: LGLGLGLGAWGPXXLGXXGXAGA (Figure 4), whereas Mms13 shows only slight similarities in the C-terminal region. The acidic C-terminal region is considered to attract and bind iron ions and to act as the starting point of magnetite single domain particle formation [79].

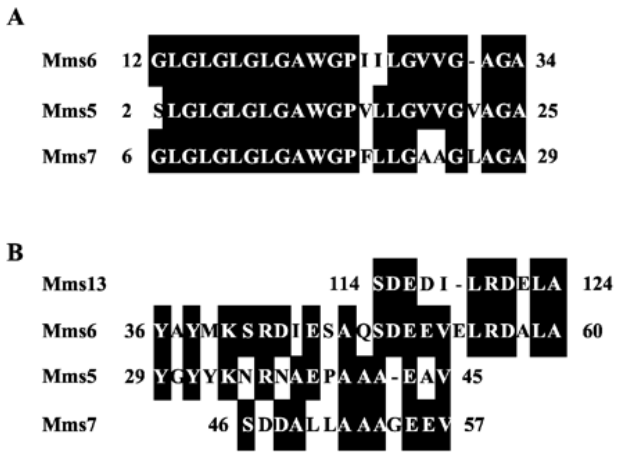

Figure 4: Comparison of the amino acid sequences of the proteins Mms5, Mms6, Mms7 and Mms13. Conserved regions are boxed. The numbers represent amino acid positions in the mature proteins. A) hydrophobic region, B) hydrophilic region [79].

Indeed Mms6 tends to aggregate in aqueous solutions due to the hydrophobic interactions caused by the repetitive N-terminal LG motif [80a, 82]. Mms6 in solution is not present as a monomer, instead the 10.2 kDa protein shows spontaneous self-assembly and formation of micelles of 20-40 proteins with an average size of 25-150 nm [83]. The micelles shape and form are in line with theoretical assumptions based on the corona-core model of block polymers and have been verified via small-angle x-ray scattering [84]. The core consists of the hydrophobic N-terminus that assembles in the micelle to a central hydrophobic part surrounded by the hydrophilic outer part of the assembled proteins. Presence of high amounts of iron results in further aggregation behavior as the micelles form tight discs of single micelles or structures similar to a mass fractal structure (Figure 5) [84].

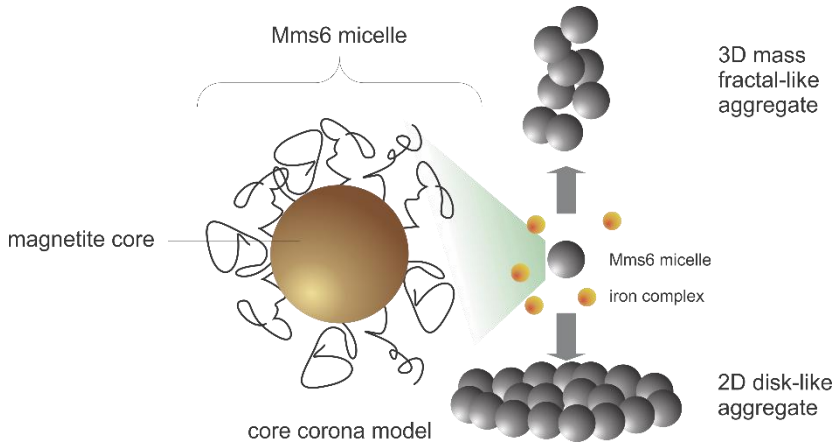

Figure 5: Schematic of the core-corona model for block polymers. An inner block and a rather unstructured outer shell comprise the resulting micelle. Addition of iron starts assembly towards either flat disk-like aggregates or fractal-like ones [84].

Within these micelles Mms6 attracts and binds Iron and starts a particle assembly process, where shape, size and morphology of the resulting particle is tightly controlled (Figure 6) resulting in particles with identical characteristics [82]. Bacteria deficient of Mms6 still show particle formation but the formed particles are smaller and have no defined uniform shape and morphology [80b].

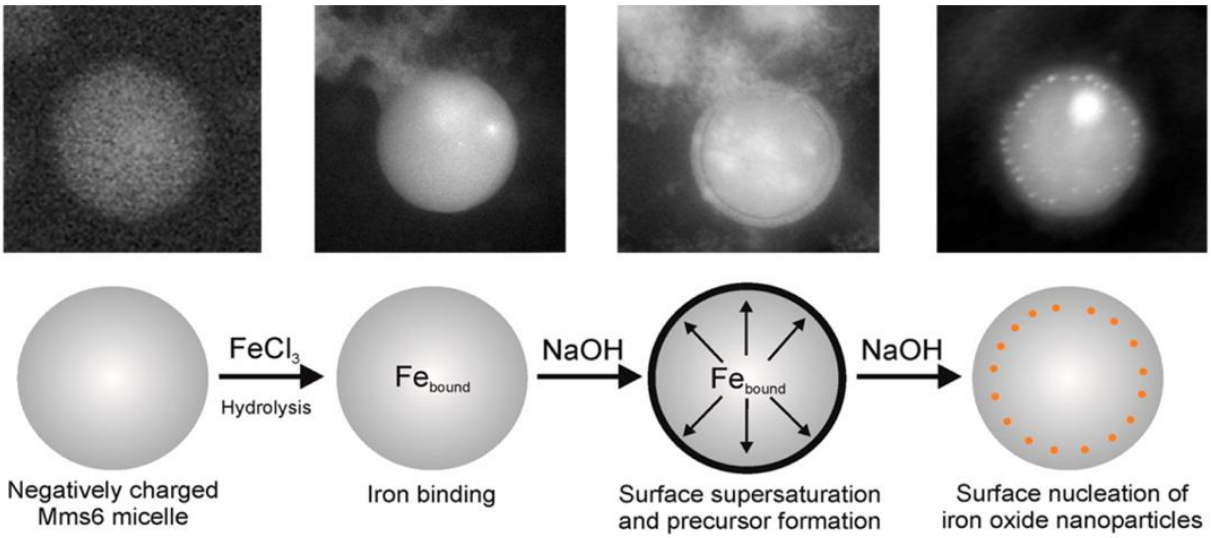

Figure 6: (Top) Schematic and high angle annular dark field scanning transmission electron microscopy (HAADF-STEM) of Mms6 mediated magnetite particle formation. The negatively charged Mms6 micelle attracts iron ions, saturates itself and initiates nucleation at the inner surface of the micelle [83c].

Nucleation with NaOH mediated precipitation is occurring exclusively within the Mms6 micelles during mild precipitation conditions using ferric chloride as iron source [83c]. Surprisingly Mms6 is capable of producing particles using other materials than iron as well as producing defined structural arrays. Mms6 mediated controlled assembly of particles made of cobalt ferrite or cobalt doped magnetite was reported *in vitro* as well as its ability to produce magnetic nanoparticle arrays [80a, 85].

3.1.5 Proof of principle enzyme: cellulase

An important enzyme for biotechnological applications (see chapter 3.1.1) is cellulase. Cellulase was chosen to be the model enzyme to be attached to the Mms6 based anchor. Cellulose, the substrate of cellulase, is the most abundant and most difficult to process carbon source on the planet. This is due to it is complete insolubility in water in its native form of hydrogen-bonded crystalline fibers [86]. It is the most stable and resistant natural organic compound known with a half-life of several million years. Because of its striking stability it tends to accumulate in the environment, making it a valuable and important carbon resource [87]. This makes it important for biotechnological applications that require large amounts of cheap sugar e.g. ethanol production. Hydrolysis of cellulose is done by cellulase enzymes but due to their demanding and unique mode of catalysis it was impossible to attach them to a solid support without significant loss of activity so far.

Cellulose is a linear, insoluble biopolymer composed of glucopyranose linked by ß-1,4 glycosidic bonds. Because of that, and in contrast to most other glucose polymers such as starch and callose, the repeating unit is not glucose but cellobiose [88]. This results in unique structural properties as native cellulose is partly crystalline, organized in microfibrills out of 15-45 linear polymer chains and amorphous regions without the rigid crystalline structure (Figure 7).

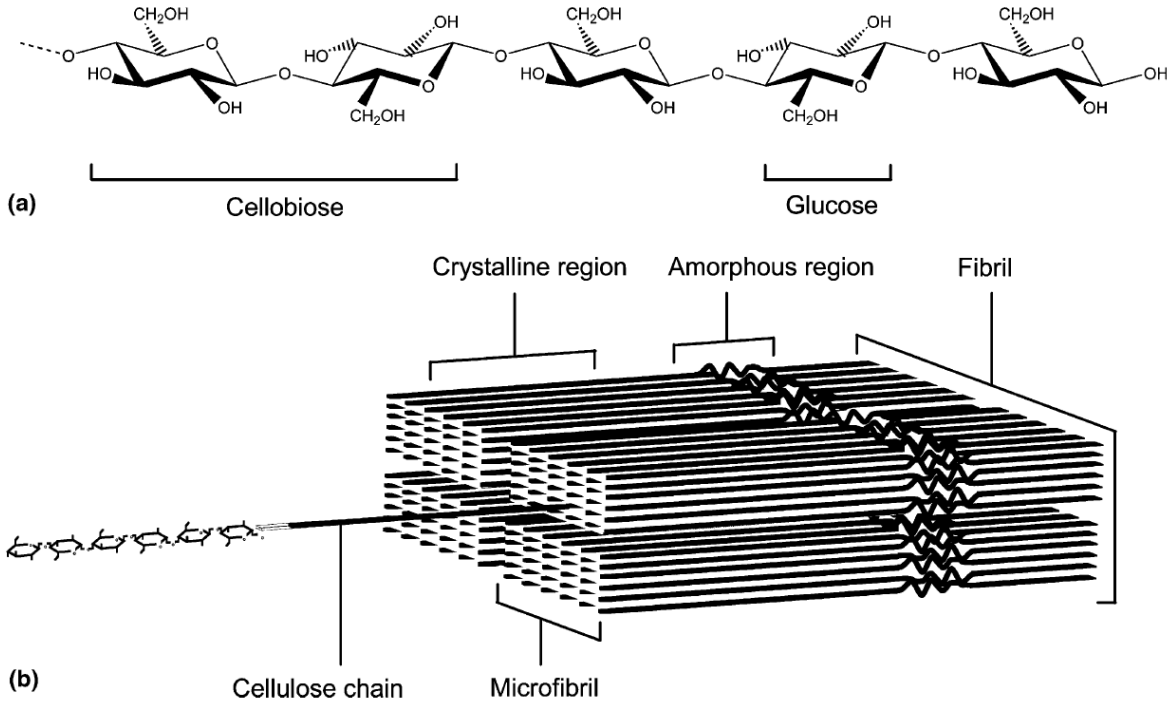

Figure 7: Structural features of cellulose: a) scheme of the primary structure. b) scheme of the structure of a cellulose fibril. With permission from [88]

Cellulases are a large and diverse superfamily of hydrolases that are used by bacteria and fungi to break down cellulose. Basically they all catalyze the same reaction, the hydrolysis of ß-1,4 glycosidic bonds. Depending on how the substrate is processed, the family of cellulases can be divided in three groups: endoglucanases, exoglucanases and ß-glucosidases [88-89]. Endoglucanases possess an open active site, allowing them to attach on the more amorphous non crystalline parts of cellulose and randomly cleave the polymer [90]. This produces open ends of either reducing or non-reducing sugar chains. Exoglucanase with its tunnel like active site is now able to attach to these loose ends and hydrolyze the chain into small glucose dimers[91]. These dimers, called cellobiosides are attacked by ß-glucosidase and cleaved into single glucose units. Cellulases in general need a non-catalytic binding molecule that attaches them to the insoluble cellulose polymer and brings them close to their actual substrate, the ß-1,4 glycosidic bond. This binding domain is attached to the enzyme via a small unstructured linker and called carbohydrate binding molecule (CBM) [92].

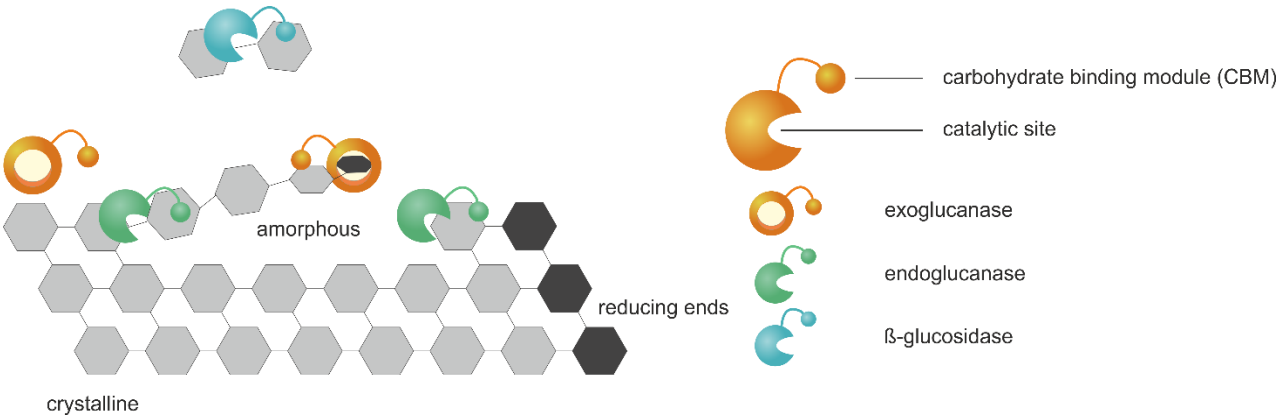

Figure 8: working scheme of free cellulase activities. Endoglucanases produce open detached polymer ends by randomly cleaving the polymer at the amorphous region of the cellulose. These open ends are attacked by the exoglucanase that processes along the strand. This lets the amorphous structure widen into the crystalline parts. Exoglucanase cleaves of small cellobiosides that are then hydrolyzed into glucose by ß-glucosidase. The free glucanases all consist of a catalytic site attached to a carbohydrate binding module (CBM).

Aerobic species secrete an array of different cellulase enzymes from their cytoplasm. Since they are unable to internalize large insoluble polymers they require this approach to break down the polymer outside of the cell and internalize the sugars after catalysis. Anaerobic species mostly secrete large (MW >1 million Da) enzyme complexes, where single enzymes most of the time lack a CBM and are bound together by a scaffoldin protein complex that has the required CBM domain (Figure 9)[93]. The complete nature of this cellusome complex is not yet understood. The cellusome complex is most likely associated with extracellular protuberances on cellusome producing bacteria. It consists of a fibrillary protein, scaffoldin, that contains sites for the cellusomal enzyme subunits, called cohesins. The enzymatic subunits have several catalytic activities of the endoglucanase and exoglucanase variety as well as a cohesion-binding site called a dockerin. Composition of the cellusome differs greatly between different species due to the fact that scaffoldins contain up to nine different cohesins with binding capacity for 26 different cellusomal enzymes so far discovered [94].

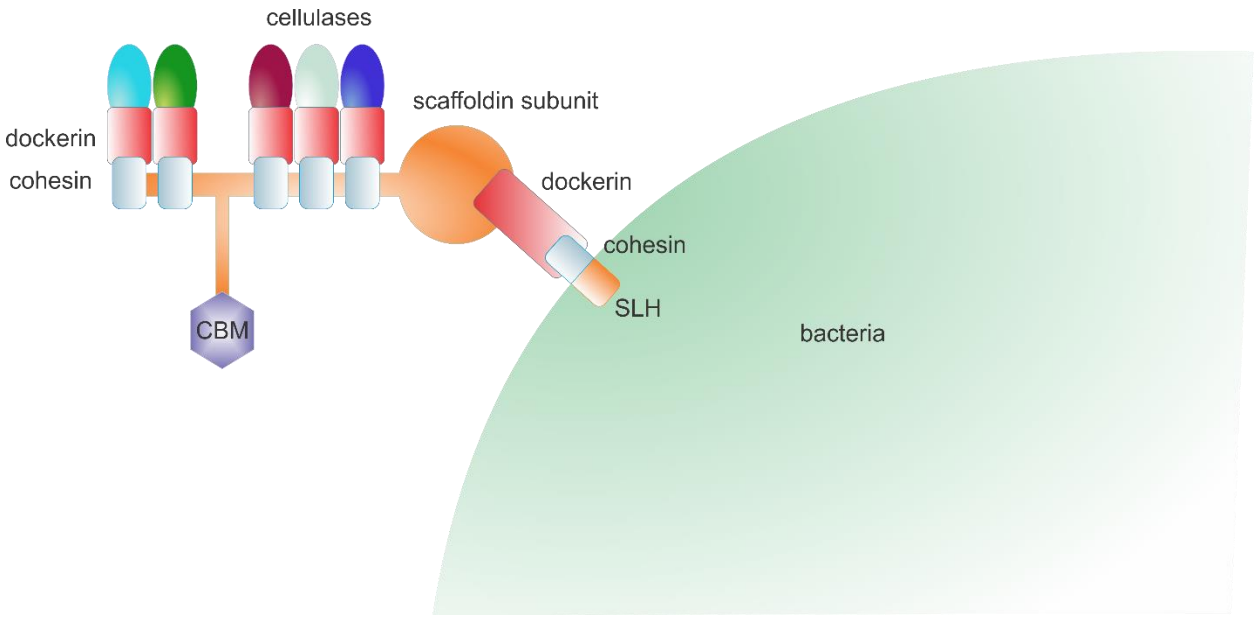

Figure 9: Schematic represenation of a cellusome. The cellusome complex is attached to the surface layer protein surrounding the bacteria via the surface layer homology domain (SLH). The SLH is attached to a cohesin that is again attached to a scaffoldin subunit via a dockerin. The scaffoldin subunit hosts several cellulases of the endogulcanase, exoglucanase and ß-glucanase variety, attached to the scaffoldin subunit via cohesin/dockerin. The subunit has a carbohydrate binding molecule (CBM) attached to it as well that locates the cellusome to cellulose.

The cellulase used in this work originates from *Fervidobacterium islandicum* a gram-negative anaerobic bacterium that uses a cellusome complex to break cellulose into its monomeric component, glucose. The enzyme used is an isolated version of *fervidobacteriums* endoglucanase and shows endoglucanase and ß-glucosidase activity.

Due to the large volume, resistant structure and heterogeneity of the cellulase polymer, kinetic studies with full cellulase are complicated and obtaining reliable, reproducible results presents itself as challenging [95]. Assays with smaller, homogeneous substrates are therefore used to obtain kinetic data of cellulase enzymes with Michaelis Menten characteristics. For this work, a colorimetric ß-D glucosidase assay was used as well as the carboxymethylcellulase (CMC) for endoglucanase activity. The CMC assay uses a linear, non-crystalline cellulase polymer to simulate the amorphous region of the native crystalline cellulase. This reduces variation due to heterogeneous substrate compositions leading to better assay results.

3.1.6 Aim

Here we aim to design a magnetic nano-support for immobilization of cellulase enzymes. Using nanoscale solid supports might enable the transition from heterogeneous catalysis at the interface of solution and solid, to a pseudo homogeneous catalysis reaction. Nanoparticles are ideal systems for pseudo-homogenous catalysis due to the high surface to volume ratio and small size. Depending on particle diameter and enzyme molecular weight they contribute negligible steric hindrances. This could make the catalysis of reactions with macromolecular substrates possible. Using non-toxic magnetic materials such as magnetite it should be possible to produce enzyme-nanoparticle conjugates that can be reused several times. Magnetite was chosen to be able to remove it from the reaction via magnetic separation. Using a magnetic separator, built from a mesh in the flow stream with an attached electromagnet, the enzyme-nanoparticle conjugate can be separated from the reaction mixture for repeated reuse (Figure 10).

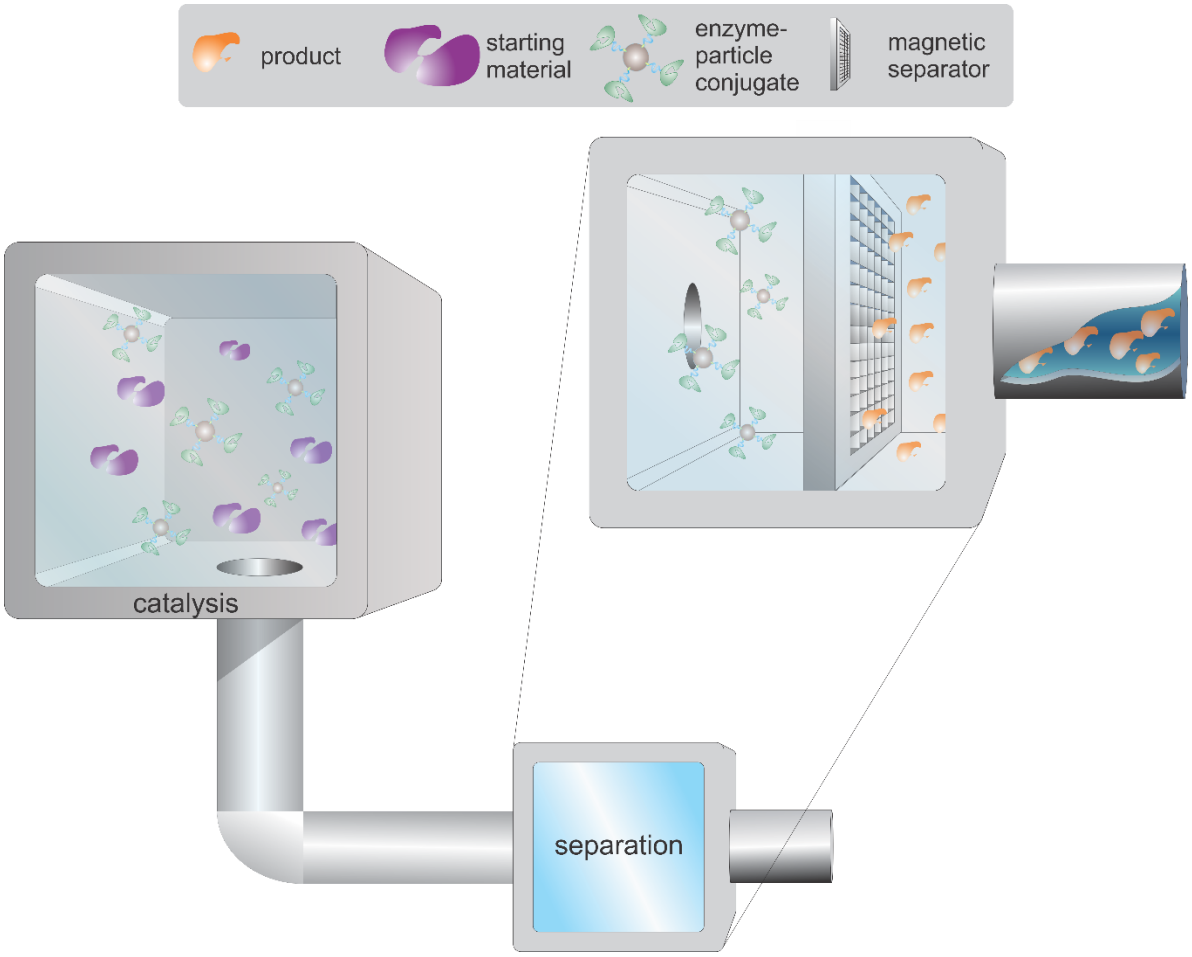

Figure 10: Proposed setup for pseudo-homogeneous catalysis. The enzyme-particle conjugate catalyzes hydrolysis of cellulose in a reaction chamber. The reaction mixture containing enzyme and product is then flushed through a magnetic separator in a separate separation chamber that uses an electromagnetic net to precipitate the enzyme-particle conjugate, leaving only the product in the solution. The enzyme-particle conjugate is then flushed out and reused by removing the magnetic field from the separator.

An ideal immobilization technique will provide a genetically encodable, targeted method of anchoring without loss of enzyme activity. In addition to that recombinant expression of an anchor-enzyme conjugate should be possible for mass production. Mms6, with its reported direct attachment to small magnetite nanoparticles, seems an ideal candidate for linking enzymes to such nanoparticles by genetic fusion of Mms6 or parts of it to the target enzyme. Here we aim at exploring the affinity of Mms6 fragments to magnetite particles. We evaluated several small peptides based upon the sequence of the Mms6 protein. Using these small peptides we will determine which part of the protein is responsible for the affinity towards the magnetic nanoparticle surface. This small peptide will then be used as the linker fused to the enzyme. As a commercially and environmentally interesting test system, the cellulase based conversion of cellulose to monomeric glucose is used as model enzyme system.

3.2 Material and Methods

3.2.1 Chemicals

If not otherwise noted all chemicals were purchased from Sigma Aldrich, St. Louis, Missouri, USA. T4 Polynucleotide Kinase (10 U/µl), ATP, nuclease free water, restriction enzymes for NotI, SalI and BseYI and corresponding buffers were all acquired from New England Biolabs, Ipswich, MA, USA. All amino acids were bought from Novabiochem, Darmstadt, Germany.

3.2.2 Devices

All peptides, if not otherwise mentioned, were synthesized using a Tribute peptide synthesizer from Protein Technologies Inc. Tucson, USA. All dynamic light scattering experiments were done using a Zetasizer Nano ZS from Malvern Instruments Ltd., Malvern, UK. Fluorescence microscopy was done using an Axioskop 40 from Carl Zeiss AG, Oberkochen, Germany. HPLC analysis was done using a DIONEX Ultimate 3000 µHPLC System from Thermo Fischer Scientific Inc., Waltham, Massachusetts, USA using analytical Kromasil C4 columns (150 x 4.6 mm, 5 µm particle size) from Sigma Aldrich, St. Loius, Missouri, USA. Gel documentation was done using a ChemiDoc MP from BioRad Laboratories Inc., Hercules, California, USA. Mass spectrometry analysis as well as peptide purification was done using an AutoPurification HPLC/MS system from Waters Corporation AG, Wilford, Massachusetts USA and preparative Kromasil C4 HPLC columns (250 x 21.2 mm, 5 µm particle size) from Sigma Aldrich, St. Loius, Missouri, USA. Cell disruption was done using a TS cell disrupter from Constant Systems, Northants, UK. Incubation was done in a HT Multitron from Infors, Bottmingen, Switzerland.

3.2.3 Peptide synthesis

Manual peptide synthesis of peptide 7 was done using fluoromethoxycarbonyl (Fmoc) solid phase peptide synthesis (SPPS) [96] on a 0.2 mmol scale using preloaded Fmoc-Ala-Wang-polystyrene (Fmoc-Ala-Wang-PS). Deprotection of the N-terminal Fmoc group was done incubating the resin twice with 20 % (v/v) piperidine in DMF for 3 and 7 min respectively. For each amino acid coupling 2.5 eq. of the corresponding Fmoc-amino acid were activated with 2.38 eq. HBTU and 5 eq. DIEA for 3 min and added to the resin for 30 min. Between coupling and deprotection steps the peptidyl-resin was washed with DMF. Amino acid side chains were protected by standard protecting groups except for lysine 2, 3 and 4 which were protected with the Mtt protecting group. PPO coupling was done on resin by removing the Fmoc protecting group as described earlier. 10 eq. of succinic anhydride in a solution of 0.5 M HOBT in DMF was added for 30 min. After washing with DMF a solution of 0.5 M CDI in DMF was added to the resin for 30 min. After washing with DMF a solution of 0.5 M HOBT in (4,7,10)-trioxa-1,13-tri-decanediamine was added to the resin for 30 min. Palmitoyl coupling was done directly after the corresponding protected lysine was coupled and deprotected. The resin was washed with DCM thoroughly for 30 min. A mixture with 20 eq. palmitoylchloride, 20 eq. HOBT, and 22 eq. trimethylamine in a mixture of 3/1 DCM/DMF was prepared. Palmitoylchloride and HOBT were added first and triethylamine with one minute delay. Coupling was done by incubating the mixture with the resin overnight. NBD coupling was done by removing the corresponding protection group and adding a solution of 2 eq. NBD in DMF with 1 % DIEA (v/v) for 60 min. After

completion of peptide synthesis the N-terminal Fmoc group was removed, the peptidyl resin was washed with DCM dried under vacuum. Overall deprotection and cleavage of peptides from resin were achieved with a cleavage cocktail out of 5 % TIS, 2,5 % ddH_2O and 92.5 % TFA 4 h at RT. Crude peptides were precipitated by addition of cold diethyl ether and subsequent centrifugation. Precipitated peptides were washed twice with ether and after removal of the supernatant dissolved in 50 % acetonitrile in water and finally lyophilized.
All other peptides were synthesized with a peptide synthesizer using Fmoc-SPPS in 0.2 mmol scale. All peptides were synthesized using preloaded Fmoc-X-Wang-polystyrene (Fmoc-X-Wang-PS) resin, where X stands for the first, C-terminal, amino acid of the sequence. The synthesizer uses the same chemistry as the manual synthesis. Peptide 2 was provided by coworkers.

3.2.4 Affinity assay

Adsorption of peptides onto nanoparticles was done by using 2 mg/ml solutions of the corresponding peptides in 20 mM Tris/HCl buffer with pH 7.8. 100 µl of the peptide solution was incubated with 100 µl of a 1 mg/ml magnetite or silica particle suspension in water for 30 min while shaking. After centrifugation (5 min 14,000 rpm), the supernatant was collected and analyzed using HPLC (C4 column 5-65% acetonitrile in 30 min) and protein content was evaluated by peak integration in comparison to an equal volume of 2 mg/ml reference solution. In the case of lipidated magnetite nanoparticles the centrifugation time was 30 minutes. Lipidated particles were produced according to a procedure described elsewhere [97].

3.2.5 Synthetic magnetite nanoparticles

Synthetic nanoparticles of 11 nm primary particle size were synthesized by partners at TU München, AG Sonja Berensmeier [98]. Synthetic nanoparticles precipitated in the presence of peptide 4 were produced as follows:

0,5 mmol $FeCl_2$ and 1 mmol $FeCl_3$ were dissolved in 1 ml degassed water spiked with argon gas. To 100 µl of the solution in a round flask under argon atmosphere the following were added to a final volume of 400 µl depending on experiment: 100 µl of a 20 % (w/v) Pluronic F-127© in ddH_2O solution, 100 µl of 20 mg/ml sodium-oleate in ddH_2O, 4 or 100 µl 2 mg/ml Peptide 4 in ddH_2O. A drop of 1 M HCl was added to set the beginning pH acidic. 1 M NaOH was added while shaking heavily until the solution turned from yellow to green/brown and dark nanoparticles started to precipitate. The heavier the shaking the smaller the agglomerates. The supernatant was removed after magnetic sedimentation of the magnetite using a strong neodymium magnet and the particles were washed three times with water. The supernatant was then analyzed using HPLC as described before and the particles were characterized using DLS

3.2.6 Expression of cellulase

Cellulase was expressed using the pET24-cellulase plasmid in *E.coli* BL21 DE3 bacteria. Bacteria were cultured to a final volume of 2 liters TB medium (all % (w/v); 1.2 % tryptone, 2.4% yeast extract, 0.4 % (v/v) glycerin, 10 % (v/v) 1 M potassium phosphate buffer pH 7 all in water) with 0.1 % (w/v) kanamycin. Culture was incubated till an OD of 0.8 was reached. Main culture was induced with 0.1 % (v/v) of 1 M IPTG solution and incubated for 4 h at 37 °C while shaking at 150 rpm. Bacteria were harvested by centrifugation at 4500 rpm for 30 min at 4 °C. Supernatant was discarded and the pellet was resuspended in 1x PBS buffer at pH 7.5 and treated with a cell disrupter at 1.89 bar. Enzyme was purified using a NiNTA column (application 1x PBS at pH 7.5, elution with a gradient of 0 mM to 500 mM imidazole in 1x PBS pH 7.5. Final product was dialyzed against 1xPBS pH 7.5

3.2.7 Cloning experiments

All cloning and consecutive workup was done using restriction enzymes and buffers from New England Biolabs, Ipswich, MA, USA and PCR purification kits from Qiagen, Hilden, Germany. Cloning was done using *E.coli XL-1 (blue)* bacteria strains.

3.2.7.1 Oligo Cloning

Complementary single strand DNA with the Peptide 4 sequence was bought from VBC biotech, Vienna, Austria.

Sequence 1

TCGACGTGTACGCCTATATGAAAAGCCGTGATATTGAAAGCGCACAGAGTGATGAAGAGGTTGAACTG CGTGATGCACTGGCA**GC**

Sequence 2

GCACATGCGGATATACTTTTCGGCACTATAACTTTCGCGTGTCTCACTACTTCTCCAACTTGACGCACTAC GTGACCGT**CGCCG**

Prior to usage the DNA was phosphorylated using T4 Polynucleotide Kinase (10 U/µl) along with 10-50 pmol DNA sample and 10 mM ATP in nuclease free water. The DNA was added to 2 µl of the ATP solution along with 1 µl of the T4 polynucleotide kinase. Sample was brought to 20 µl volume with nuclease free water, mixed thoroughly, spun down briefly and incubated at 37 °C for 20 min. Kinase was then inactivated at 75 °C for 10 min. Annealing is done by dissolving both DNA single strands 1:1 in annealing buffer (1 mM Tris, pH 7.5-8.0, 50 mM NaCl, 1 mM EDTA in nuclease free water), heating them at 95 °C for 2 min and then letting them slowly cool to room temperature over at least 45 minutes. This is best done by turning off the Thermomixer and letting the tube cool to room temperature in the cooling heat block without the lid on. This will take at least 50 minutes. Afterwards the hybridized DNA was stored at -20 °C.

3.3 Results and Discussion

3.3.1 Testing Mms6 based peptides for their affinity to magnetite particles

In order to test affinity towards magnetite nanoparticles we used two different particle variants. Magnetite nanoparticles were produced using a alkaline precipitation method described elsewhere [99]. Untreated blank magnetite nanoparticles of 11 nm primary particle size and magnetite particles with an oleic acid lipid bilayer in order to simulate the natural phospholipid bilayer present in native magnetosomes were tested [97b]. We compared the ability of Mms6 peptides 1-5 to bind specifically to these two types of nanoparticles and compared their adsorption efficiency to two non Mms6 based peptides 6 and 7 (Figure 11). Peptide 6 was used as a negative control and is a peptide that has no sequence resemblance to the Mms6 variants but is of a similar size (3450.79 Da, versus the size of the Mms6 variants from 1761.82 to 3022.52 Da). 7 is a short lysine rich peptide equipped with a polyethyleneglycol polyamide oligomer (PPO) chain [100] and two palmitoyl residues. The palmitoyl moieties are used to enhance interaction with the oleic acid lipid membrane. The PPO group is added to counteract the reduction in hydrophilicity that the two palmitoyl groups introduce and the 7-nitrobenzofuran (NBD) fluorescence dye is used as a suitable label. Peptides 1-7 were synthesized according to the procedures outlines in chapter 3.2.3. Analytical data for the syntheses are found in the appendix. Peptide 2, 3 and 5 are hard to synthesize due to their high hydrophobicity, resulting in poor purification yields.

In order to check for magnetite nano-surface specificity of the Mms6 variants we checked adsorption on 11 nm magnetite particles, 13 nm lipidated magnetite particles and silica particles with 12 nm primary particle size as a negative control. Lipidated magnetite particles are covered by a lipid membrane of oleic acid to mimic the native membrane shell of the magnetosome. Peptides were adsorbed according to the procedure explained earlier.

native GGTIWTGKGLGLGLGLGLGAWGPIILGVVGAGAVYAYMKSRDIESAQSDEEVELRDALA

1 GLGLGLGLGLGAWGPIILGVVGAGA

2 ESAQSDEEVELRDALA

3 GGTIWTGKGLGLGLGLGLGAWGPIILGVVGAGA

4 VYAYMKSRDIESAQSDEEVELRDALA

5 GLGAWGPIILGVVGAGAVYAYMKSRDIESA

6 CTQSNEITIPVTFESRAQLGGPEAAKDSETAAK

7 CGGKGKAAKKA-[PPO]$_3$-A

NBD, Palm, Palm

NBD = 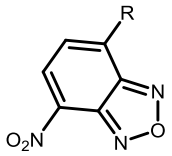

Palm = 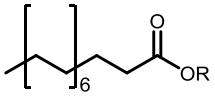

Figure 11: Sequences peptide 1-7. NBD = 7-nitrobenzofuran fluorescence label, palm = palmitoyl moiety, $[PPO]_3$ = polyethyleneglycol polyamide oligomer trimer. Peptide 6 is a negative control peptide.

Magnetite as well as silica nanoparticles have the tendency to form large, unstructured and random sized agglomerates in aqueous solvents [101]. This tendency of particle materials with oxygen rich surfaces needs to be taken into account when experimenting with nanoparticles. In order to obtain particle suspensions with smaller and less polydisperse particle populations, different sonication times were evaluated prior to the experiments. Sonicating for at least one minute reduced size and heterogeneity of agglomerates significantly by 59 % as well as a drop of polydispersity index by 43 % (Figure 12). This effect is reversible and the particles agglomerate again within 20 minutes to more than 100 % of the original size. Increase in size is most probably due to the local increase in temperature during the sonication process, promoting the agglomeration processes typical for these materials. Sonication times of at least two minutes result in a drop of average agglomerate size of 67 % and polydispersity was reduced by 71 %. The reduction in polydispersity also reverses to original levels in 40 minutes. The reduction of polydispersity hints at the destruction of agglomerates whose size deviates from the average first. Taking these results into account sonication of 2 minutes was applied to all further experiments and the experiment itself was done as quickly as possible directly after sonication.

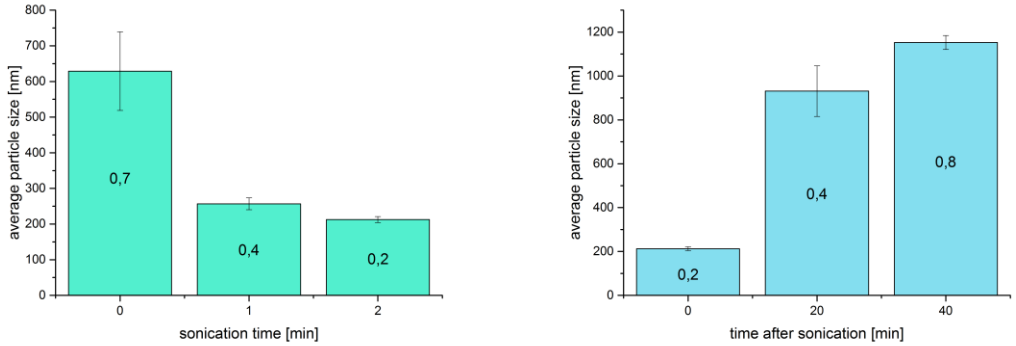

Figure 12: Influence of sonication on particle agglomeration and polydispersity of magnetite nanoparticle preparations. Values in the column bars represent polydispersity values of the corresponding sample. n=3.

Adsorbed peptide was determined indirectly by measuring peptide content in the supernatant of the particle suspension after 30 minutes incubation with the peptide. The difference between initial peptide concentration and concentration in the supernatant was used to calculate the peptide adsorbed onto the nanoparticles. Attachment of the peptide to the particle is proposed to happen via the acidic parts of the peptide, making peptides 2 and 4 the most likely candidates to adsorb with high affinity [102]. Highest affinity is seen at the DEEVE part of the sequence with the glutamic and aspartic acid groups interacting with the iron ions. (Figure 13). Surprisingly the probability of the peptide chain carbonyl to interact with the iron is higher than that of the acidic side chains. The hydrophobic section of the Mms6 protein is thought to introduce the protein into the membrane of the growing magnetosome.

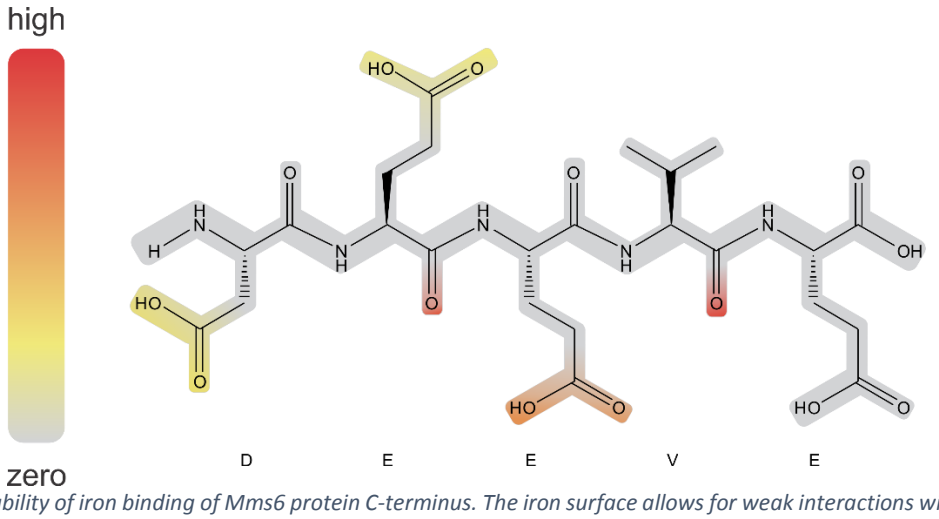

Figure 13: Probability of iron binding of Mms6 protein C-terminus. The iron surface allows for weak interactions with hydroxyl and carboxyl groups of the protein or peptide fragment. Reproduced with permission from [102]

Adsorption experiments of peptides 1-7 on different kinds of nanoparticles (Figure 14) however, give results not in line with one previous assumption. The least polar parts of the Mms6 protein have the highest affinity towards magnetite particles (variants 3 and 5), whereas the acidic variants 1 and 4 have up to 55% less adsorption compared to peptide variant 5. Adsorption values of peptide 6 are comparable to that of 1 and higher than those of 4. The adsorption of Mms6 peptides on magnetite nanoparticles with or without a lipid bilayer or on silica nanoparticles is within the same range for most of the peptide variants. A clear preference of the Mms6 peptide variants for magnetite over the silica particles could not be found, questioning the assumption of Mms6's affinity towards magnetite surfaces.

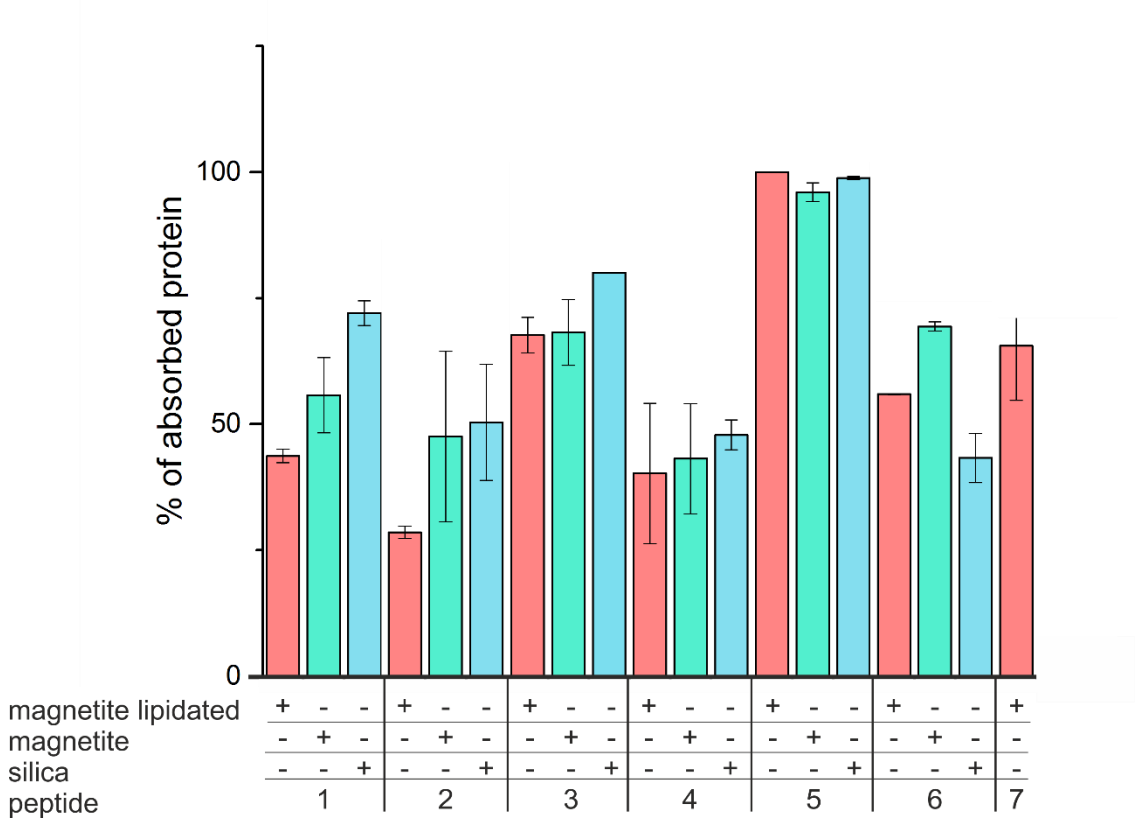

Figure 14: Percentage of absorbed peptide on different particles. Either particles with or without an oleic acid lipid bilayer. Peptides 1-7 were tested on magnetite and silica nanoparticles of equal size. Since peptide 7 was only used for comparing interaction efficiency with lipid mono- or bilayers there is no data of peptide 7 with blank particles. n=6

3.3.2 Affinity based adsorption of Mms6 peptide 4 during alkaline precipitation of magnetite nanoparticles

Prozorov et al. propose a role of Mms6 in the formation of the magnetosomes magnetite core and attribute the first steps of particle formation to the presence of Mms6 [103]. Their experiments have shown that Mms6 influences the particle size and shape if present during alkaline precipitation of magnetite particles. They attribute this effect dominantly to a C-terminal sequence identical to our peptide 4. We proposed that affinity based adsorption of Mms6 based peptides possibly did not happen on fully formed nanoparticles due to that. Precipitating the magnetite nanoparticles in the presence of the Mms6 based peptides might facilitate a strong specific attachment of the peptides to the nanoparticles as it forms.

In order to validate this hypothesis, alkaline co-precipitation of Fe_2O_3 and Fe_3O_4 in presence of Mms6 peptide 4 was performed. Since Prozorov claim that the acidic part of Mms6 is necessary for interaction with iron, and short fragments are not as suitable as larger ones, all other Mms6 based peptides were not used any longer for these experiments. To simulate natural cytoplasmic viscosity, Pluronic F-127 was added to the reaction mixture. Oleic acid was added in order to produce a lipid bilayer similar to those present on the native magnetosome [97b]. The effect of each of these constituents on nanoparticle size was evaluated using DLS (Figure 15).

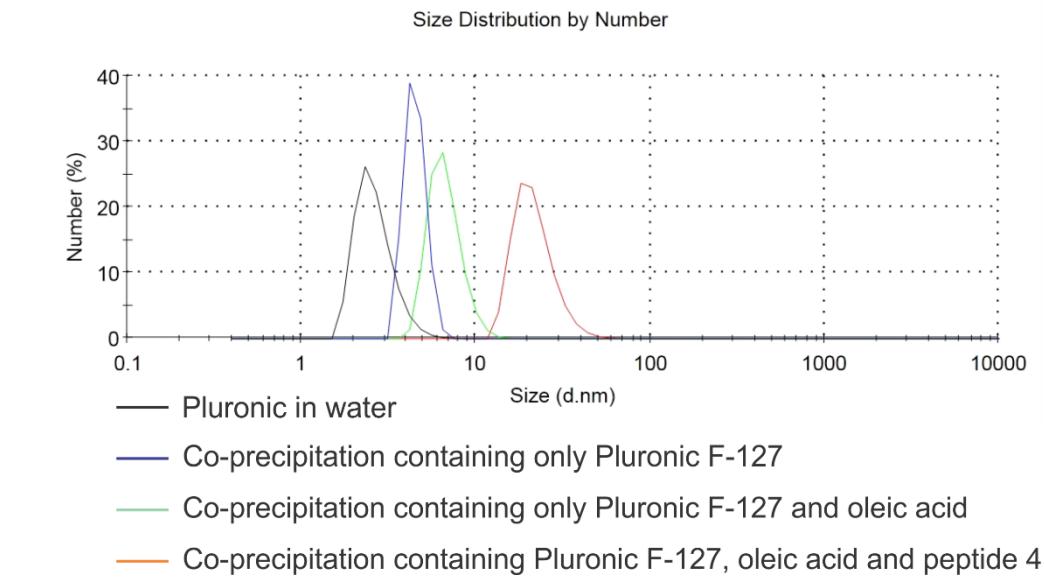

Figure 15: Dynamic light scattering data on the influence of different conditions on particle size during alkaline co-precipitation of a Fe_2O_3/Fe_3O_4 solution. Results weighted by number.

DLS measurements show that Pluronic F-127 itself produces weak scattering interference that are interpreted as ~2 nm size particles by the software. This is a direct result from its high viscosity and resulting scattering of light. Since signal intensity at DLS experiments increases with radius of the particles to the power of 6, these small Pluronic F-127 signals are very weak and are not detrimental for further experiments. Pluronic F-127 alone influences particle formation during co-precipitation resulting in particles in the size range of natural magnetosomes (6-8 nm). Adding oleic acid and Pluronic F-127 increases the size to 7-9 nm which corresponds well with the increase in size that the addition of a lipid bi- or monolayer produces. Adding Pluronic F-127, oleic acid and peptide 4 to the co-precipitation solution results in significantly larger particles of around 12-14 nm. In contrast to Prozorov we do not observe a similar effect of peptide 4 towards smaller particle sizes. Adding only peptide 4 to the co-precipitation solution results in heterogeneous particle populations with polydispersity indexes close to 1. The same result was obtained when using no additives to the co-precipitation, indicating no effect at all of peptide 4 on particle size. Since polydispersity indices of 1 deliver no signals at all no data is shown for these two cases.

Adsorption of peptide 4 on magnetite particles was compared with peptide 6. Verification of particle sizes using ESEM measurements was not successful since Pluronic F-127 covers the samples completely under a smooth surface and cannot be removed in large enough quantities to stop this from happening.

Both peptides were used separately in identical co-precipitation experiments in order to prove specificity of peptide 4 over control peptide 6. After precipitation, unbound peptide was removed with the supernatant and peptide concentration was analyzed versus a peptide stock solution of known peptide concentration. Integration of HPLC signals showed very similar results for both peptides (Figure 16). This indicates a non-sequence dependent, unspecific adsorption of peptides on magnetite or silica nanoparticles.

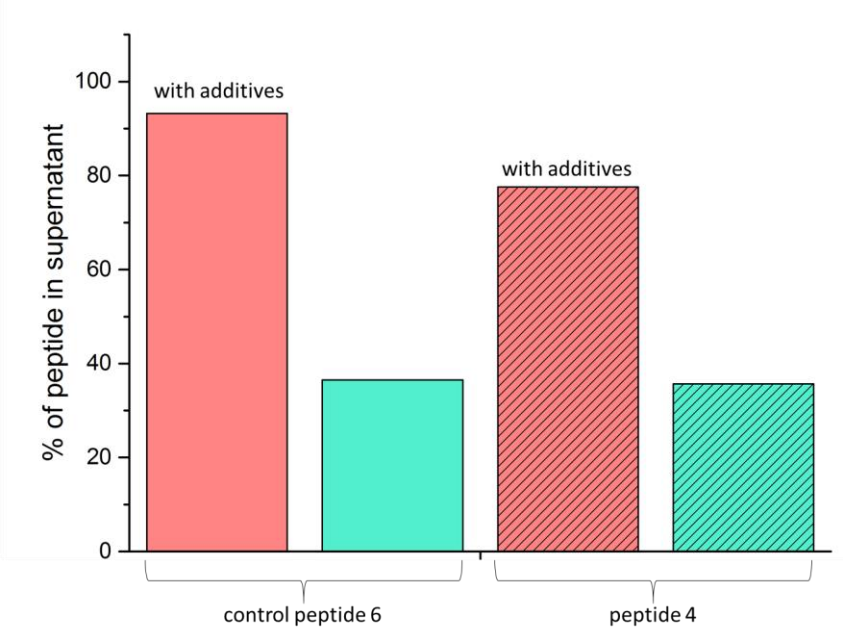

Figure 16: Comparison of peptide affinity for magnetite particles in co-precipitation experiments. Remaining peptide content in the supernatant after co-precipitation experiments for precipitation with or without additives. Additives: oleic acid and Pluronic F-127 added during co-precipitation. n=2

The possibility remained that sequence dependent, specific adsorption on magnetite nanoparticles might be achieved using the Mms6 based peptide 4 sequence with the enzyme attached recombinantly. We therefore aimed to express a recombinant cellulase-peptide 4 variant.

3.3.3 Recombinant production of a cellulase-peptide construct with peptide 4

We aimed to produce a cellulase-peptide 4 fusion construct by recombinant expression in *E.coli*. A small linker with the sequence GGAAGATCTGCAGGCGGAGCAGGAGCA was used as a spacer between cellulase and peptide 4. A pET-24 plasmid that already contained cellulase plus the linker and a modified multiple cloning site for high throughput cloning (Figure 17) was provided by coworkers. We decided to use *Sal*I and *Not*I as restriction sites to obtain incompatible sticky ends, avoid cross reaction and relegation and be able to use the same buffers for all steps. Restriction digests were carried out as simultaneous digest on either restriction sites or one after the other. We used the oligo cloning method for small inserts. Here the DNA is designed as complementary single strands with overlapping ends that correspond to the sticky ends of the used restriction sites. If hybridized, these sequences will result in an insert with sticky ends already present. Using both *Not*I and *Sal*I, either consecutively or in a double digest, did not allow for insertion of the peptide 4 sequence although SDS page confirmed activity of all used enzymes (Figure 17).

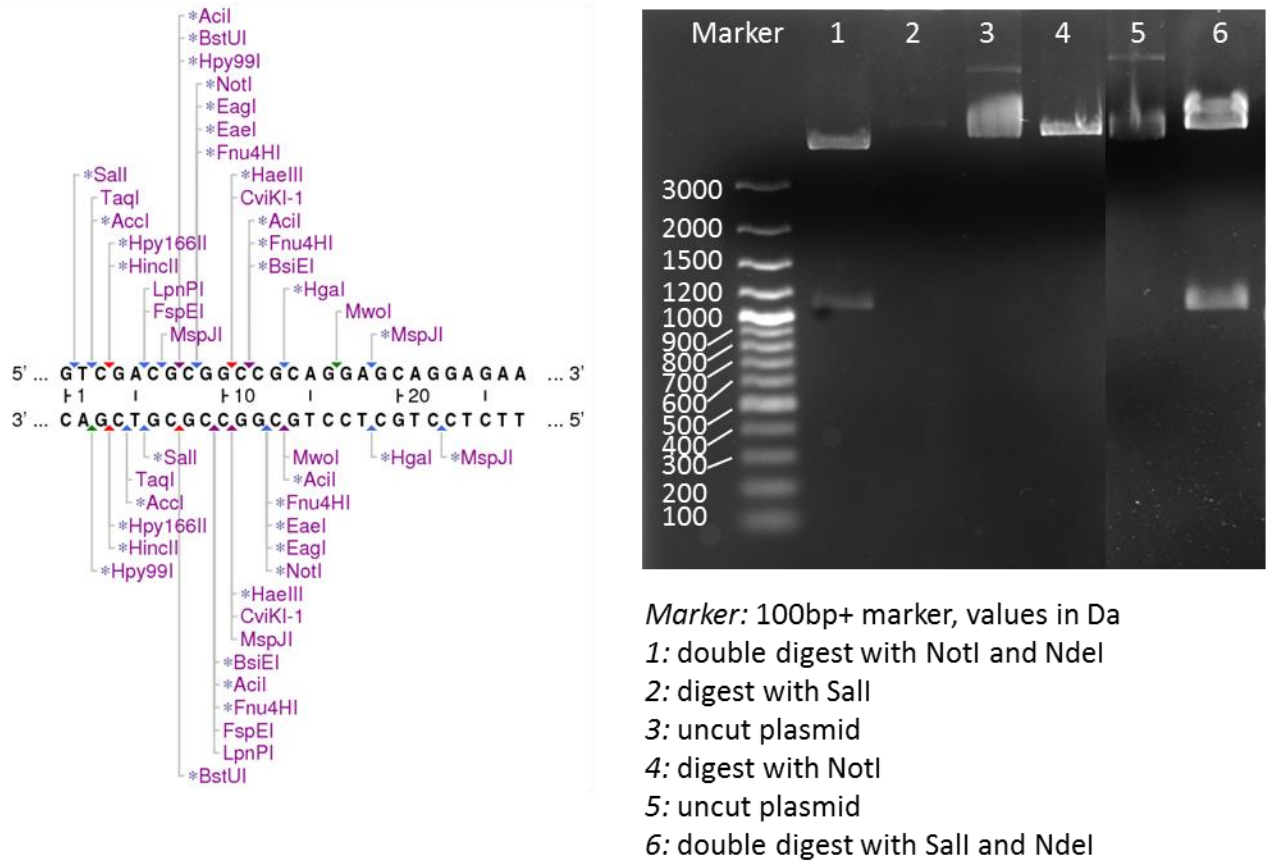

Figure 17: modified multiple cloning site of pET-24 with cellulase and linker already cloned into the plasmid. Plasmid digests using NotI, SalI and NdeI. NdeI was used to cut outside the MCS resulting in easy to identify large fragments of the plasmid in order to verify enzyme function. All three enzymes worked as intended.

Further experiments were then done using peptide 4 already cloned into another plasmid (pEX-A2) obtained from eurofins, Vienna. Due to the small size of the peptide 4 sequence (85 nucleotides) normal workup using standard purification kits was not possible. We devised two different variants of cloning experiments (cloning method I and II) that should address this challenge. Cloning method I (Figure 18) uses a symmetric workup procedure exploiting the fact that very small nucleotide chains are lost during standard purification workups. After a digest with *Not*I and *Sal*I, the pET-24 plasmid containing cellulase with linker is shortened by only 6 nucleotides. After workup this small piece is not recovered and the linearized DNA remains. A digest of the pEX-A2 plasmid containing the peptide 4 sequence is then added to the purified pET-24 plasmid. The pEX-A2 digest has not been purified, otherwise the short peptide 4 insert would have been lost. Due to incompatible sticky ends the pET-24 plasmid cannot realign. It can only incorporate the peptide 4 sequence or incorporate the remaining pEX-A2 plasmid forming a large superplasmid. The pEX-A2 plasmid on the other hand can either reinsert the cut peptide 4 sequence, or built a very large plasmid by fusing also with the pET-24 plasmid. After ligation reaction the bacteria are selected towards the resistance incorporated in the pET-24 plasmid. Therefore only two possible variants should remain. The pET-24 with the right peptide 4 insert, or a large plasmid that consists of pEX-A2 and pET-24. Transforming the final plasmid into E.coli bacteria and consecutive harvest and sequencing of selected colonies DNA did not show any insertion of the desired fragment (Figure 20).

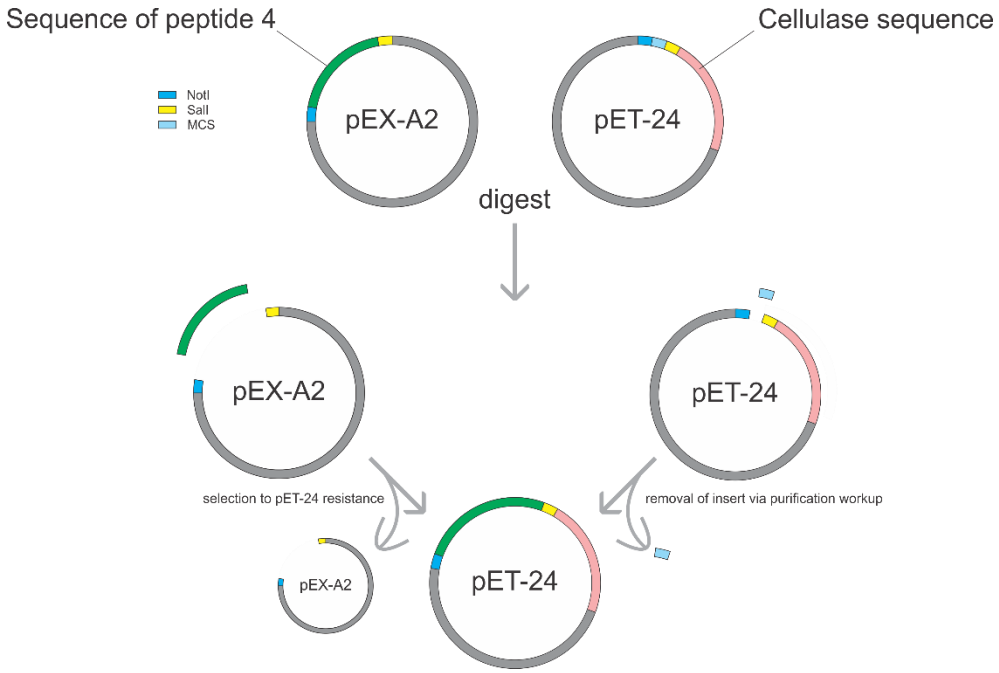

Figure 18: Schematic of cloning method I. pEX-A2 with peptide 4 and pET-24 with cellulase were digested using the SalI and NotI restriction sites. The pET-24 digest is worked up and the small insert is not recovered due to its small size. Annealing should result in either the desired clone or reinsertion of the Peptide 4 insert into the pEX-A2 vector. pET-24 cannot connect its sticky ends without the peptide 4 insert. Selection with kanamycin removes all pEX-A2 plasmids and only viable pET-24 plasmids containing the cellulase and Peptide 4 sequence survive.

Cloning method II addresses the concern that having two restriction sites that are too close together for the restriction enzymes to detect the cutting site might be the reason for cloning failure. Using *Not*I and *BseY*I as restriction enzymes, a large 752 base pair sequence will be cleaved from the pEX-A2 plasmid. A sequence of this size is easily purified via gel extraction. This sequence, containing the peptide 4 gene will then be digested again using *Sal*I, resulting in a DNA strand containing two sequences, peptide 4 and a 667 base pair sequence of no interest. Ligation of this mixture with a digested and purified pET-24 plasmid should again result in the desired clone (Figure 19).

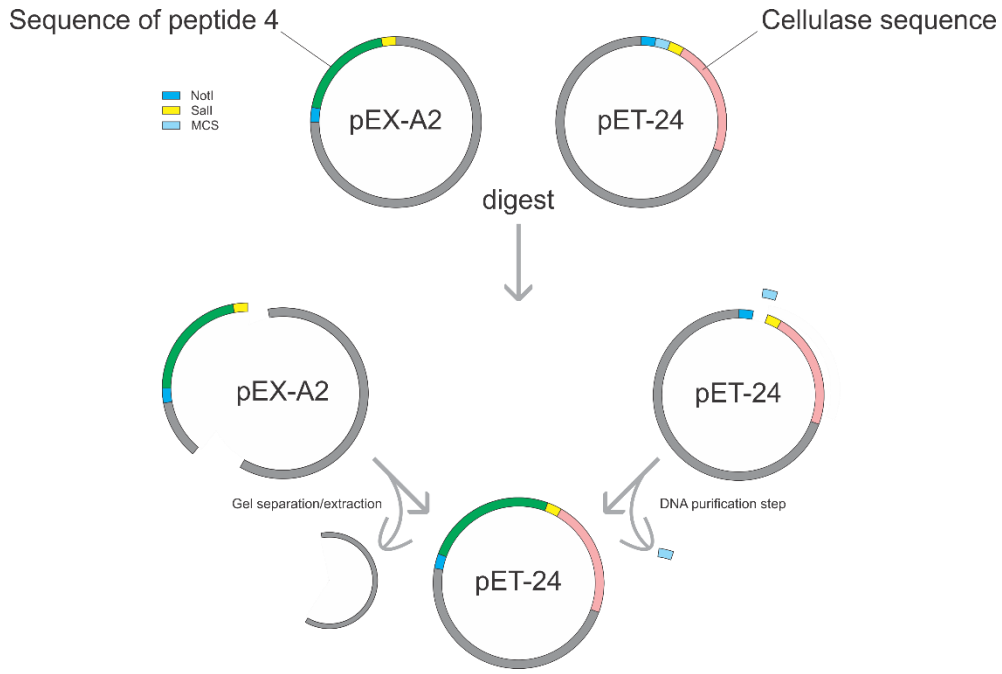

Figure 19 Schematic of cloning method II. pEX-A2 and pET-24 containing the Peptide 4 and cellulase-linker sequence respectively were digested with SalI and NotI in the case of the pET-24 plasmid or NotI and BseYI for the pEX-A2 plasmid. This results in a very small DNA fragment cut from the pET-24 and a large fragment cut from the pEX-A2 plasmid. Using gel extraction it is now possible to purify the Peptide 4 sequence due to the large part of the plasmid still attached to it. Digest with SalI results in the desired Peptide 4 fragment in the solution that can then be used without further purification to be inserted into the pET-24 plasmid

Sequencing of several of the clones from both approaches showed no correct insertion of the Peptide 4 sequence into the pET-24 plasmid. Both approaches show deletion products in the MCS after the experiments as well as random sequence insertions that do not correspond to any part of the Peptide 4 sequence (Figure 20 as well as appendix for detailed data).

Linker MCS Peptide 4 Tev Site and His Tag

KLADIGRSAGGAGAVDAAAGAGENLYFQGHHHHHH ORIGINAL SEQUENCE

KLADIGRSAGGAGAVDVYAYMKSRDIESAQSDEEVELRDALAAAAGAGENLYFQGHHHHHH

KLADIGRSAGGAGENLYFQGHHHHHH

KLADIGRSAGGAGAVDAGFKAGAAAGAGENLYFQGHHHHHH

KLADIGRSAGGAGAGENLYFQGHHHHHH

KLADIGRSAGGAGAVDAGFKAGAAAGAGENLYFQGHHHHHH

Figure 20: Sequencing of the first two clones from cloning method I and II experiments. Original sequence shows the pET-24 plasmid before the experiments. With the lilac insert the expected sequence is shown, having the Peptide 4 sequence inserted into the MCS. From top to bottom are then the first two analysis results from method I and II respectively. All other picked clones (10 each) did show similar results (see appendix).

3.4 Conclusion

It was possible to synthesize different Mms6 based peptides (1-7) in order to determine if these peptides show any specific affinity towards magnetic nanoparticles. We could show that sample preparation is crucial for the work with nanoparticles since they form large agglomerates very fast, making experimental results unreliable. 20 minutes after heavy sonication for 2 minutes, the particles had already returned to large agglomerates with very high polydispersity indices. Taking these findings into account we were able to test the Mms6 peptides and compare their affinity to that of a negative control peptide with no sequence similarities (peptide 6) as well as a peptide equipped with hydrophobic side chains that should show higher affinities towards nanoparticles encapsulated in a lipid bilayer (peptide 7).

No defined trend could be found for the adsorption of Mms6 peptides on magnetite nanoparticles in these experiments. The control peptide 6 showed considerable higher adsorption values than most of the Mms6 peptides. A difference in adsorption behavior between Mms6 peptides on magnetite or silica nanoparticles was not significant. A specific affinity of the Mms6 peptides towards magnetite nanoparticles was not found.

Examining the role of Mms6 in the formation of magnetite nanoparticles as a means to attach the peptide to magnetic nanoparticles during particle formation was done using the Mms6 peptide variant 4 that covers the protein sequence that is reported to be responsible for initiating particle formation and control. Our experiments did not verify the influence peptide 4 has on particle size during particle formation reported by Prozorov et.al [103]. On the contrary we could report a striking influence on particle size during particle formation of the additives used by Prozorov, with the majority of size control attributable to the viscosity enhancer Pluronic F-127. Adsorption or incorporation of peptide 4 during the precipitation process of magnetite nanoparticles is not specific, the negative control peptide 6 again showed higher adsorption/incorporation rates than peptide 4.

Recombinant production of a peptide 4-cellulase construct could not be achieved. Assay or enzyme failure could be successfully ruled out, which leaves structural challenges of the peptide 4 sequence as a possible explanation for the problems. Most likely the small insert folds in a way that makes the sticky ends inaccessible for cloning.

In conclusion we could show that the Mms6 peptide variants show no discernible affinity for magnetite nanoparticles. The presented data does hint towards an unspecific affinity of peptides towards nanoparticles regardless of their size, since all tested peptides showed at least moderate adsorption (~40-50%) on nanoparticles. This was also true when the particle material was changed. This unspecific adsorption behavior was first brought to the attention of the scientific community by Jacob Klein under the name of protein corona[104].

3.5 Literature

[1] D. A. Bazylinski, R. B. Frankel, *Nat Rev Micro* **2004**, *2*, 217-230.

[2] aD. Samuel, *Science* **1996**, *273*, 488; bP. E. McGovern, S. J. Fleming, S. H. Katz, *The origins and ancient history of wine: food and nutrition in history and antropology*, Routledge, **2003**.

[3] S. Sen, V. V. Dasu, B. Mandal, *Appl Biochem Biotech* **2007**, *143*, 212-223.

[4] T. Haider, Q. Husain, *International Journal of Pharmaceutics* **2008**, *359*, 1-6.

[5] R. Y. Cabrera-Padilla, M. C. Lisboa, A. T. Fricks, E. Franceschi, A. S. Lima, D. P. Silva, C. M. F. Soares, *J Ind Microbiol Biotechnol* **2012**, *39*, 289-298.

[6] J. L. Fu, J. Reinhold, N. W. Woodbury, *Plos One* **2011**, *6*.

[7] H. Wen, V. Nallathambi, D. Chakraborty, S. C. Barton, *Microchim Acta* **2011**, *175*, 283-289.

[8] J. T. Chern, Y. P. Chao, *J Biotechnol* **2005**, *117*, 267-275.

[9] R. Bussamara, L. Dall'agnol, A. Schrank, K. F. Fernandes, M. H. Vainstein, *Enzyme Res* **2012**, *2012*, 329178.

[10] B. C. Kim, D. Lopez-Ferrer, S. M. Lee, H. K. Ahn, S. Nair, S. H. Kim, B. S. Kim, K. Petritis, D. G. Camp, J. W. Grate, R. D. Smith, Y. M. Koo, M. B. Gu, J. Kim, *Proteomics* **2009**, *9*, 1893-1900.

[11] J. M. Guisán, G. Penzol, P. Armisen, A. Bastida, R. M. Blanco, R. Fernandez-Lafuente, E. García-Junceda, in *Immobilization of Enzymes and Cells* (Ed.: G. F. Bickerstaff), Humana Press, Totowa, NJ, **1997**, pp. 261-275.

[12] Y. M. Elcin, *Biomaterials* **1995**, *16*, 1157-1161.

[13] A. Flores-Maltos, L. V. Rodriguez-Duran, J. Renovato, J. C. Contreras, R. Rodriguez, C. N. Aguilar, *Enzyme Res* **2011**, *2011*, 768183.

[14] F. Vaillant, A. Millan, P. Millan, M. Dornier, M. Decloux, M. Reynes, *Process Biochem* **2000**, *35*, 989-996.

[15] L. C. Katwa, M. Ramakrishna, M. R. R. Rao, *J Bioscience* **1981**, *3*, 135-142.

[16] H. Tumturk, N. Karaca, G. Demirel, F. Sahin, *Int J Biol Macromol* **2007**, *40*, 281-285.

[17] Q. Y. Shen, R. J. Yang, X. Hua, F. Y. Ye, W. B. Zhang, W. Zhao, *Process Biochem* **2011**, *46*, 1565-1571.

[18] S. Ates, N. S. Dogan, *Turk J Biochem* **2010**, *35*, 58-62.

[19] A. J. H. Al-Adhami, J. Bryjak, B. Greb-Markiewicz, W. Peczynska-Czoch, *Process Biochem* **2002**, *37*, 1387-1394.

[20] D. Mislovicova, J. Masarova, A. Vikartovska, P. Gemeiner, E. Michalkova, *J Biotechnol* **2004**, *110*, 11-19.

[21] J. Bryjak, J. Aniulyte, J. Liesiene, *Carbohydr Res* **2007**, *342*, 1105-1109.

[22] M. Namdeo, S. K. Bajpai, *Journal of Molecular Catalysis B: Enzymatic* **2009**, *59*, 134-139.

[23] K. Labus, A. Turek, J. Liesiene, J. Bryjak, *Biochem Eng J* **2011**, *56*, 232-240.

[24] X. J. Huang, P. C. Chen, F. Huang, Y. Ou, M. R. Chen, Z. K. Xu, *J Mol Catal B-Enzym* **2011**, *70*, 95-100.

[25] M. P. Klein, C. W. Scheeren, A. S. G. Lorenzoni, J. Dupont, J. Frazzon, P. F. Hertz, *Process Biochem* **2011**, *46*, 1375-1379.

[26] M. Matto, Q. Husain, *J Mol Catal B-Enzym* **2009**, *57*, 164-170.

[27] N. A. Dung, N. D. Huyen, N. D. Hang, T. T. Canh, *Radiat Phys Chem* **1995**, *46*, 1037-1042.

[28] A. I. Raafat, E. Araby, S. Lotfy, *Carbohydrate Polymers* **2012**, *87*, 1369-1374.

[29] R. Satar, M. Matto, Q. Husain, *J Sci Ind Res India* **2008**, *67*, 609-615.

[30] L. Gomez, H. L. Ramirez, A. Neira-Carrillo, R. Villalonga, *Bioproc Biosyst Eng* **2006**, *28*, 387-395.

[31] S. Hosseinkhani, R. Szittner, M. Nemat-Gorgani, E. A. Meighen, *Enzyme and Microbial Technology* **2003**, *32*, 186-193.

[32] M. Miroliaei, H. Nayeri, S. Z. Samsam-Shariat, A. M. Atar, *Sci Iran* **2007**, *14*, 303-307.

[33] P. C. Ashly, M. J. Joseph, P. V. Mohanan, *Food Chemistry* **2011**, *127*, 1808-1813.
[34] Q. Xiangli, L. Zhe, L. Zhiwei, Z. Yinglin, Z. Zhengjia, *Biochem Eng J* **2010**, *50*, 71-76.
[35] T. Romaskevic, E. Viskantiene, S. Budriene, A. Ramanaviciene, G. Dienys, *Journal of Molecular Catalysis B: Enzymatic* **2010**, *64*, 172-176.
[36] S. Pahujani, S. S. Kanwar, G. Chauhan, R. Gupta, *Bioresource Technology* **2008**, *99*, 2566-2570.
[37] M. V. Kahraman, G. Bayramoğlu, N. Kayaman-Apohan, A. Güngör, *Reactive and Functional Polymers* **2007**, *67*, 97-103.
[38] M. A. Abdel-Naby, *Process Biochem* **1999**, *34*, 399-405.
[39] M. Koneracká, P. Kopčanský, M. Antalík, M. Timko, C. N. Ramchand, D. Lobo, R. V. Mehta, R. V. Upadhyay, *Journal of Magnetism and Magnetic Materials* **1999**, *201*, 427-430.
[40] G.-W. Xing, X.-W. Li, G.-L. Tian, Y.-H. Ye, *Tetrahedron* **2000**, *56*, 3517-3522.
[41] Y. K. Chang, L. Chu, *Biochem Eng J* **2007**, *35*, 37-47.
[42] aL. Huang, Z.-M. Cheng, *Chem Eng J* **2008**, *144*, 103-109; bM. Kamori, T. Hori, Y. Yamashita, Y. Hirose, Y. Naoshima, *Journal of Molecular Catalysis B: Enzymatic* **2000**, *9*, 269-274.
[43] D. Koszelewski, N. Müller, J. H. Schrittwieser, K. Faber, W. Kroutil, *Journal of Molecular Catalysis B: Enzymatic* **2010**, *63*, 39-44.
[44] C.-H. Liu, Y.-H. Lin, C.-Y. Chen, J.-S. Chang, *Journal of the Taiwan Institute of Chemical Engineers* **2009**, *40*, 359-363.
[45] R. P. Pogorilyi, E. Y. Siletskaya, V. P. Goncharik, L. I. Kozhara, Y. L. Zub, *Russ J Appl Chem+* **2007**, *80*, 330-334.
[46] M. Soleimani, A. Khani, K. Najafzadeh, *Journal of Molecular Catalysis B: Enzymatic* **2012**, *74*, 1-5.
[47] M. Dezott, L. H. Innocentini-Mei, N. Durán, *Journal of Biotechnology* **1995**, *43*, 161-167.
[48] C. C. Rosa, H. J. Cruz, M. Vidal, A. G. Oliva, *Biosensors and Bioelectronics* **2002**, *17*, 45-52.
[49] R. Sahney, B. K. Puri, S. Anand, *Analytica Chimica Acta* **2005**, *542*, 157-161.
[50] F. B.-O. Daoud, S. Kaddour, T. Sadoun, *Colloids and Surfaces B: Biointerfaces* **2010**, *75*, 93-99.
[51] A. Ganesh Kumar, K. Perinbam, P. Kamatchi, N. Nagesh, G. Sekaran, *Bioresource Technology* **2010**, *101*, 1377-1379.
[52] G. Kibarer, G. Akovali, *Biomaterials* **1996**, *17*, 1473-1479.
[53] A. S. Rani, M. L. M. Das, S. Satyanarayana, *Journal of Molecular Catalysis B: Enzymatic* **2000**, *10*, 471-476.
[54] S. Dutta, A. Bhattacharyya, P. De, P. Ray, S. Basu, *Journal of Hazardous Materials* **2009**, *172*, 888-896.
[55] S. Bellini, *Chin J Oceanol Limn* **2009**, *27*, 6-12.
[56] R. Blakemore, *Science* **1975**, *190*, 377-379.
[57] C. B. Flies, H. M. Jonkers, D. de Beer, K. Bosselmann, M. E. Böttcher, D. Schüler, *FEMS Microbiology Ecology* **2005**, *52*, 185-195.
[58] R. B. Frankel, D. A. Bazylinski, in *Design and Processing of Materials by Biomimetics* (Ed.: I. A. M. Sarikaya), AIP Press, **1995**, pp. 199-216.
[59] D. Schuler, *Fems Microbiol Rev* **2008**, *32*, 654-672.
[60] A. Komeili, *Fems Microbiol Rev* **2012**, *36*, 232-255.
[61] C. T. Lefevre, D. Trubitsyn, F. Abreu, S. Kolinko, L. G. P. de Almeida, A. T. R. de Vasconcelos, U. Lins, D. Schuler, N. Ginet, D. Pignol, D. A. Bazylinski, *Environ Microbiol* **2013**, *15*, 2267-2274.
[62] aS. Schubbe, M. Kube, A. Scheffel, C. Wawer, U. Heyen, A. Meyerdierks, M. H. Madkour, F. Mayer, R. Reinhardt, D. Schuler, *Journal of Bacteriology* **2003**, *185*, 5779-5790; bY. Fukuda, Y. Okamura, H. Takeyama, T. Matsunaga, *Febs Lett* **2006**, *580*, 801-812.
[63] R. P. Blakemore, *Annu Rev Microbiol* **1982**, *36*, 217-238.
[64] C. B. Flies, J. Peplies, D. Schüler, *Applied and Environmental Microbiology* **2005**, *71*, 2723-2731.
[65] D. Schuler, E. Baeuerlein, *Arch Microbiol* **1996**, *166*, 301-307.

[66] W. E. Müller, *Molecular biomineralization: aquatic organisms forming extraordinary materials*, Springer Science & Business Media, **2011**.
[67] aR. P. Blakemore, R. B. Frankel, A. J. Kalmijn, *Nature* **1980**, *286*, 384-385; bB. L. Taylor, I. B. Zhulin, M. S. Johnson, *Annual Review of Microbiology* **1999**, *53*, 103-128; cR. B. Frankel, D. A. Bazylinski, M. S. Johnson, B. L. Taylor, *Biophys J* **1997**, *73*, 994-1000.
[68] R. B. Frankel, *Annu Rev Biophys Bio* **1984**, *13*, 85-103.
[69] aD. Schuler, S. Spring, D. A. Bazylinski, *Systematic and Applied Microbiology* **1999**, *22*, 466-471; bS. L. Simmons, D. A. Bazylinski, K. J. Edwards, *Science* **2006**, *311*, 371-374.
[70] D. A. Bazylinski, B. M. Moskowitz, *Rev Mineral* **1997**, *35*, 181-223.
[71] aR. E. Dunin-Borkowski, M. R. McCartney, R. B. Frankel, D. A. Bazylinski, M. Posfai, P. R. Buseck, *Science* **1998**, *282*, 1868-1870; bI. Penninga, H. Dewaard, B. M. Moskowitz, D. A. Bazylinski, R. B. Frankel, *Journal of Magnetism and Magnetic Materials* **1995**, *149*, 279-286.
[72] aK. Grünberg, E.-C. Müller, A. Otto, R. Reszka, D. Linder, M. Kube, R. Reinhardt, D. Schüler, *Applied and Environmental Microbiology* **2004**, *70*, 1040-1050; bY. A. Gorby, T. J. Beveridge, R. P. Blakemore, *Journal of Bacteriology* **1988**, *170*, 834-841.
[73] B. M. Moskowitz, *Reviews of Geophysics* **1995**, *33*, 123-128.
[74] F. W. Brown, *Micromagnetics*, Robert E. Krieger Publishing Company, **1978**.
[75] A. Aharoni, *J Appl Phys* **2001**, *90*, 4645-4650.
[76] M. Richter, M. Kube, D. A. Bazylinski, T. Lombardot, F. O. Glöckner, R. Reinhardt, D. Schüler, *Journal of Bacteriology* **2007**, *189*, 4899-4910.
[77] aC. Nakamura, J. G. Burgess, K. Sode, T. Matsunaga, *Journal of Biological Chemistry* **1995**, *270*, 28392-28396; bY. Okamura, H. Takeyama, T. Matsunaga, *Journal of Biological Chemistry* **2001**, *276*, 48183-48188; cT. Matsunaga, N. Tsujimura, Y. Okamura, H. Takeyama, *Biochem Bioph Res Co* **2000**, *268*, 932-937.
[78] aN. Abreu, S. Mannoubi, E. Ozyamak, D. Pignol, N. Ginet, A. Komeili, *Journal of Bacteriology* **2014**, *196*, 3111-3121; bA. Scheffel, M. Gruska, D. Faivre, A. Linaroudis, J. M. Plitzko, D. Schüler, *Nature* **2006**, *440*, 110-114.
[79] A. Arakaki, J. Webb, T. Matsunaga, *Journal of Biological Chemistry* **2003**, *278*, 8745-8750.
[80] aY. Amemiya, A. Arakaki, S. S. Staniland, T. Tanaka, T. Matsunaga, *Biomaterials* **2007**, *28*, 5381-5389; bM. Tanaka, E. Mazuyama, A. Arakaki, T. Matsunaga, *Journal of Biological Chemistry* **2011**, *286*, 6386-6392.
[81] C. Jogler, M. Kube, S. Schubbe, S. Ullrich, H. Teeling, D. A. Bazylinski, R. Reinhardt, D. Schuler, *Environ Microbiol* **2009**, *11*, 1267-1277.
[82] A. Arakaki, F. Masuda, Y. Amemiya, T. Tanaka, T. Matsunaga, *Journal of Colloid and Interface Science* **2010**, *343*, 65-70.
[83] aS. Feng, L. Wang, P. Palo, X. Liu, S. Mallapragada, M. Nilsen-Hamilton, *International Journal of Molecular Sciences* **2013**, *14*, 14594; bL. Wang, T. Prozorov, P. E. Palo, X. Liu, D. Vaknin, R. Prozorov, S. Mallapragada, M. Nilsen-Hamilton, *Biomacromolecules* **2012**, *13*, 98-105; cS. Kashyap, T. J. Woehl, X. Liu, S. K. Mallapragada, T. Prozorov, *Acs Nano* **2014**, *8*, 9097-9106.
[84] H. Zhang, X. Liu, S. Feng, W. Wang, K. Schmidt-Rohr, M. Akinc, M. Nilsen-Hamilton, D. Vaknin, S. Mallapragada, *Langmuir* **2015**, *31*, 2818-2825.
[85] aJ. M. Galloway, A. Arakaki, F. Masuda, T. Tanaka, T. Matsunaga, S. S. Staniland, *Journal of Materials Chemistry* **2011**, *21*, 15244-15254; bJ. M. Galloway, J. P. Bramble, A. E. Rawlings, G. Burnell, S. D. Evans, S. S. Staniland, *Small* **2012**, *8*, 204-208; cT. Prozorov, P. Palo, L. Wang, M. Nilsen-Hamilton, D. Jones, D. Orr, S. K. Mallapragada, B. Narasimhan, P. C. Canfield, R. Prozorov, *Acs Nano* **2007**, *1*, 228-233.
[86] Y. Malhi, *Philosophical Transactions of the Royal Society A: Mathematical, Physical and Engineering Sciences* **2002**, *360*, 2925-2945.

[87] aE. A. Bayer, R. Lamed, *Biodegradation* **1992**, *3*, 171-188; bP. Falkowski, R. J. Scholes, E. Boyle, J. Canadell, D. Canfield, J. Elser, N. Gruber, K. Hibbard, P. Hogberg, S. Linder, F. T. Mackenzie, B. Moore Iii, T. Pedersen, Y. Rosental, S. Seitzinger, V. Smetacek, W. Steffen, *Science* **2000**, *290*, 291-296.
[88] M. Desvaux, *Fems Microbiol Rev* **2005**, *29*, 741-764.
[89] aD. Jabbour, B. Klippel, G. Antranikian, *Applied Microbiology and Biotechnology* **2012**, *93*, 1947-1956; bY.-H. P. Zhang, L. R. Lynd, *Biotechnology and Bioengineering* **2004**, *88*, 797-824.
[90] Y. Li, D. C. Irwin, D. B. Wilson, *Applied and Environmental Microbiology* **2007**, *73*, 3165-3172.
[91] A. M. Larsson, T. Bergfors, E. Dultz, D. C. Irwin, A. Roos, H. Driguez, D. B. Wilson, T. A. Jones, *Biochemistry* **2005**, *44*, 12915-12922.
[92] Alisdair B. BORASTON, David N. BOLAM, Harry J. GILBERT, Gideon J. DAVIES, *Biochemical Journal* **2004**, *382*, 769-781.
[93] E. A. Bayer, J.-P. Belaich, Y. Shoham, R. Lamed, *Annual Review of Microbiology* **2004**, *58*, 521-554.
[94] aE. A. Bayer, L. J. W. Shimon, Y. Shoham, R. Lamed, *Journal of Structural Biology* **1998**, *124*, 221-234; bR. H. Doi, A. Kosugi, *Nat Rev Micro* **2004**, *2*, 541-551; cR. H. Doi, A. Kosugi, K. Murashima, Y. Tamaru, S. O. Han, *Journal of Bacteriology* **2003**, *185*, 5907-5914.
[95] S. Zhang, D. E. Wolfgang, D. B. Wilson, *Biotechnology and Bioengineering* **1999**, *66*, 35-41.
[96] G. B. Fields, R. L. Noble, *International Journal of Peptide and Protein Research* **1990**, *35*, 161-214.
[97] aL. Zhang, R. He, H. C. Gu, *Appl Surf Sci* **2006**, *253*, 2611-2617; bQ. Lan, C. Liu, F. Yang, S. Liu, J. Xu, D. Sun, *Journal of Colloid and Interface Science* **2007**, *310*, 260-269.
[98] H.-C. Roth, S. P. Schwaminger, F. Peng, S. Berensmeier, *ChemistryOpen* **2016**, n/a-n/a.
[99] H.-C. Roth, S. P. Schwaminger, M. Schindler, F. E. Wagner, S. Berensmeier, *Journal of Magnetism and Magnetic Materials* **2015**, *377*, 81-89.
[100] K. Rose, J. Vizzavona, *Journal of the American Chemical Society* **1999**, *121*, 7034-7038.
[101] O. Hakami, Y. Zhang, C. J. Banks, *Environmental Science and Pollution Research* **2014**, *22*, 3257-3264.
[102] A. E. Rawlings, J. P. Bramble, A. M. Hounslow, M. P. Williamson, A. E. Monnington, D. J. Cooke, S. S. Staniland, *Chemistry – A European Journal* **2016**, *22*, 7885-7894.
[103] T. Prozorov, S. K. Mallapragada, B. Narasimhan, L. J. Wang, P. Palo, M. Nilsen-Hamilton, T. J. Williams, D. A. Bazylinski, R. Prozorov, P. C. Canfield, *Adv Funct Mater* **2007**, *17*, 951-957.
[104] J. Klein, *Proceedings of the National Academy of Sciences* **2007**, *104*, 2029-2030.

3.6 Appendix

3.6.1 Analytical data for peptide 1

Peptide 1 was synthesized using standard SPPS procedures with a PTI peptide synthesizer. Peptide 1 was purified by RP-HPLC using a preparative C4, 20 mL/min flow rate, 5 % to 65 % buffer B (ACN + 0.08 % TFA) in buffer A (ddH20 + 0.1 % TFA) in 40 min, yielding peptide 1 (1.7 % yield based on crude).

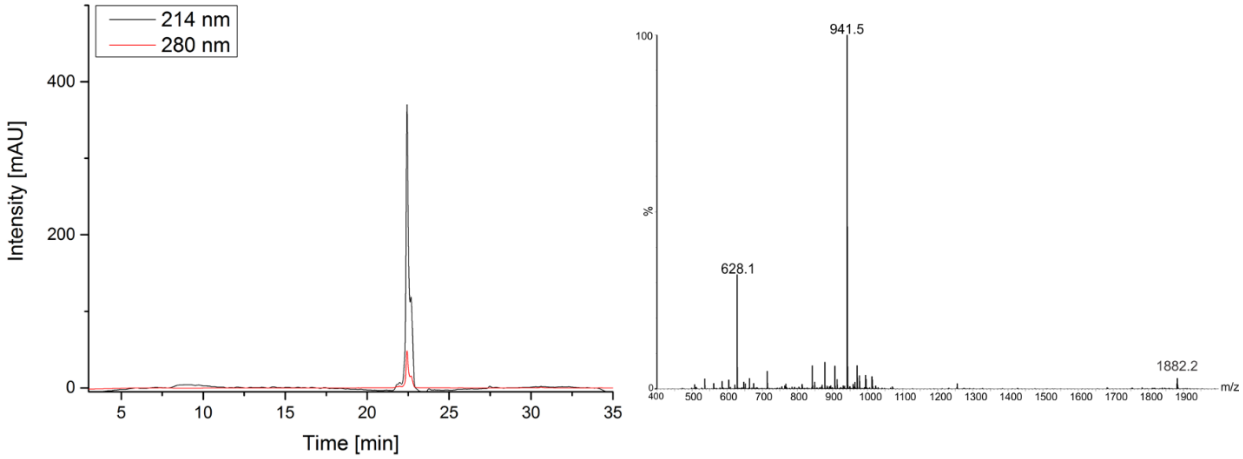

Figure 21: left: Analytical RP-HPLC spectrum of peptide 1; right) ESI-MS spectrum of peptide 1 with a calculated mass of $[M+H]^{+}$ = 1882.6, $[M+2H]^{2+}$ = 941.8 and $[M+3H]^{3+}$ = 628.2

3.6.2 Analytical data for peptide 2

Peptide 2 was synthesized using standard SPPS procedures with a PTI peptide synthesizer. Peptide 2 was purified by RP-HPLC using a preparative C4, 20 mL/min flow rate, 5 % to 65 % buffer B (ACN + 0.08 % TFA) in buffer A (ddH20 + 0.1 % TFA) in 40 min, no yield was determined

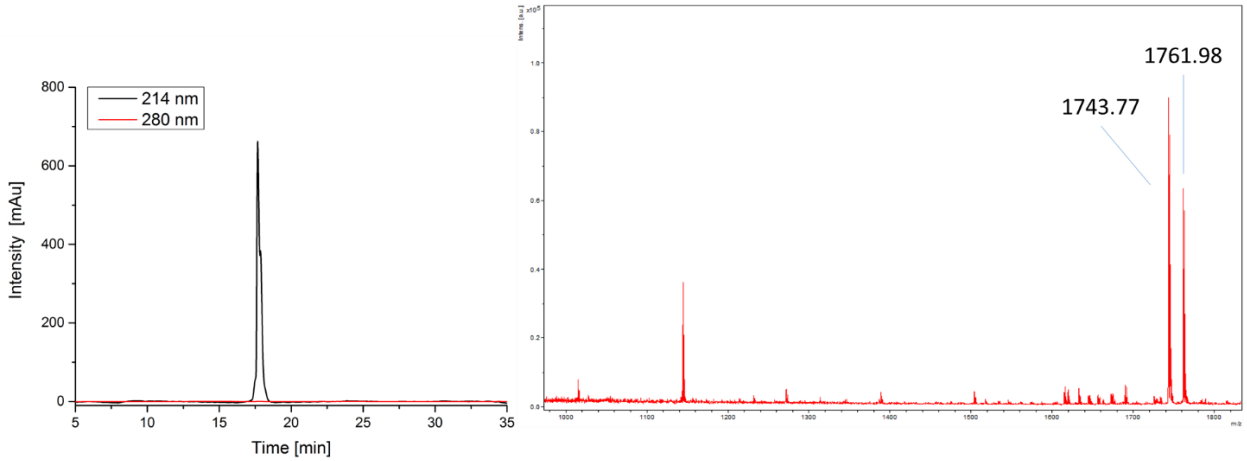

Figure 22: left: Analytical RP-HPLC spectrum of peptide 2; right) MALDI-TOF-MS spectrum of peptide 2 with a calculated mass of $[M+H]^+$ = 1761.06. 1743.77 represents a deletion of water.

3.6.3 Analytical data for peptide 3

Peptide 3 was synthesized using standard SPPS procedures with a PTI peptide synthesizer. Peptide 3 was purified by RP-HPLC using a preparative C4, 20 mL/min flow rate, 5 % to 65 % buffer B (ACN + 0.08 % TFA) in buffer A (ddH20 + 0.1 % TFA) in 40 min, yielding peptide 3 (1.3 % yield based on crude).

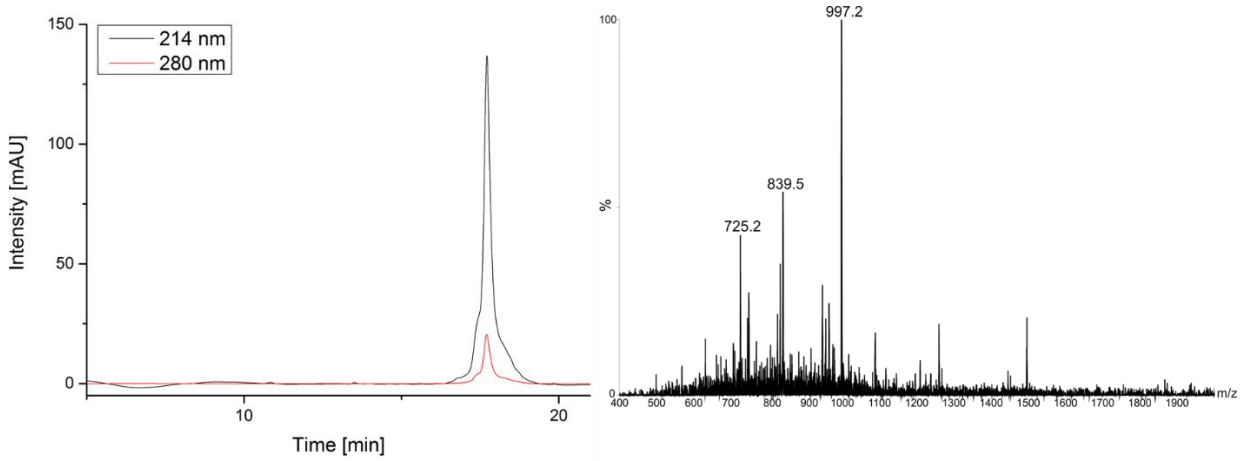

Figure 23: left: Analytical RP-HPLC spectrum of peptide 3; right) ESI-MS spectrum of peptide 3 with a calculated mass of $[M+H]^{+}$ = 2989.56, $[M+2H]^{2+}$ = 1494.78 and $[M+3H]^{3+}$ = 996.52

3.6.4 Analytical data for peptide 4

Peptide 4 was synthesized using standard SPPS procedures with a PTI peptide synthesizer. Peptide 4 was purified by RP-HPLC using a preparative C4, 20 mL/min flow rate, 5 % to 65 % buffer B (ACN + 0.08 % TFA) in buffer A (ddH20 + 0.1 % TFA) in 40 min, yielding peptide 4 (23 % yield based on crude).

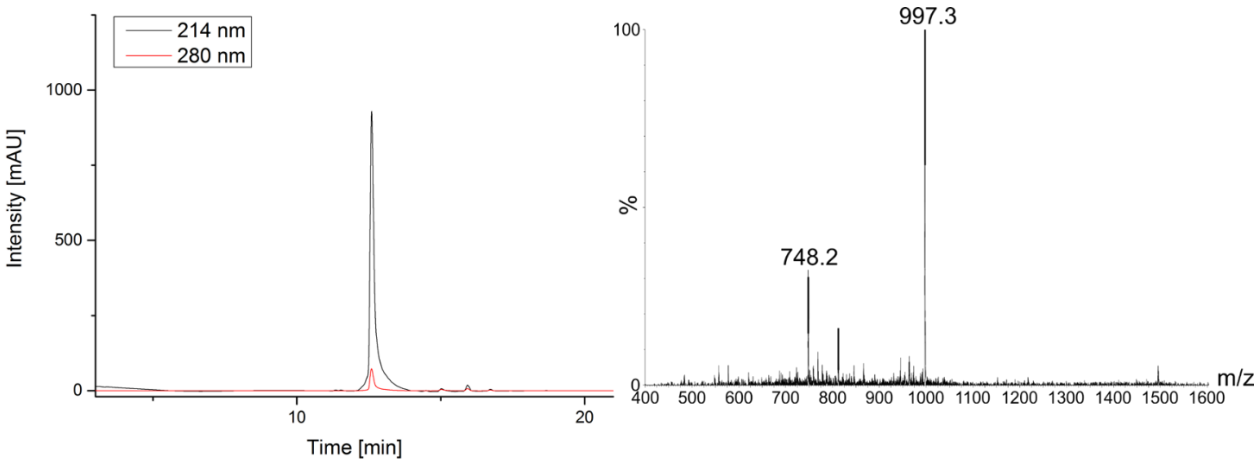

Figure 24: left: Analytical RP-HPLC spectrum of peptide 4; right) ESI-MS spectrum of peptide 4 with a calculated mass of $[M+H]^{+}$ = 2989.27, $[M+2H]^{2+}$ = 1494.63 and $[M+3H]^{3+}$ = 996.42, $[M+4H]^{4+}$ = 747.31

3.6.5 Analytical data for peptide 5

Peptide 5 was synthesized using standard SPPS procedures with a PTI peptide synthesizer. Peptide 5 was purified by RP-HPLC using a preparative C4, 20 mL/min flow rate, 5 % to 65 % buffer B (ACN + 0.08 % TFA) in buffer A (ddH20 + 0.1 % TFA) in 40 min, yielding peptide 5 (1.5 % yield based on crude).

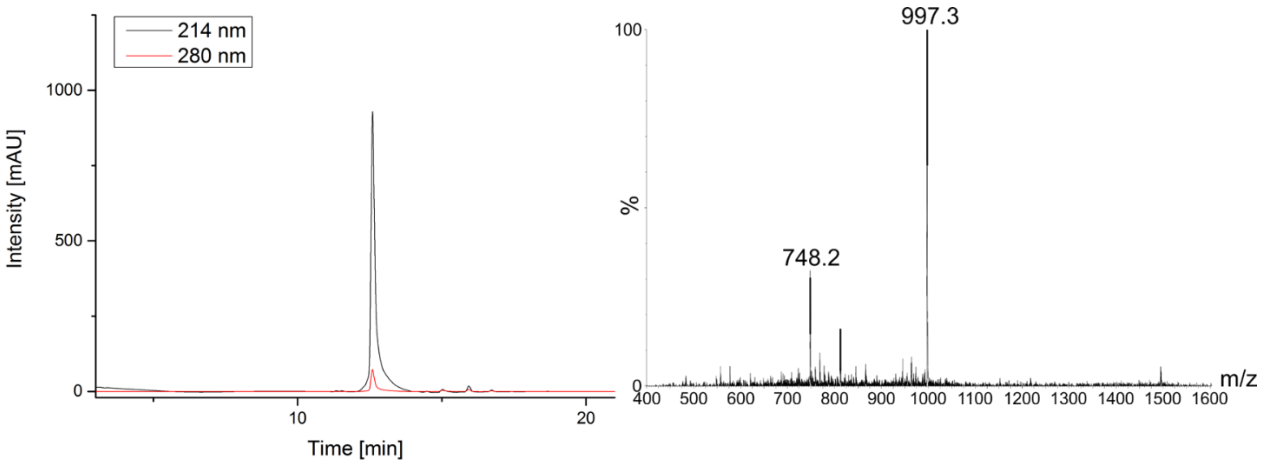

Figure 25: left: Analytical RP-HPLC spectrum of peptide 5; right) ESI-MS spectrum of peptide 5 with a calculated mass of $[M+H]^{+}$ = 3022.52, $[M+2H]^{2+}$ = 1511.26 and $[M+3H]^{3+}$ = 1007.50, $[M+4H]^{4+}$ = 755.63

3.6.6 Analytical data for peptide 6

Peptide 6 was synthesized using standard SPPS procedures with a PTI peptide synthesizer. Peptide 6 was purified by RP-HPLC using a preparative C4, 20 mL/min flow rate, 5 % to 65 % buffer B (ACN + 0.08 % TFA) in buffer A (ddH20 + 0.1 % TFA) in 40 min. No yield was determined

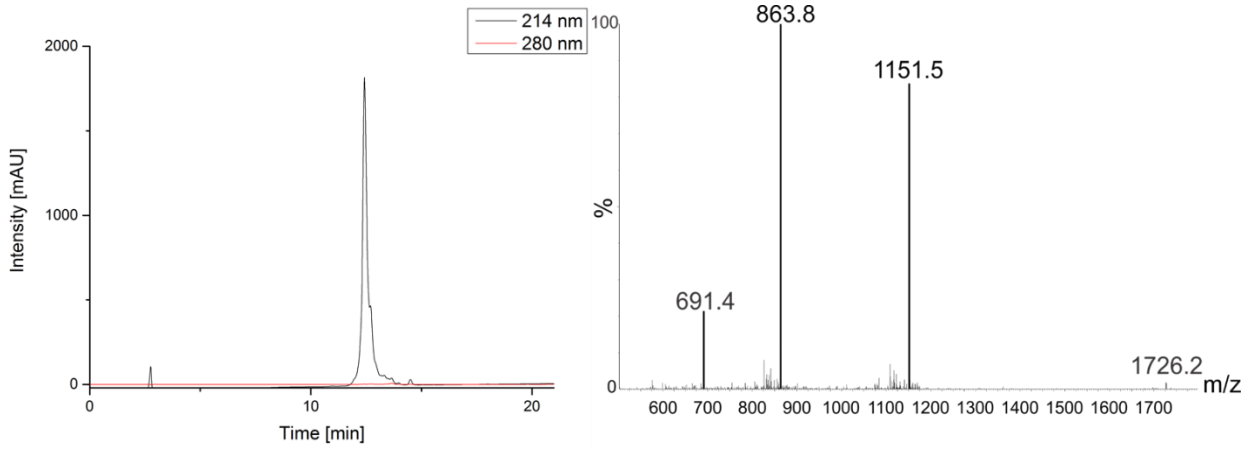

Figure 26: left: Analytical RP-HPLC spectrum of peptide 6; right) ESI-MS spectrum of peptide 6 with a calculated mass of $[M+H]^{+}$ = 3450.80, $[M+2H]^{2+}$ = 1725.4 and $[M+3H]^{3+}$ = 1150.26, $[M+4H]^{4+}$ = 862.7, $[M+5H]^{5+}$ = 690.14

3.6.7 Analytical data for peptide 7

Peptide 7 was synthesized using standard SPPS procedures manually. Peptide 7 was purified by RP-HPLC using a preparative C4, 20 mL/min flow rate, 5 % to 65 % buffer B (ACN + 0.08 % TFA) in buffer A (ddH20 + 0.1 % TFA) in 40 min, yielding peptide 7 (2.2 % yield based on crude). The resulting peptide still has a tBu protecting group attached to its cysteine.

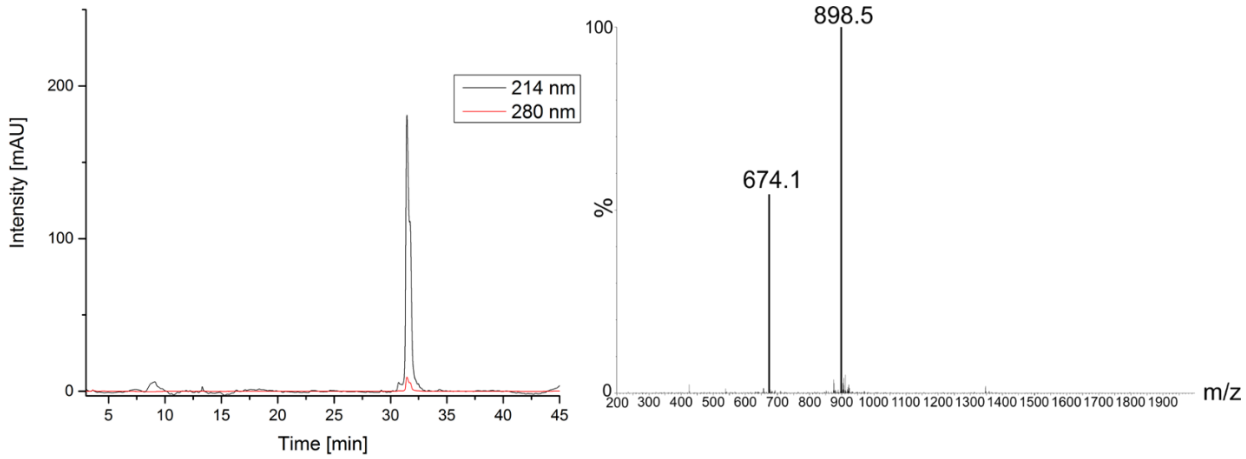

Figure 27: left: Analytical RP-HPLC spectrum of peptide 7; right) ESI-MS spectrum of peptide 7 with a calculated mass of $[M+H]^{+}$ = 2693.42 $[M+2H]^{2+}$ = 1346.71 and $[M+3H]^{3+}$ = 897.81, $[M+4H]^{4+}$ = 673.35

3.6.8 Results of cloning experiments

DNA sequencing of picked clones from cloning method I and II. Insertion would have happened at positions 6201-6285.

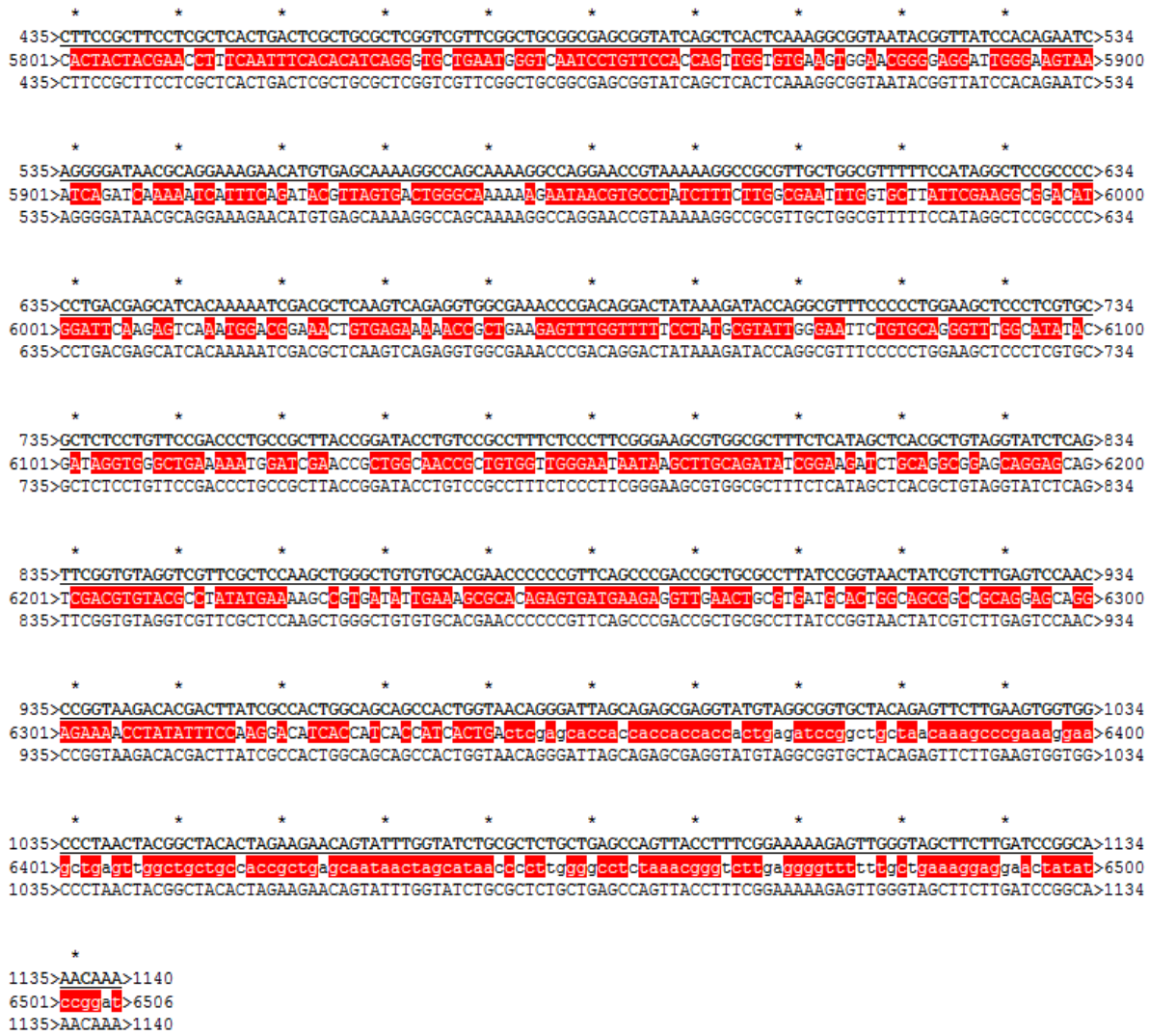

Figure 28: Sequencing data. Red = mismatch. Middle line is the expected sequence, upper and lower line is the sequence data. Results from cloning method I

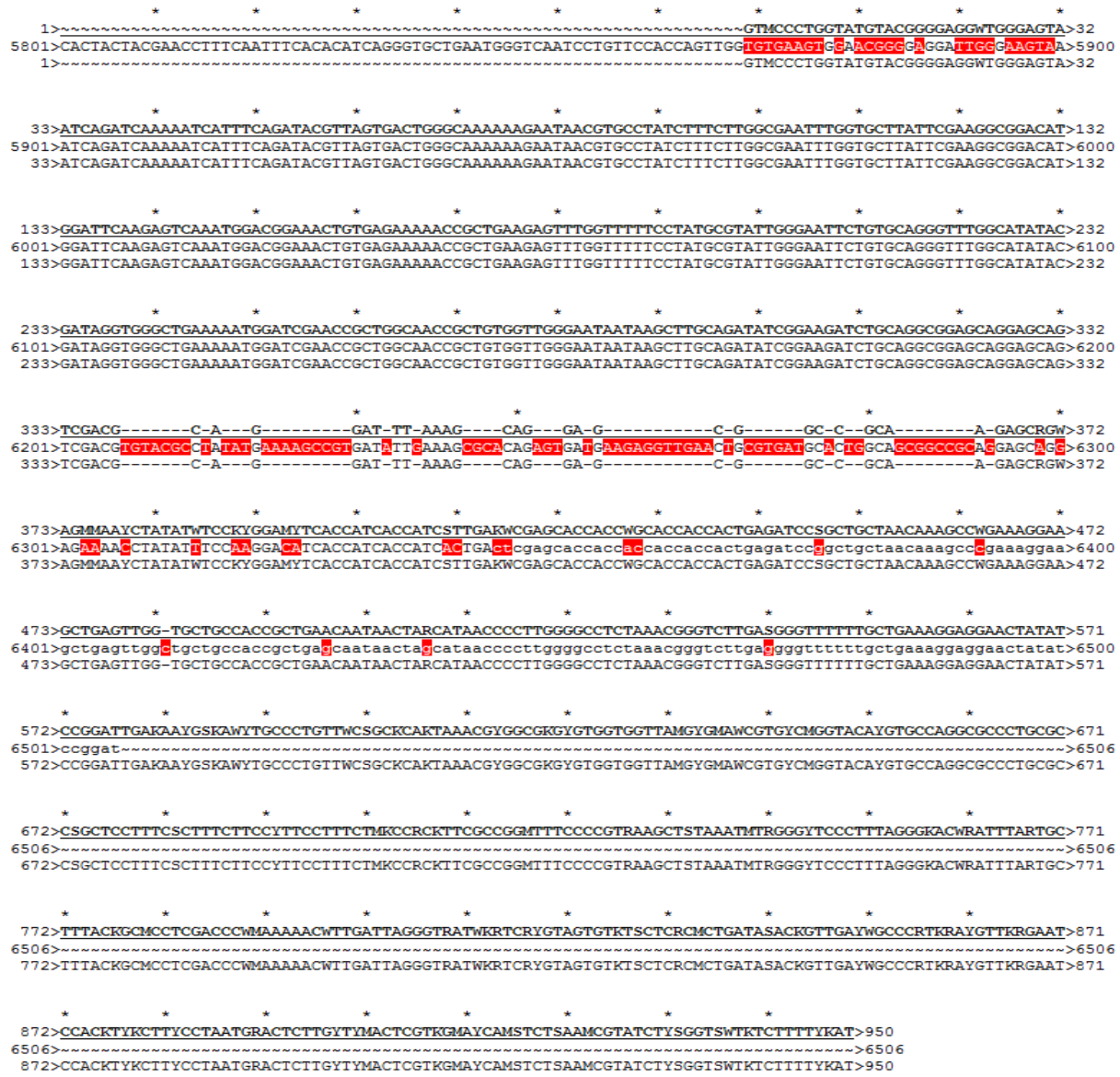

Figure 29: Sequencing data. Red = mismatch. Middle line represents the expected clone, upper and lower the sequencing results. Results from cloning method II

3.6.9 Plasmid charts

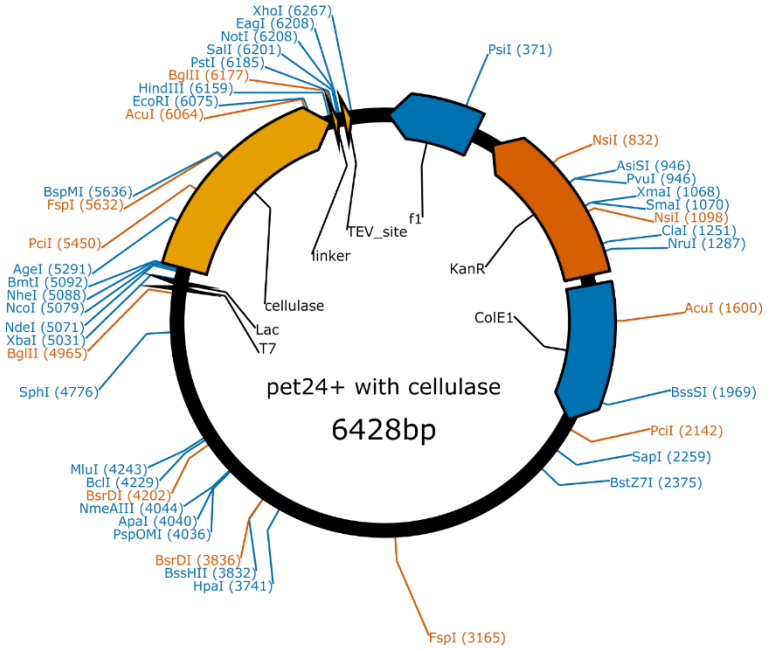

Figure 30: plasmid map of pET24+

Modified MCS for pET 24+

GTCGACGCGGCCGCAGGAGCAGGAGAA

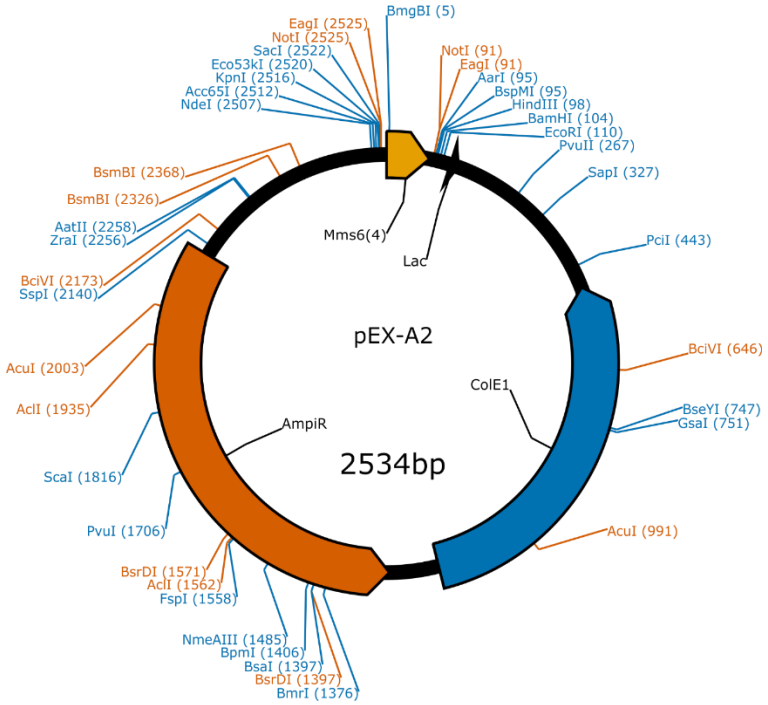

Figure 31: Plasmid chart of pEX-A2 with the Mms6 peptide variant 4 gene sequence added

MCS of pEX-A2 (Mms6 peptide variant 4 in red)

GGAGCAGACAAGCCCGTCAGGGCGCGTCAGCGGGTGTTGGCGGGTGTCGGGGCTGGCTTAACTATGC
GGCATCAGAGCAGATTGTACTGAGAGTGCACcaattgGGTACCgagctcGCGGCCGCAAGCCGACGACGT
GTACGCCTATATGAAAAGCCGTGATATTGAAAGCGCACAGAGTGATGAAGAGGTTGAACTGCGTGAT
GCACTGGCAGCCGTGTACGCCTATATGAAAAGCCGTGATATTGAAAGCGCACAGAGTGATGAAGAGG
TTGAACTGCGTGATGCACTGGCAGCACCTGCTTTTGCTCGCTTggatccGAATTCCTGTGTGAAATTGTTA
TCCGCTCACAATTCCACACAACATACGAGCCGGAAGCATAAAGTGTAAAGCCTG

4 Peptide Corona

4.1 Introduction

4.1.1 Nanoparticles in biological environments

Nanoparticles can be classified as organic or inorganic based structures of natural or artificial origin between the sizes of 1-100 nm. They mostly occur as a waste product by human activity (exhaust gases from cars or power plants) or as specifically produced materials for medical or industrial purposes. Nanoparticle based technology is rapidly increasing and introducing itself in such diverse fields as medicine [1], biotechnology [2], food science [3] or cosmetics [4]. Increased exposure to nanoparticles in our everyday lives makes understanding the interaction between nanoparticles and biological systems more and more important.

Nanoparticles in the sense of this work, are artificial structures of spherical [5], rod-like [6], disk-like [7], triangular [8], cubic [8], cage-like[8], shell-like [9] or even star [10] shape that are usually made from lipids (liposomes [11] or nanoemulsions [12]), carbon (fullerenes [13] and nanotubes [14]), silicon, silica, metals (gold [8], silver [8], iron [15], platinum [16], quantum dots [17], titanoxide [18]) or polymers [19] (e.g. polyethylenimine [20] and dendrimers [21]). They offer unique properties in biological systems that can be exploited to introduce an equally unique approach to medicine, nanomedicine. Depending on particle size and shape, they can enter most compartments of the human body easily. After injection or inhalation nanoparticles could be detected in the colon, lung, liver, heart, thymus, brain and spleen [22]. Interaction of nanoparticles with these organs is not always beneficial. Carbon nanotubes for example have been reported to produce mesothelioma-like lesions similar to those induced by asbestos in mice [23], and silica nanoparticles have a dose dependent damaging effect on the liver as well as significant impact on the MAP/ERK and Nrf2/ARE signaling pathways [24]. After intravenous injection, silica and titanium dioxide nanoparticles were able to cross the trans-placental membrane having relocated into the embryos brain and liver, leading to decreased fetus size and negative impact on brain and liver formation, as well as hampering placental development, increasing the risk of miscarriage [25].

While exact modes of nanoparticle transport into the aforementioned compartments are not perfectly understood yet, some kind of active endocytosis is most likely involved [26]. For cancer cells the entry via the enhanced permeability and retention (EPR) effect is possible as well. This effect, initially described by Maeda is easily exploited by nanoparticles, especially on the larger end of the nanoparticle size scale [27]. The fenestrated endothelium of cancer tissue allows nanoparticles to enter effectively whereas the inefficient lymphatic drainage is not able to remove the large particles from the tumor. Accumulation of nanoparticles in cancer cells is therefore very common.

The fate of nanoparticles in the body is however not only controlled by their shape or molecules covalently attached to them but by their interaction with biomolecules in the surrounding environment. Proteins in particular, but lipids as well, interact directly with nanoparticles upon contact, adsorbing on the nanoparticle surface, changing the surface characteristics of the particle and therefore its fate in the organism [28].

4.1.2 Protein Corona

The adsorption of proteins on surfaces is a well-established phenomenon. Protein adsorption on surfaces of all kinds has been investigated for a long time by the biomaterials community in order to establish adsorption resistant, inert surfaces e.g. for medical implants [29]. It is therefore not surprising that the same effect occurs with nanoparticles or nanostructures that come into contact with biological fluids. Klein as well as Cederwall [30] first brought this knowledge to the attention of the nanomedicine community in 2007. In their work they described the impact of protein adsorption on medical nanoparticles in detail and established the term protein corona to describe the way that proteins adsorb onto nanostructures.

There are two effects leading to high interaction between proteins and nanostructures such as nanoparticles: nanoparticles have a much larger surface energy compared to a flat surface of the same material and large proteins have a tendency to pack around small spaces [31]. Upon being exposed to a biological environment a nanoparticle non-specifically adsorbs surrounding proteins, forming a complete layer of proteins. The protein layer lowers the curvature and surface energy of the particle resulting in a very stable adsorption (Figure 32) [30a, 32]. Any further external interaction now occurs between surface bound proteins and the environment e.g. via weak protein-protein interactions. The new protein layer then defines the biological identity of the particle as well as its bio-distribution in general [33].

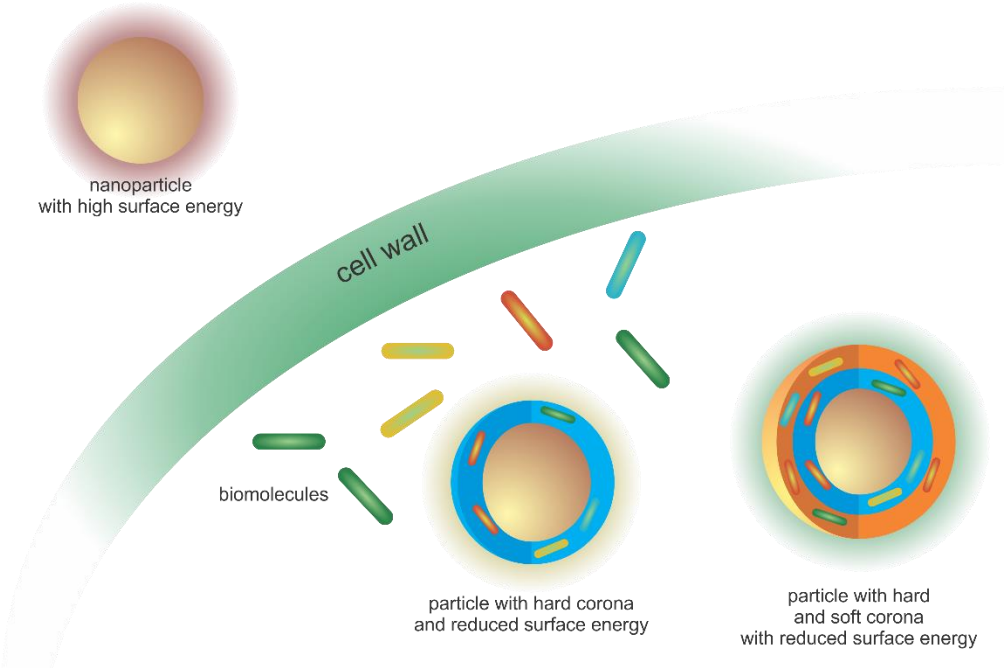

Figure 32: Basic schematic of protein corona formation. Upon moving from a biomolecule free environment (such as a drug formulation in a syringe) to an environment that includes biomolecules (cell the drug is administered to), nanoparticles attract the molecules semi indiscriminately, forming a first layer of molecules on their surface, the hard corona. All further biomolecules adsorb on this initial layer forming a second layer called soft corona.

In a typical biological environment many biomolecules compete for the limited nanoparticle surface. This work focuses on proteins only but lipids have been identified as being adsorbed to the surface as well [34]. Generally, adsorption of proteins on solid surfaces has been described in detail for flat surfaces by the Vroman effect [35], but no such detailed understanding of the adsorption kinetics to nanoparticles exists yet. Fluorescence correlation spectroscopy experiments have shown that the initial layer of proteins adsorbs on the particles within a few hundred microseconds, completely covering the particle. The adsorption is surprisingly stable. New proteins with possible higher affinities for the particle surface do not adsorb or remove adsorbed protein in biological relevant time scales. Blank nanoparticles, despite their high adsorption potential, are not able to remove the hard corona from covered particles [36]. Milani could show that the two time point model of soft and hard corona is misleading. A multilayer model of one hard irreversible corona surrounded by several layers of soft corona is more fitting to the data (Figure 33). The soft corona layers are subject to rapid change and external forces such as new blank nanoparticles [36]. The energetic benefit of the hard corona formation is large enough to allow nanoparticles to rip proteins from intact cell walls to form their corona [37]. This often leads to severe local inflammatory responses in living organisms [38].

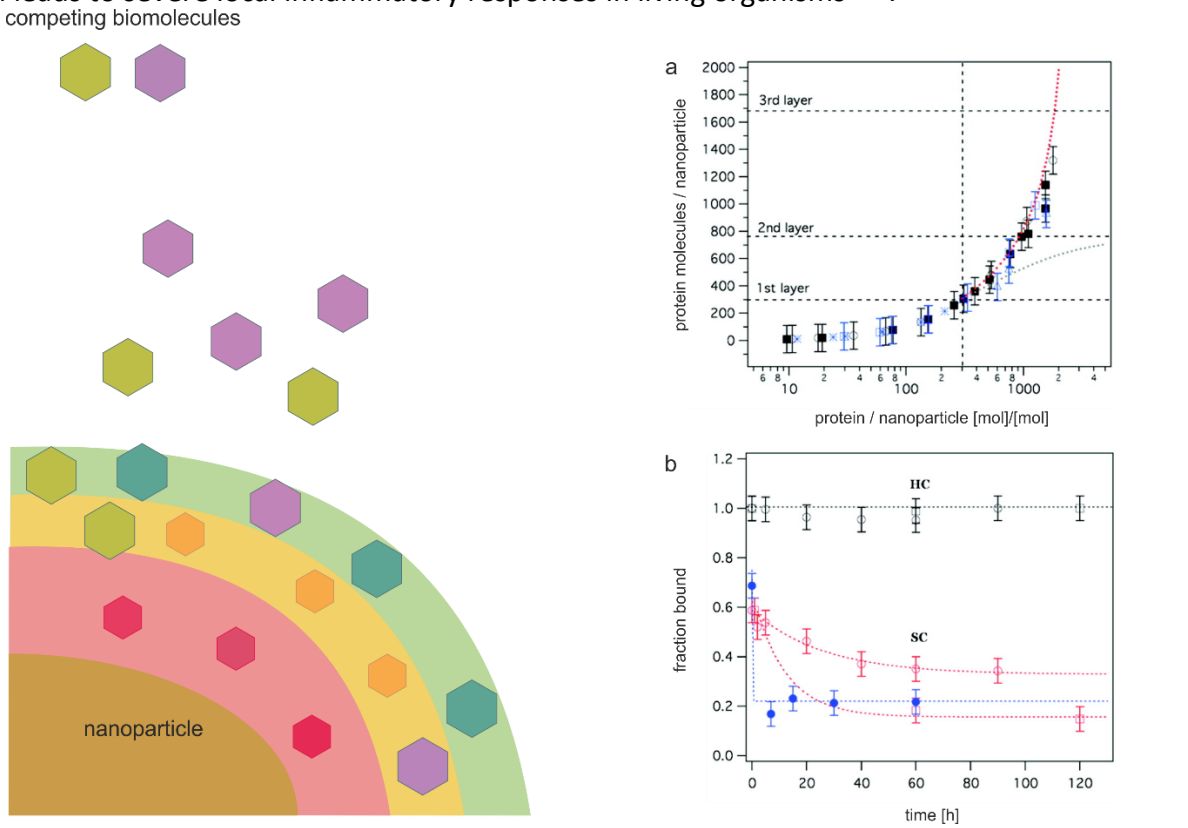

Figure 33: Schematic of the formation of the different layers of the protein corona. Proteins adsorb on the naked nanoparticle surface till saturation of the surface is reached. Further adsorption now happens in additional layers on top of the first protein layer till several layers are built. Fluorescence correlation spectroscopy of covered nanoparticles: a) Surface coverage in protein per nanoparticle. Predicted curves for monolayer model (grey dotted line) and multilayer model (red dotted line). Data clearly matches the multilayer model. b) Competitive unbinding of corona proteins in the presence of plasma proteins. No unbinding is visible for hard corona particles (black HC, circles 5% plasma, squares 10% plasma). In case of a labeled secondary layer the addition of plasma (blue and red circles 5% plasma for carboxyl-polystyrene and sulfonate polystyrene nanoparticles respectively, square 10% plasma to sulfonate polystyrene nanoparticles) removes the secondary layer completely or partially. Graphs with permission from [36]

Nanoparticles with a corona are identified by the organism by their corona constituents instead of particle material due to the near irreversible adsorption of the hard corona. Although small change of the hard corona has been reported over longer time scales and changing environments, the corona can be seen as mostly static [33a]. Nanoparticle fate is dictated by the corona to the point where nanoparticles with an artificial corona could be designed to enter specific parts of the body [14, 28, 31c, 33b, 39]. In addition, previously attached drug molecules on the particle are often blocked by the corona and hindered in their function [40]. In order to understand the implications of the protein corona a need for new experimental procedures arose. Lack of comparability of in vitro to in vivo experiments was shown by Sakulkhu and Hajidemetriou by comparing the corona formed in an in vitro assay and in vivo and finding only 10 % agreement between the two [41]. Lack of suitable test methods in vitro makes evaluation of the medical impact of nanoparticles and nanoparticle based drug delivery systems unreliable. It could be shown that gold nanoparticles hinder the formation of amyloid-ß-peptides, the aggregating peptide that is linked to Alzheimer's disease, in vitro [42]. In vivo however the observed effects are more diverse due to corona formation. Mirsadeghi discovered a reduction of fibril formation by blank nanoparticles, whereas gold nanoparticles with a native corona accelerated the process slightly [43]. The need for a deeper understanding of protein-nanoparticle interactions is further underlined by the fact that common toxicological assays are falsified by the presence of nanoparticles. The standard MTT assay for example shows 20% increased cytotoxicity values when iron oxide nanoparticles are present due to a mix of adsorption of the dye and redox interactions with it [44]. A similar effect is seen for the carboxymethylcellulose test for cellulase activity, where activity rises up to 100 % if iron oxide particles are present (data in this work).

Finally, the impact of adsorption on protein structure needs to be taken into account. Proteins adsorbing on nanoparticles are subject to high steric stress due to the curvature of the particle. This often leads to changes in secondary and tertiary structure and as a results of this in protein function. Deng could show that adsorption of fibrinogen on nanoparticles in vivo unfolds the protein, producing an inflammatory response and activating the immune system via the NF-κB signaling pathway [45]. Suitable methods for examining the structural changes to proteins upon adsorption to nanoparticles are circular dichroism (CD) [46], Fourier transformation infrared [47] and nuclear magnetic resonance [47]. In this work, the focus was on CD measurements.

4.1.3 Aims

Understanding the interaction between nanoparticles and proteins has been of growing interest since the phenomenon has been introduced to a wider audience by Klein 2007[30b]. Time evolution, composition and stability have been of equal interest as ways to modify the corona to the advantage of the nanomedical researcher. In addition to that, beneficial effects of immobilization of enzymes on nanoparticles have been observed, although detailed explanations and ways to predict behavior are still lacking. Here we aim to combine the current understanding of protein adsorption according to the protein corona model with enzymatic systems. We propose that non-covalent adsorption of cellulase on nanoparticles made of suitable materials such as silica or magnetite will result in a stable enzyme-nanoparticle system that retains the enzymes activity and can be used for biotechnological applications.

Building on the questions posed in chapter 3 we will try to design a cellulase-nanoparticle system that is suitable for cellulose conversion. We designed a set of experiments highlighting the feasibility of the approach, evaluates activity of cellulase after adsorption as well as after interaction with a completely covered nanoparticle. We will evaluate adsorption capacities of the corresponding particles, the effect adsorbing protein has on agglomeration properties of particles. We will test activity of the resulting conjugates using the ß-glucosidase activity assay as well as the carboxymethylcellulase assay commonly used to test for endoglucanase activity. Changes in enzyme structure after adsorption or interaction with nanoparticles will be evaluated using circular dichroism experiments.

4.2 Material and Methods

4.2.1 Chemicals

If not otherwise noted all chemicals were purchased from Sigma Aldrich, St. Louis, Missouri, USA. Cellulase was cloned and produced by ourselves using E.Coli BL21(DE3) bacteria.

4.2.2 Devices

All dynamic light scattering experiments were done using a Nanosight NS500 or a Zetasizer Nano from Malvern Instruments Ltd., Malvern, UK. Fluorescence experiments were done using a Synergy MX Multi Mode Reader from BioTek Inc. Wonooski, VT, USA. Protein concentration was measured using 280nm absorption and a Nanodrop 2000c from Thermo Fischer Scientific Inc., Waltham, Massachusetts, USA. Circular Dichroism measurements were carried out using a Chirascan-Plus CD spectrometer from Applied Photophysics Ltd. Surrey, UK.

4.2.3 ß-D-Glucosidase assay with nanoparticles

ß-D-glucosidase activity was measured using a modified assay after Zhang et al [48]. In short cellulase (24 nmol/ml) in 1xPBS buffer (pH 7) was incubated with previously sonicated nanoparticles in the same buffer for 15 minutes while shaking. After separation of the unbound fraction from the bound fraction via centrifugation (silica nanoparticles) or magnetic separation (magnetite particles) the remaining nanoparticle containing fraction was washed three times with 1xPBS buffer and resuspended in the same. The enzyme concentration was determined using the enzyme concentration of the supernatant and assuming that all missing enzyme was bound on the nanoparticles. All samples, supernatant as well as nanoparticle suspension, where diluted with 1xPBS to a final enzyme concentration of 1.2 nmol/ml of cellulase. 100 µl of each sample was incubated with 100 µl of 2 mM 4-nitrohenol-ß-D-cellobiosid in 0.05 M sodium acetate buffer (pH 5) for 30 min at 50°C. The reaction was stopped by adding another 100 µl of 1 M sodium carbonate buffer and the activity was measured versus a concentration range of 4-nitrophenol in a 1:1 mixture of 1x PBS and 0,05 M sodium acetate buffer at 405 nm at RT.

4.2.4 Dinitrosalicylic acid carboxymethylcellulose assay

Endoglucanase activity was evaluated using the carboxymethylcellulose (CMC) substrate and 3,5-dinitrosalicylic acid (DNS) reagent. DNS reagent is prepared by dissolving 10.6 g of DNS with 19.8 g of sodium hydroxide in 1.5 l of water. After complete dissolution 360 g of sodium potassium tartrate, 7.6 ml of molten phenol (at 50°C) and 8.3 g of sodium metabisulfite was added and mixed. Nanoparticle-enzyme conjugates were produced by adding cellulase (24 nmol/ml) in 1xPBS buffer (pH 7) to a suspension of silica nanoparticles (1 mg/ml) in 50 mM citrate buffer (pH 4.8) and incubating for 15 min while shaking. After separation of unbound enzyme from the nanoparticles via centrifugation the silica nanoparticles where washed three times with 50 mM citrate buffer (pH 4.8) and resuspended in the same. The resulting supernatant and enzyme-nanoparticle-conjugate suspension where diluted to a final enzyme concentration of 1.2 nmol/ml with 50 mM citrate buffer (pH4.8). To 25µl of the sample, 25µl of 2% (w/v) CMC in 50 mM citrate buffer (pH 4.8) was added and incubated at 50°C for 30 minutes. After adding 150µl of the DNS reagent the samples were boiled at 95°C for 5 minutes and cooled down in ice. Enzyme activity was evaluated versus a glucose concentration curve having undergone the same reaction conditions at 540 nm. Due to the nature of the assay (redox reaction) the assay is not suitable for magnetite particles since they produce a similar reaction as the sugar would.

4.3 Results

4.3.1 Immobilization of cellulase on nanoparticles using the protein corona effect

The effectiveness of enzyme adsorption was tested on two different nanoparticle materials, magnetite and silica. Two different sizes of silica nanoparticles with primary particle sizes of 12 nm and 40 nm were used to test for size influence on adsorption. Magnetite nanoparticles were at a primary particle size of 11 nm. Adsorption was measured by incubating increasing amounts of nanoparticles with a fixed amount of enzyme and measuring remaining protein concentration in the supernatant. Adsorption followed classical saturation behavior (Figure 34) and allowed for a saturation prediction of all three particles. 12 nm silica particles were saturated at 5.5 µg enzyme per 40 µg particles, 40 nm silica 5.75 µg enzyme per 140 µg particles and magnetite 4.6 µg enzyme per 60 µg particles. This results to ~139 ng enzyme per µg particles for 12 nm silica nanoparticles, ~57 ng/µg for 40 nm silica particles and ~102 ng/µg for magnetite. Variation in adsorption values indicates heterogeneous agglomeration populations in the sample underlining the necessity of sonication in order to homogenize the particle agglomerates. This is also the reason that no 100% adsorption was reached in these experiments.

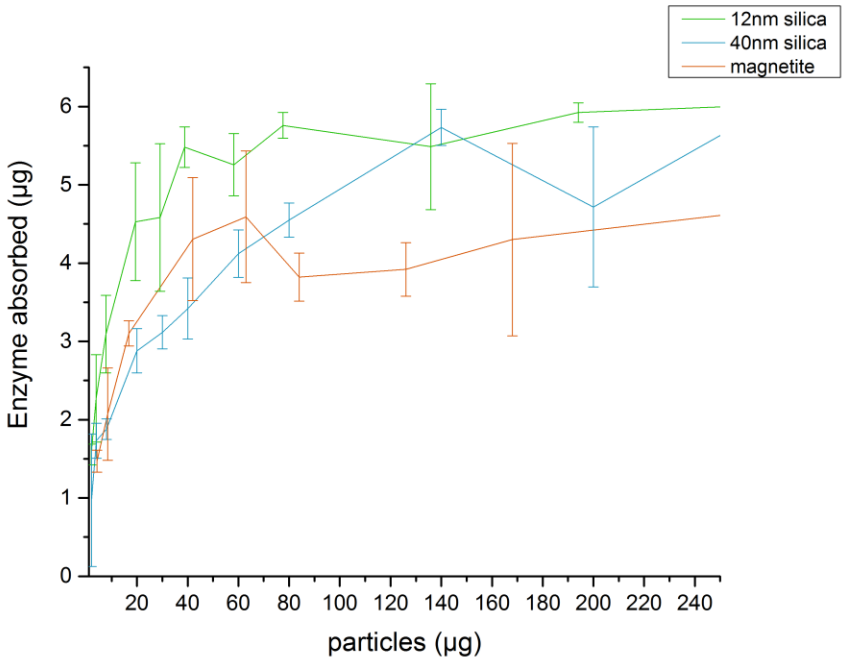

Figure 34: Adsorption of enzyme on different kinds of nanoparticles. Available enzyme was kept constant at 6 µg for silica particles and 5.5 µg for magnetite as the amount of particles per volume was increased stepwise from experiment to experiment.

Additional information on agglomeration behavior was gathered using nanotracking technology (NTA), a variant of the dynamic light scattering technique that allows for size analysis of complex heterogeneous samples. Two different statistical numbers are used to discuss the data, the D50 value and the mode. The D50 value is defined as the data point where 50 % of a population of particles is larger, and 50 % is smaller than the D50 value. The mode is defined as the most abundant data point in a population. D50 values of the used particles range from 275.9 nm for the 40 nm silica particles, 206.6 nm for magnetite particles to 166.3 nm for 12 nm silica particles. 12 nm silica and 10 nm magnetite nanoparticles should deliver smaller hydrodynamic

radii than the 40 nm silica particles which they do. The differences are however not as pronounced as expected and do not mirror the difference in primary particle size. Comparing 12 nm silica particles with 40 nm silica particles we expect the larger silica particles to deliver hydrodynamic radii that are roughly 3.3 times larger than the smaller 12 nm particles. Indeed we observe a difference by a factor of 1.6. This highlights the increased tendency of smaller nanoparticles to agglomerate. There is a small difference between magnetite and silica particles in agglomeration tendency as well. Magnetite nanoparticles deliver hydrodynamic radii that are 74% of the average size of 40 nm silica, three times larger than expected. Since the magnetite particles have a primary size of 10 nm this might however be either an effect of material or the even smaller size.

Table 2: Comparison of Zeta potential values, mode and D50 values of 40nm silica, magnetite and 12nm silica particles

	40 nm silica particle		*magnetite particle*		*12 nm silica particle*	
	blank	with cellulase	blank	with cellulase	blank	with cellulase
Zeta [mV]	-25.2±0.1	-16.5±0.0	2.0±0.0	-23.0±0.0	20.3±0.1	-12.4±0.0
Mode [nm]	314.3±12.6	206.0±24.2	183.3±33.9	140.6±23.7	172.4±11.0	209.3±35.3
D50 [nm]	275.9±0.2	239.8±13.3	206.6±12.3	126.6±12.3	166.3±15.0	225.5±11.5

Figure 35 highlights the heterogeneous distribution of agglomerates within the different particle preparations. The native 12 nm silica particles the most homogeneous with the majority of particles being in the range of 166.3 nm. A dramatic increase in heterogeneity occurs when the particles are incubated with cellulase.

Hydrodynamic radii decreased after adsorption of cellulase with the exception of 12 nm silica particles. Generally less aggregation after protein adsorption on the particles is expected. This is due to the fact that the increase in size that results from the adsorption of a protein layer reduces the volume to surface ratio, reducing surface energy/tension and thereby decreasing the entropic benefit the aggregation normally provides. This seems to be most prominent with the larger 40 nm silica. Despite the reduction in surface charge, and therefore less repulsion of the particles to each other, the agglomeration is reduced, D50 and mode values are decreased. The same magnitude of net surface charge is observed with the smaller silica particles, but the average size indicators increase. Here the entropy driven reduction in agglomeration seems to be negated by the loss of net surface charge. Magnetite nanoparticles show a dramatic net increase in surface charge, resulting in reduced average agglomeration size

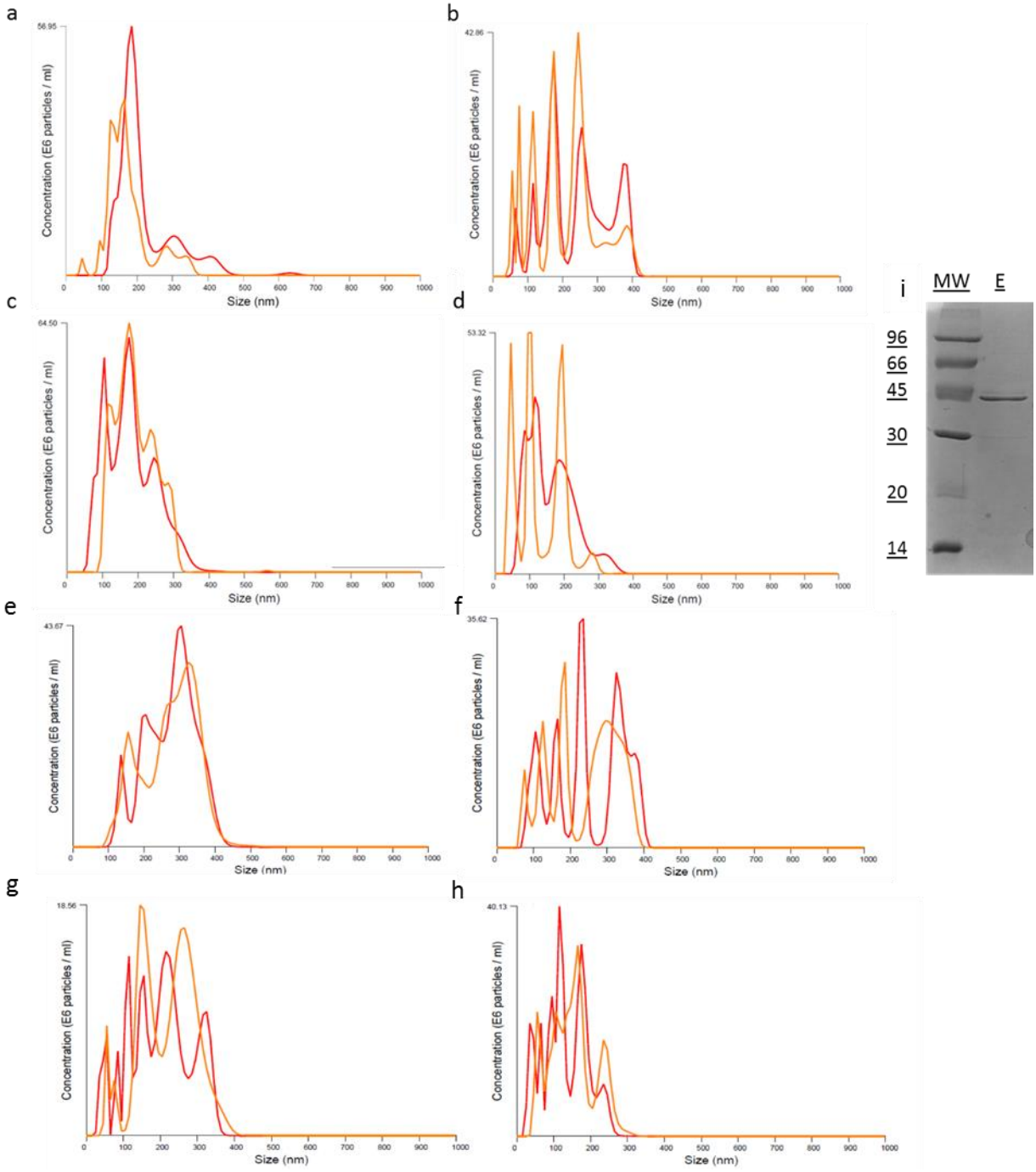

Figure 35: Influence of cellulase adsorption on agglomeration behavior of nanoparticles measured with NTA. Double measurements showed, red= first measurement, orange = second measurement a) 12 nm silica particles without enzyme, b) 12 nm silica particles with cellulase corona, c) cellulase removed after incubation with 12 nm silica particles. d) native cellulase. e) 40 nm silica particles without enzyme. f) 40 nm silica particles with cellulase corona. g) magnetite particles without enzyme. h) magnetite particles with cellulase corona. i) SDS gel of purified recombinantly expressed cellulase (E) with MW = 41426.1 Da

Zeta potential shifts dramatically towards negative values for the two smaller particles, where it surprisingly shifts towards a more positive value for the 40 nm silica particles. Magnetite particles surface potential changes from 2 mV to -23 mV, explaining the large decrease in agglomerate size from 183 to 140 nm average and a complete loss of all species larger 300 nm (data not shown). 12nm Silica undergoes an even more dramatic change with a net change of 32.7 mV from 20.3 mV down to -12.4 mV. While this change is dramatic it moves the zeta potential more towards neutrality, resulting in a less charged surface. Neutral surfaces of nanoparticles result in increased agglomeration since the neutrally charged particles are attracted to each other over the polar surrounding solvent.

4.3.2 Activity of immobilized cellulase

To determine if cellulase remains active after adsorption on nanoparticles two standard cellulase activity assays were used: the p-nitrophenole-ß-D-cellobiosid assay for ß-D-glucosidase activity and the carboxymethyl cellulose (CMC) assay for endoglucanase activity (Figure 36) [48]. Both assays use optical detection for quantification of enzymatic activity. The cellulase used during all experiments is a recombinantly expressed endoglucanase originally from *fervidobacterium islandicum*.

The ß-D-glucosidase assay tests for cleavage of a ß-D-glycosidic bond. The substrate has a p-nitrophenole moiety attached to a cellobiosid via a ß-D-glycosidic bond. As soon as the p-nitrophenole is enzymatically cleaved from the glucose dimer which in turn is detected and quantified via UV/VIS spectrometry. The CMC assay uses dinitrosalicylic acid to test for reducing sugars. In the substrate there are no free acetale OH groups resulting in no redox reaction between DNS and the polymer. Cleavage of glycosidic bonds results in smaller polymer fragments having reducing sugars at their end, which in turn react with the DNS. DNS is reduced to 3-nitro, 5-aminosalicylic acid which is then detected.

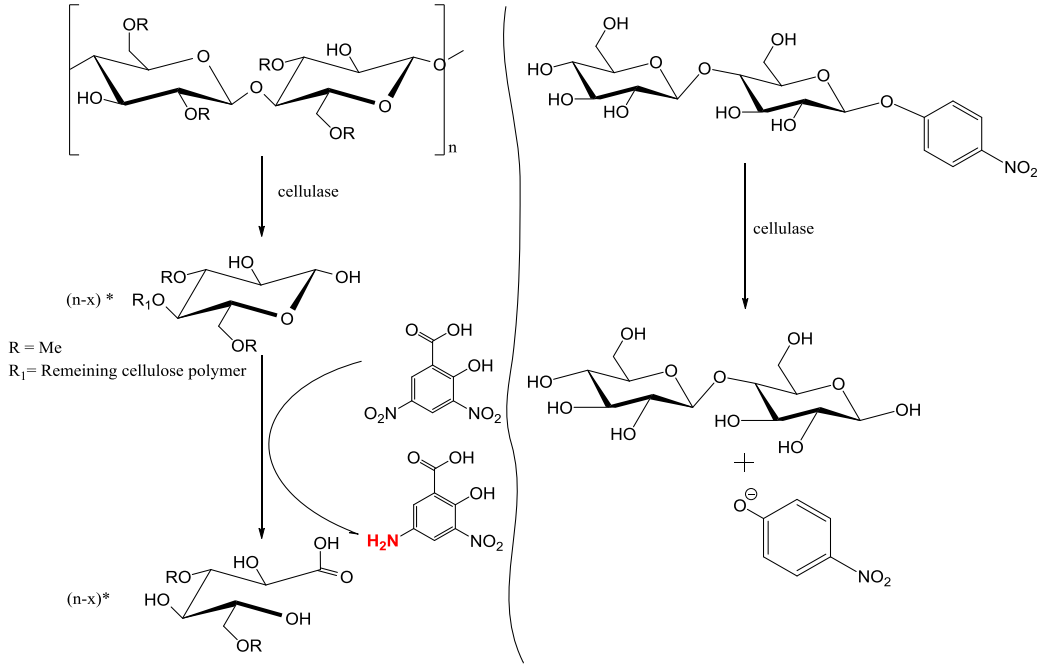

Figure 36: Schematic of used cellulase activity assays. LEFT: Carboxymethylcellulase assay for endoglucanase activity. The enzyme cleaves the polymeric glucose into smaller polymers that are then treated with a reaction mixture containing dinitrosalicylic acid. In a redox reaction, the sugar is oxidized and the dinitrosalicylic acid is reduced to 3-nitro, 5-aminosalicylic acid. RIGHT: 4-nitrophenyl-ß-D-cellobioside is enzymatically cleaved into 4-nitrophenol (yellow) and cellobiosid.

Early experiments showed high retained enzymatic activity of cellulase after adsorption on nanoparticles (Figure 37). Quantification of remaining activity of adsorbed enzyme proved to be challenging due to large experimental variation. It was possible to reduce variation dramatically by reducing agglomeration with three minutes of sonication, and by using lower enzyme concentrations to compensate for the high activity of the cellulase from *fervidobacterium islandicum*. Further experiments were done with a maximum of 3.5 µg/ml of free or immobilized enzyme, adjusted for each experiment to the same concentration to account for actual adsorption to. Activity was calculated by comparing absorbance values of native enzyme to all other enzyme variants.

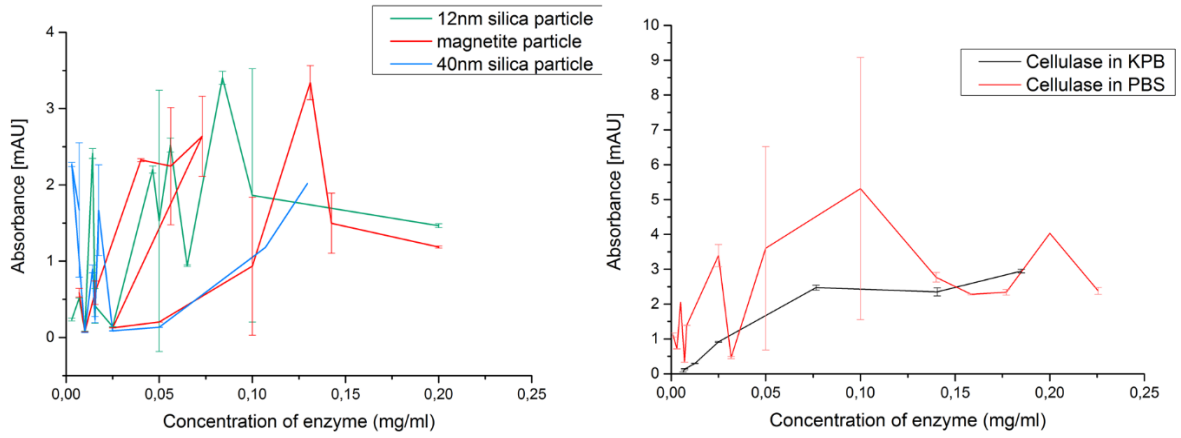

Figure 37: ß-D-glucosidase assay of cellulase-particle conjugates (left) and native cellulase (right). Due to the exceptionally high activity of the fervidobacterium islandicum cellulase and inconsistent adsorption rates onto the particles due to agglomeration, variation of the experiments is too high for activity calculation. [n=3-10]

Adsorption values of the enzyme and relative activity values observed remained exceptionally high, less detrimental effect of immobilization than expected (Figure 38). Cellulase adsorbed on magnetite nanoparticles showed levels of activity comparable to those of the native enzyme. Cellulase adsorbed on the different silica particles showed a decrease in activity of average 40 % for the 12 nm silica nanoparticles and average 35 % for the 40 nm ones. Adsorbed cellulase, irrespective of particle size and material, shows a surprising increase in comparative activity at low enzyme concentrations. A maximum of activity seems to be reached at 3.75 µg/ml per 0.2 mM substrate suspension where a comparative ß-glucosidase activity of 147 % (12 nm silica) up to 259 % (magnetite) is found. This result might seem counterintuitive at first but the nanoparticles could help attracting the substrate to a small extent, or increase enzyme movement due to Brownian motion, effects that might be more pronounced the smaller the concentration of enzyme [49]. An additional effect that can explain the cellulase behavior is located in the enzymes cellusomal origin, where it works attached to a large organelle with defined spaces between different cellulase types along a cohesin molecule. Adsorption on nanoparticles might therefore resemble the original setup of the enzyme. Lower concentrations seem to be better than high loading of the particle hinting at less complete coverage of the particle better mimics the optimal spatial requirements of the enzyme.

In order to guarantee saturation of the nanoparticle surface with cellulase an excess of two times the theoretical particle loading capacity was used. Unbound enzyme was removed via magnetic sedimentation or centrifugation as applicable. Absence of particles in the supernatant was verified by environmental scanning electron microscopy (ESEM) and DLS. Unbound cellulase was evaluated for changes in activity as well. A change in activity of unbound enzyme is expect due to possible changes to the enzyme via protein-protein interaction with the cellulase layer on the nanoparticle. Increases of comparative activity for unbound cellulase from 108 % to 186 % could be observed. The change is dependent on concentration and type of particle material conjugate the free enzyme interacted with. While the change in activity was positive for all tested concentrations there seems to be an optimal enzyme to substrate ratio between 12.5 µg/ml and 25 µg/ml.

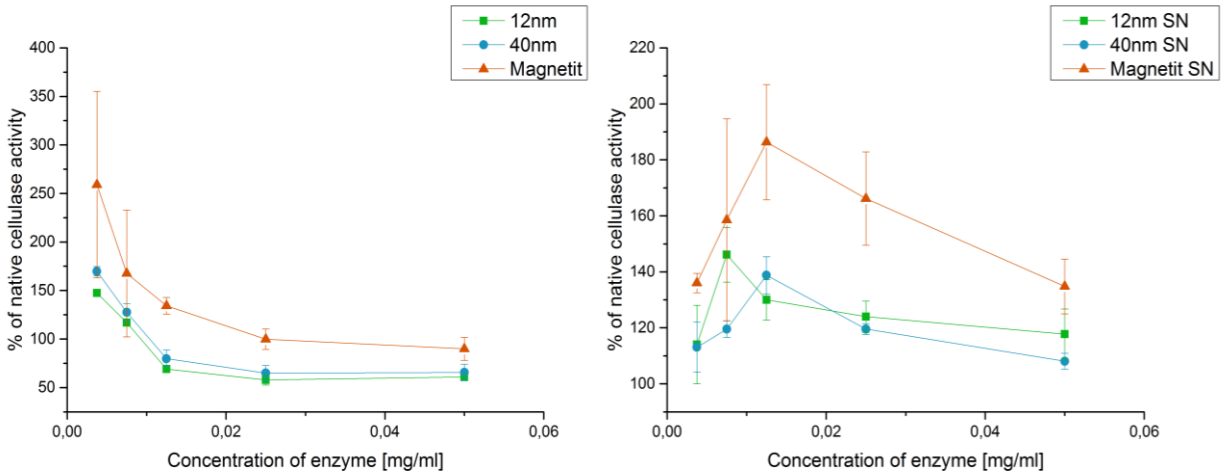

Figure 38: Average ß-D-glucosidase activity of endoglucanase from fervidobacterium islandicum immobilized on nanoparticles (left) as well as the unbound enzyme in the supernatant (SN) (right). Shown are experiments using 12nm silica particles (12nm) 40nm silica particles as well as 10nm magnetite particles. Substrate concentration was the same in all experiments at 0.2mM

In order to test for endoglucanase activity a new setup based on the CMC-DNS assay was evaluated. Experiments using this reductive sugar assay for endoglucanase activity showed exactly reversed effects to what was observed for ß-glucosidase activity before. Whereas the comparative activity of free enzyme was reduced, immobilized cellulase showed increased comparative endoglucanase activity (Figure 39). This is especially positive since for biotechnological applications endoglucanase activity is of higher importance. Experimental variation of the supernatant from 12 nm silica nanoparticle experiments was surprisingly high and consistent hinting at an irregular interaction pattern that could not be further explained. Data for magnetite based enzyme-particle-conjugates could not be obtained since the redox active surface of the magnetite particles produced false positive results, making reliable measurements impossible.

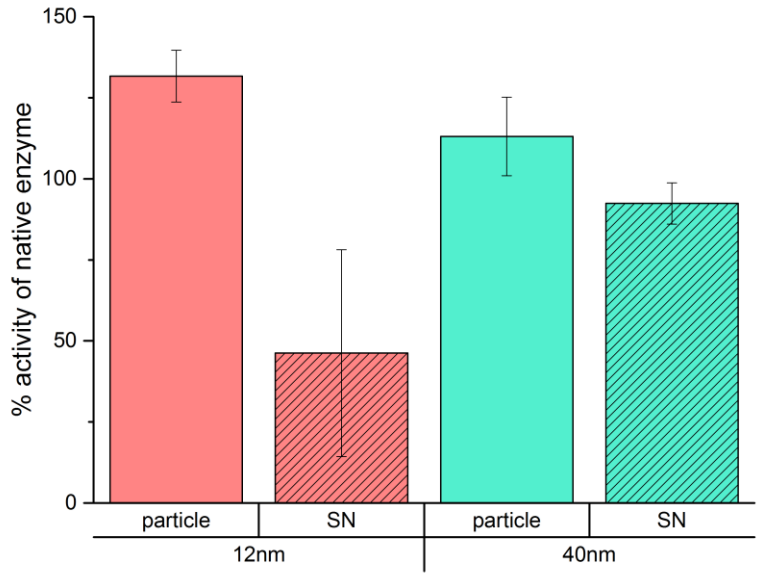

Figure 39: Relative activity of cellulase immobilized on different nanoparticles or unbound cellulase from the supernatant of the immobilization experiments. n=9

4.3.3 Influence of enzyme adsorption on enzyme structure

In order to determine the reasons for the changes in relative activity after immobilization on or interaction with nanoparticles a set of circular dichroism experiments was done. We measured the CD spectra of native cellulase versus immobilized cellulase and unbound cellulase from the supernatant of the immobilization experiments. Due to the minimum required enzyme concentrations for CD experiments it was impossible to include cellulase adsorbed on magnetite nanoparticles in the setup. The amount of particles in the solution required colored the solution to an extent where CD measurements were no longer possible (Figure 40 1-3).

Immobilization of cellulase on silica nanoparticles resulted in drastic changes of secondary protein structure. Cellulase immobilized on 12 nm silica nanoparticles showed a significant increase in α-helical content from 22 % to 27 % and a loss of ß-sheet structures of 15% that went along with an 3 % increase in ß-turn and an 12 % increase of unstructured regions. Cellulase immobilized on 40 nm silica particles displayed a significant increase in ß-sheet structures from 25 % to 31 % and a loss of a-helical structures from 22 % down to 11 %. Loss of defined structure was less pronounced with an increase of unstructured regions of 4 %. This indicates a generally more disrupting effect of the smaller particle on the enzyme due to the large loss of structured sequences. The cellulase on 40 nm silica particles on the other hand shows more of a rearrangement to a different structure shifting a-helical parts of the protein towards a higher ß-sheet content. ß-sheets are generally accepted as an indicator for increased protein stability, an increase in the stability of the enzyme might be the result. This is not necessarily true for the activity of the enzyme.

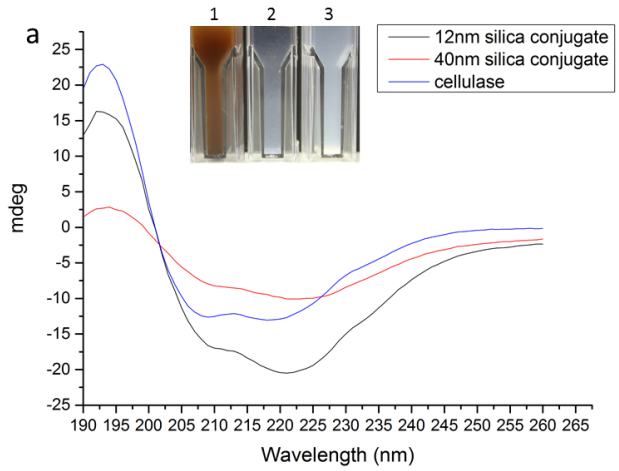

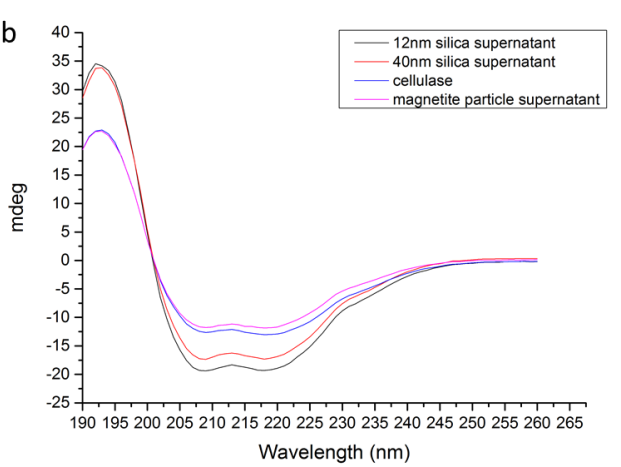

	cellulase	12 nm particles	40 nm particles
Helix	22%	27%	11%
Antiparallel	25%	10%	34%
Parallel	7%	7%	4%
Beta-Turn	19%	15%	19%
Rndm. Coil	28%	40%	32%
Total Sum	101%	99%	100%

	cellulase	12 nm SN	40 nm SN	magnetite SN
Helix	22%	31 %	35%	21%
Antiparallel	25%	8%	8%	24%
Parallel	7%	8%	8%	6%
Beta-Turn	19%	18%	17%	19%
Rndm. Coil	28%	31%	29%	31%
Total Sum	101%	96%	97%	101%

Figure 40: Overview of the CD Data and spectra for a) enzymes immobilized on nanoparticles and b) unbound enzymes. 1) magnetite particle-enzyme suspension, 2) 12 nm silica particle-enzyme suspension, 3) 40 nm silica particle-enzyme suspension

Enzymes in the supernatant showed less pronounced overall changes in the spectra. Cellulase from silica immobilization experiments showed an increase of α-helical structures and a loss of ß-sheet structures. There is however, no significant increase in unstructured content in the spectrum. There is therefore a less pronounced but significant change in the structure of the enzyme after interaction with the hard corona of silica particles but it seems to be less disruptive for the enzyme compared to complete adsorption. Cellulase from the magnetite immobilization experiments undergo no drastic changes at all retaining roughly the same structure as before with minimal changes to the native enzyme structure. This is especially interesting since these cellulases show the highest increase in relative ß-glucosidase activity. The more dramatic changes of the immobilized cellulase seem to reflect a positive effect on endoglucanase activity, hinting at a better access to large substrates, whereas the catalysis of smaller substrates in the ß-glucosidase assay is hampered.

4.4 Conclusion

We were able to functionally adsorb cellulase on 12 nm silica, 40 nm silica and 10 nm magnetite nanoparticles. In previous attempts to attach cellulase to solid supports, the activity of the enzyme was reduced significantly. Cellulase immobilized to nanoparticles however, retained a large percentage of its native activity, in some cases even surpassing that of the native enzyme. Surprisingly, cellulase immobilized on nanoparticles shows ß-glucosidase activities of up to 259 % compared to the native enzyme for very low enzyme to substrate ratios. For higher enzyme concentrations, cellulase still retained 60 to 100 % of its native activity depending on the particle material used. CD data shows significant structural changes for cellulase after adsorption on silica nanoparticles with a tendency towards more unstructured secondary structures. No CD data could be obtained for cellulase adsorbed on magnetite nanoparticles due to high optical density of suspensions containing magnetite (brown coloring).

Unbound cellulase showed significantly increased ß-glucosidase activity. Relative ß-glucosidase activities of 108 % to 186 % were observed with a maximum at moderate enzyme to substrate ratios. Relative activities remained higher than 100% regardless of enzyme to substrate ratio. The moderate changes to the enzymatic structure indicate a small effect of structural changes at best. This is further underlined by the fact that the most active enzyme is the unbound supernatant cellulase from the magnetite immobilization experiments where structural changes are very small. This hints at a different effect resulting in the increase of activity. A protein corona promoted formation of larger agglomerates of cellulase might be responsible for the increase in activity here, since cellulase from fervidobacterium islandicum natively works within a cellusomal multi-enzyme complex.

Relative endoglucanase activity on the other did not only reach native enzyme levels but surpassed them. The native enzymes main activity therefore is boosted by the immobilization of the enzyme to a small solid structure. The structural changes or the close proximity to other cellulases seem to be beneficial for hydrolysis of the large substrate of carboxymethylcellulose in the scissor-like active site of the enzyme. An additional explanation might be a stabilizing effect of the particle against the large polymeric substrate, therefore stabilizing the active site.

In contrast to the increase in endoglucanase activity of immobilized cellulase, unbound cellulase showed reduced endoglucanase activity. The beneficial effects of the constant protein-protein interaction of the protein corona seems to be detrimental for hydrolysis of large substrates.

In summary, it was possible to show the feasibility of a nanoparticle-cellulase construct based on physical adsorption of cellulase on small nanoparticles using the adsorption effect called protein corona. The resulting particle-enzyme complex retains at least 60% of its activity, depending on the particle materials the activity could be retained at 100% or more for all activity assays. Immobilization delivers improved catalytic activity of the endoglucanase from fervidobacterium islandicum hinting at a stabilizing effect of the particle as well as beneficial conformational changes to the enzyme during adsorption. Weak protein-protein interactions allow for dramatic increases in side activity of the cellulase while the main activity of the enzyme is reduced compared to the native enzyme. This hints at an effect that increases turnover for small substrates and hinders the hydrolysis of large substrates. The system of nanoparticle immobilization for pseudo-homogeneous catalysis using cellulase is established. Further experiments need to show stability of the system under conditions present in commercial

applications of cellulase as well as further delve into the reasons for the striking activity changes of the enzyme during interaction with nanoparticles. The latter can be evaluated using structural NMR as well as more precise particle characterization techniques such as sedimentation disc centrifugation to understand the adsorption timeline and effects.

4.5 Literature

[1] P. Fortina, L. J. Kricka, D. J. Graves, J. Park, T. Hyslop, F. Tam, N. Halas, S. Surrey, S. A. Waldman, *Trends in Biotechnology* **2007**, *25*, 145-152.

[2] P. Tartaj, M. P. Morales, T. González-Carreño, S. Veintemillas-Verdaguer, C. J. Serna, *Journal of Magnetism and Magnetic Materials* **2005**, *290–291, Part 1*, 28-34.

[3] M. Cushen, J. Kerry, M. Morris, M. Cruz-Romero, E. Cummins, *Trends in Food Science & Technology* **2012**, *24*, 30-46.

[4] L. Mu, R. L. Sprando, *Pharmaceutical research* **2010**, *27*, 1746-1749.

[5] M. R. Jones, K. D. Osberg, R. J. Macfarlane, M. R. Langille, C. A. Mirkin, *Chemical Reviews* **2011**, *111*, 3736-3827.

[6] H. Dai, E. W. Wong, Y. Z. Lu, S. Fan, C. M. Lieber, *Nature* **1995**, *375*, 769-772.

[7] S. Chen, Z. Fan, D. L. Carroll, *The Journal of Physical Chemistry B* **2002**, *106*, 10777-10781.

[8] Y. Sun, Y. Xia, *Science* **2002**, *298*, 2176-2179.

[9] L. R. Hirsch, R. J. Stafford, J. A. Bankson, S. R. Sershen, B. Rivera, R. E. Price, J. D. Hazle, N. J. Halas, J. L. West, *Proceedings of the National Academy of Sciences* **2003**, *100*, 13549-13554.

[10] K. Pandian Senthil, P.-S. Isabel, R.-G. Benito, F. J. G. d. Abajo, M. L.-M. Luis, *Nanotechnology* **2008**, *19*, 015606.

[11] Y. Malam, M. Loizidou, A. M. Seifalian, *Trends in Pharmacological Sciences* **2009**, *30*, 592-599.

[12] C. Solans, P. Izquierdo, J. Nolla, N. Azemar, M. J. Garcia-Celma, *Current Opinion in Colloid & Interface Science* **2005**, *10*, 102-110.

[13] F. Lao, L. Chen, W. Li, C. Ge, Y. Qu, Q. Sun, Y. Zhao, D. Han, C. Chen, *Acs Nano* **2009**, *3*, 3358-3368.

[14] N. V. Konduru, Y. Y. Tyurina, W. Feng, L. V. Basova, N. A. Belikova, H. Bayir, K. Clark, M. Rubin, D. Stolz, H. Vallhov, A. Scheynius, E. Witasp, B. Fadeel, P. D. Kichambare, A. Star, E. R. Kisin, A. R. Murray, A. A. Shvedova, V. E. Kagan, *PLoS ONE* **2009**, *4*, e4398.

[15] D. L. Huber, *Small* **2005**, *1*, 482-501.

[16] L. Nguyen Viet, C. Nguyen Duc, H. Tomokatsu, H. Hirohito, L. Gandham, N. Masayuki, *Nanotechnology* **2010**, *21*, 035605.

[17] V. Biju, T. Itoh, A. Anas, A. Sujith, M. Ishikawa, *Analytical and Bioanalytical Chemistry* **2008**, *391*, 2469-2495.

[18] A. S. Nikolov, P. A. Atanasov, D. R. Milev, T. R. Stoyanchov, A. D. Deleva, Z. Y. Peshev, *Appl Surf Sci* **2009**, *255*, 5351-5354.

[19] J. P. Rao, K. E. Geckeler, *Progress in Polymer Science* **2011**, *36*, 887-913.

[20] S. Nimesh, A. Goyal, V. Pawar, S. Jayaraman, P. Kumar, R. Chandra, Y. Singh, K. C. Gupta, *Journal of Controlled Release* **2006**, *110*, 457-468.

[21] T. P. Thomas, A. K. Patri, A. Myc, M. T. Myaing, J. Y. Ye, T. B. Norris, J. R. Baker, *Biomacromolecules* **2004**, *5*, 2269-2274.

[22] aX.-L. Huang, B. Zhang, L. Ren, S.-F. Ye, L.-P. Sun, Q.-Q. Zhang, M.-C. Tan, G.-M. Chow, *Journal of Materials Science: Materials in Medicine* **2008**, *19*, 2581-2588; bE. Fabian, R. Landsiedel, L. Ma-Hock, K. Wiench, W. Wohlleben, B. van Ravenzwaay, *Arch Toxicol* **2008**, *82*, 151-157; cW. H. De Jong, W. I. Hagens, P. Krystek, M. C. Burger, A. J. A. M. Sips, R. E. Geertsma, *Biomaterials* **2008**, *29*, 1912-1919; dJ.-T. Kwon, S.-K. Hwang, H. Jin, D.-S. Kim, A. Minai-Tehrani, H.-J. Yoon, M. Choi, T.-J. Yoon, D.-Y. Han, Y.-W. Kang, B.-I. Yoon, J.-K. Lee, M.-H. Cho, *Journal of Occupational Health* **2008**, *50*, 1-6.

[23] C. A. Poland, R. Duffin, I. Kinloch, A. Maynard, W. A. H. Wallace, A. Seaton, V. Stone, S. Brown, W. MacNee, K. Donaldson, *Nat Nano* **2008**, *3*, 423-428.

[24] aH. Nabeshi, T. Yoshikawa, K. Matsuyama, Y. Nakazato, K. Matsuo, A. Arimori, M. Isobe, S. Tochigi,

S. Kondoh, T. Hirai, T. Akase, T. Yamashita, K. Yamashita, T. Yoshida, K. Nagano, Y. Abe, Y. Yoshioka, H. Kamada, T. Imazawa, N. Itoh, S. Nakagawa, T. Mayumi, S.-i. Tsunoda, Y. Tsutsumi, *Biomaterials* **2011**, *32*, 2713-2724; bH. Gehrke, A. Fruhmesser, J. Pelka, M. Esselen, L. L. Hecht, H. Blank, H. P. Schuchmann, D. Gerthsen, C. Marquardt, S. Diabate, C. Weiss, D. Marko, *Nanotoxicology* **2013**, *7*, 274-293.

[25] K. Yamashita, Y. Yoshioka, K. Higashisaka, K. Mimura, Y. Morishita, M. Nozaki, T. Yoshida, T. Ogura, H. Nabeshi, K. Nagano, Y. Abe, H. Kamada, Y. Monobe, T. Imazawa, H. Aoshima, K. Shishido, Y. Kawai, T. Mayumi, S.-i. Tsunoda, N. Itoh, T. Yoshikawa, I. Yanagihara, S. Saito, Y. Tsutsumi, *Nat Nano* **2011**, *6*, 321-328.

[26] J. REJMAN, V. OBERLE, I. S. ZUHORN, D. HOEKSTRA, *Biochemical Journal* **2004**, *377*, 159-169.

[27] H. Maeda, J. Wu, T. Sawa, Y. Matsumura, K. Hori, *J Control Release* **2000**, *65*, 271-284.

[28] M. P. Monopoli, C. Aberg, A. Salvati, K. A. Dawson, *Nat Nanotechnol* **2012**, *7*, 779-786.

[29] aE. V. Amirgoulova, J. Groll, C. D. Heyes, T. Ameringer, C. Röcker, M. Möller, G. U. Nienhaus, *ChemPhysChem* **2004**, *5*, 552-555; bC. D. Heyes, A. Y. Kobitski, E. V. Amirgoulova, G. U. Nienhaus, *The Journal of Physical Chemistry B* **2004**, *108*, 13387-13394; cE. Ostuni, R. G. Chapman, R. E. Holmlin, S. Takayama, G. M. Whitesides, *Langmuir* **2001**, *17*, 5605-5620.

[30] aT. Cedervall, I. Lynch, S. Lindman, T. Berggård, E. Thulin, H. Nilsson, K. A. Dawson, S. Linse, *Proceedings of the National Academy of Sciences* **2007**, *104*, 2050-2055; bJ. Klein, *Proceedings of the National Academy of Sciences* **2007**, *104*, 2029-2030.

[31] aK. K. Nanda, A. Maisels, F. E. Kruis, H. Fissan, S. Stappert, *Phys Rev Lett* **2003**, *91*; bM. A. Dobrovolskaia, A. K. Patri, J. W. Zheng, J. D. Clogston, N. Ayub, P. Aggarwal, B. W. Neun, J. B. Hall, S. E. McNeil, *Nanomed-Nanotechnol* **2009**, *5*, 106-117; cM. Lundqvist, J. Stigler, G. Elia, I. Lynch, T. Cedervall, K. A. Dawson, *Proceedings of the National Academy of Sciences* **2008**, *105*, 14265-14270; dS. Tenzer, D. Docter, S. Rosfa, A. Wlodarski, J. Kuharev, A. Rekik, S. K. Knauer, C. Bantz, T. Nawroth, C. Bier, J. Sirirattanapan, W. Mann, L. Treuel, R. Zellner, M. Maskos, H. Schild, R. H. Stauber, *Acs Nano* **2011**, *5*, 7155-7167.

[32] aE. Casals, T. Pfaller, A. Duschl, G. J. Oostingh, V. Puntes, *Acs Nano* **2010**, *4*, 3623-3632; bD. Dell'Orco, M. Lundqvist, C. Oslakovic, T. Cedervall, S. Linse, *PLoS ONE* **2010**, *5*, e10949.

[33] aM. Lundqvist, J. Stigler, T. Cedervall, T. Berggard, M. B. Flanagan, I. Lynch, G. Elia, K. Dawson, *Acs Nano* **2011**, *5*, 7503-7509; bC. Schleh, M. Semmler-Behnke, J. Lipka, A. Wenk, S. Hirn, M. Schaffler, G. Schmid, U. Simon, W. G. Kreyling, *Nanotoxicology* **2012**, *6*, 36-46; cJ. V. Georgieva, D. Kalicharan, P.-O. Couraud, I. A. Romero, B. Weksler, D. Hoekstra, I. S. Zuhorn, *Mol Ther* **2011**, *19*, 318-325.

[34] E. Hellstrand, I. Lynch, A. Andersson, T. Drakenberg, B. Dahlbäck, K. A. Dawson, S. Linse, T. Cedervall, *FEBS Journal* **2009**, *276*, 3372-3381.

[35] L. Vroman, A. L. Adams, *Journal of Biomedical Materials Research* **1969**, *3*, 43-67.

[36] S. Milani, F. Baldelli Bombelli, A. S. Pitek, K. A. Dawson, J. Rädler, *Acs Nano* **2012**, *6*, 2532-2541.

[37] A. Lesniak, F. Fenaroli, M. P. Monopoli, C. Åberg, K. A. Dawson, A. Salvati, *Acs Nano* **2012**, *6*, 5845-5857.

[38] C. A. Shaw, G. M. Mortimer, Z. J. Deng, E. S. Carter, S. P. Connell, M. R. Miller, R. Duffin, D. E. Newby, P. W. F. Hadoke, R. F. Minchin, *Nanotoxicology* **2016**, 1-11.

[39] S.-D. Li, L. Huang, *Journal of Controlled Release* **2010**, *145*, 178-181.

[40] A. Salvati, A. S. Pitek, M. P. Monopoli, K. Prapainop, F. B. Bombelli, D. R. Hristov, P. M. Kelly, C. Aberg, E. Mahon, K. A. Dawson, *Nat Nano* **2013**, *8*, 137-143.

[41] aM. Hadjidemetriou, Z. Al-Ahmady, M. Mazza, R. F. Collins, K. Dawson, K. Kostarelos, *Acs Nano* **2015**, *9*, 8142-8156; bU. Sakulkhu, L. Maurizi, M. Mahmoudi, M. Motazacker, M. Vries, A. Gramoun, M.-G. Ollivier Beuzelin, J.-P. Vallee, F. Rezaee, H. Hofmann, *Nanoscale* **2014**, *6*, 11439-11450.

[42] aS. Rocha, A. F. Thünemann, M. d. C. Pereira, M. Coelho, H. Möhwald, G. Brezesinski, *Biophysical Chemistry* **2008**, *137*, 35-42; bK. Yokoyama, D. R. Welchons, *Nanotechnology* **2007**, *18*, 105101.
[43] S. Mirsadeghi, R. Dinarvand, M. H. Ghahremani, M. R. Hormozi-Nezhad, Z. Mahmoudi, M. J. Hajipour, F. Atyabi, M. Ghavami, M. Mahmoudi, *Nanoscale* **2015**, *7*, 5004-5013.
[44] M. Mahmoudi, A. Simchi, M. Imani, M. A. Shokrgozar, A. S. Milani, U. O. Häfeli, P. Stroeve, *Colloids and Surfaces B: Biointerfaces* **2010**, *75*, 300-309.
[45] Z. J. Deng, M. Liang, M. Monteiro, I. Toth, R. F. Minchin, *Nat Nano* **2011**, *6*, 39-44.
[46] aJ. E. Gagner, M. D. Lopez, J. S. Dordick, R. W. Siegel, *Biomaterials* **2011**, *32*, 7241-7252; bJ. Wang, U. B. Jensen, G. V. Jensen, S. Shipovskov, V. S. Balakrishnan, D. Otzen, J. S. Pedersen, F. Besenbacher, D. S. Sutherland, *Nano Letters* **2011**, *11*, 4985-4991.
[47] R. Podila, R. Chen, P. C. Ke, J. M. Brown, A. M. Rao, *Applied Physics Letters* **2012**, *101*, 263701.
[48] Y. H. P. Zhang, J. Hong, X. Ye, in *Biofuels: Methods and Protocols* (Ed.: R. J. Mielenz), Humana Press, Totowa, NJ, **2009**, pp. 213-231.
[49] S. Ding, A. A. Cargill, I. L. Medintz, J. C. Claussen, *Current Opinion in Biotechnology* **2015**, *34*, 242-250.

5 Drug delivery using silica particles produced by R5 silica precipitation

5.1 Introduction

5.1.1 Silica formation in diatoms

From the early days of microscopy, diatoms have been among the favorite groups of organisms for biologists to examine due to their beautiful cell walls and diverse intricate structures (Figure 41). Diatoms are eukaryotic unicellular microalgae with cell walls made of a composite of organic material and silica. Diatoms take up silicon from their environment as silicic acid and polymerize it into silica during the period of cell wall synthesis. The ornate shape that is the result of this process is called frustule and its regular shape hints at a tightly controlled formation of silica.

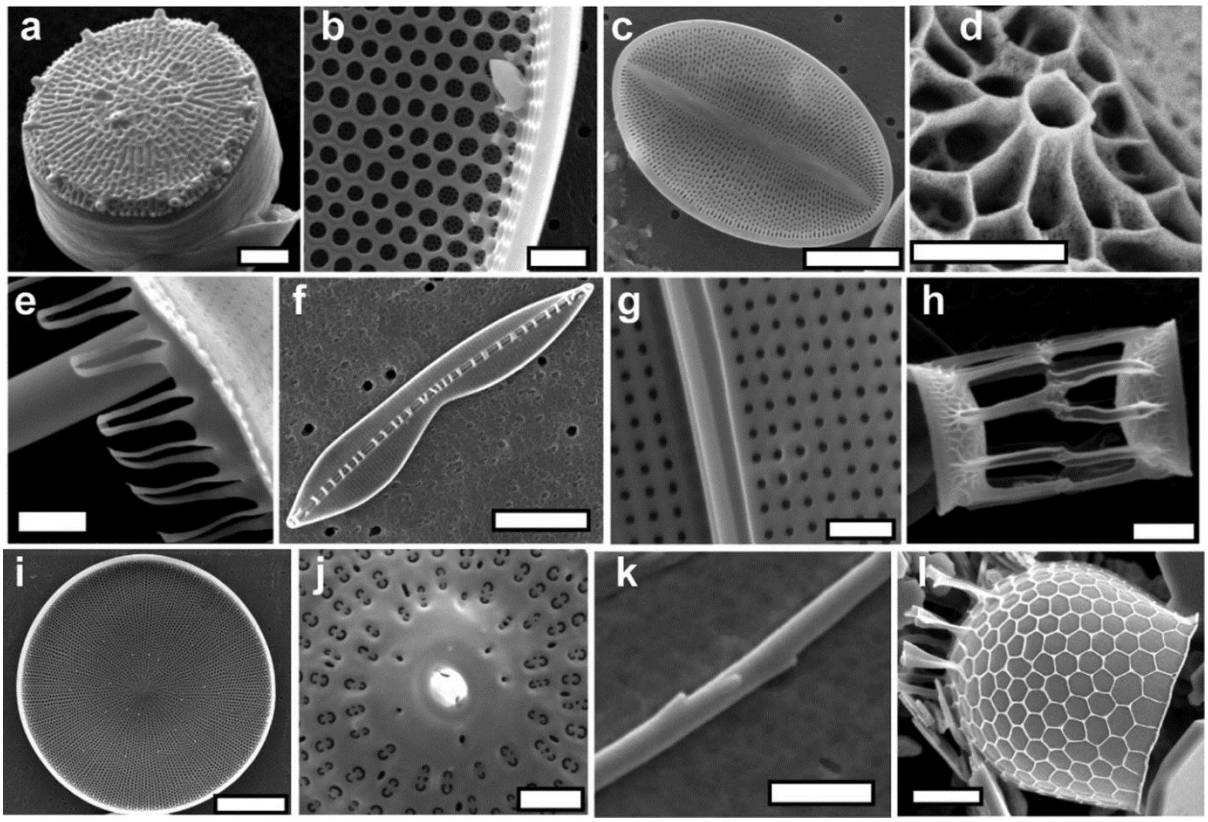

Figure 41: Diversity of diatom silica structures. SEM pictures of acid-cleaned material from (a)Thalassiosira pseudonana, bar = 1 µm, (b) close up of Coscinodiscus wailesii, bar = 5 µm, (c) Cocconeis sp., bar = 10 µm, (d) rimoportula from Thalassiosira weissflogii, bar = 500 nm, (e) corona structure of Ditylum brightwellii, bar = 2 µm, (f) Bacilaria paxillifer, bar = 10 µm, (g) close up of pores in Gyrosigma balticum, bar = 2 µm, (h) Skeletonema costatum, bar = 2 µm, (i) valve of C. wailesii, bar = 50 µm, (j) close up of pores in D. brightwellii, bar = 2 µm, (k) seta of Chaetoceros gracilis, bar = 1 µm, and (l) Stephanopyxis turris, bar = 10 µm. With permission from [1]

Diatoms are ubiquitously found all around the world in both marine and fresh water environments as long as sufficient amounts of nutrients are present. Overall there are more than 250 genera of living diatoms with an estimated 100,000 species, making them the second most diverse group of photosynthetic organisms after the angiosperms [2]. They are the most important group of eukaryotic phytoplankton, responsible for close to 40% of marine primary activity as well as for 20% of global carbon fixation [3].

Diatoms can be separated into two general structural types: centric and pennate [4]. Centric diatoms with a central symmetry center form circular shapes but more diverse forms that have a centric symmetry are also possible(Figure 41a,c,h,I,l). Pennate diatoms have an elongated form that has bilateral or even helical symmetry (Figure 41f).

The silica cell wall is constructed like a petri dish with the upper half (epitheca) overlapping the lower half (hypotheca). Both halves consist of an ornate cover (valve) while the curved sides of the lid are less ornate and called girdle bands. Each lid with its girdle bands form one half (theca) of the cell wall. The rigid nature of the frustule offers mechanical protection[5] and the frustules porous nature allows for nutrient uptake. There is evidence that pore size and form influence nutrient uptake in a selective way [6]. The frustule might also be involved in diatom interaction with surfaces as cleaned frustules adhere to smooth surfaces even under high flow pressure [7]. Frustules effect light as it enters the cells in multiple ways, possibly serving a photo-selective, photo-protective or light focusing role [8]. New diatoms are predominantly produced vegetatively, but sexual reproduction is possible as well. New silica walls are formed in special vesicles in the diatom called silica deposition vesicles (SDV). After the morphogenesis process the silica parts are deposited on the cell surface via exocytosis (Figure 42) [4].

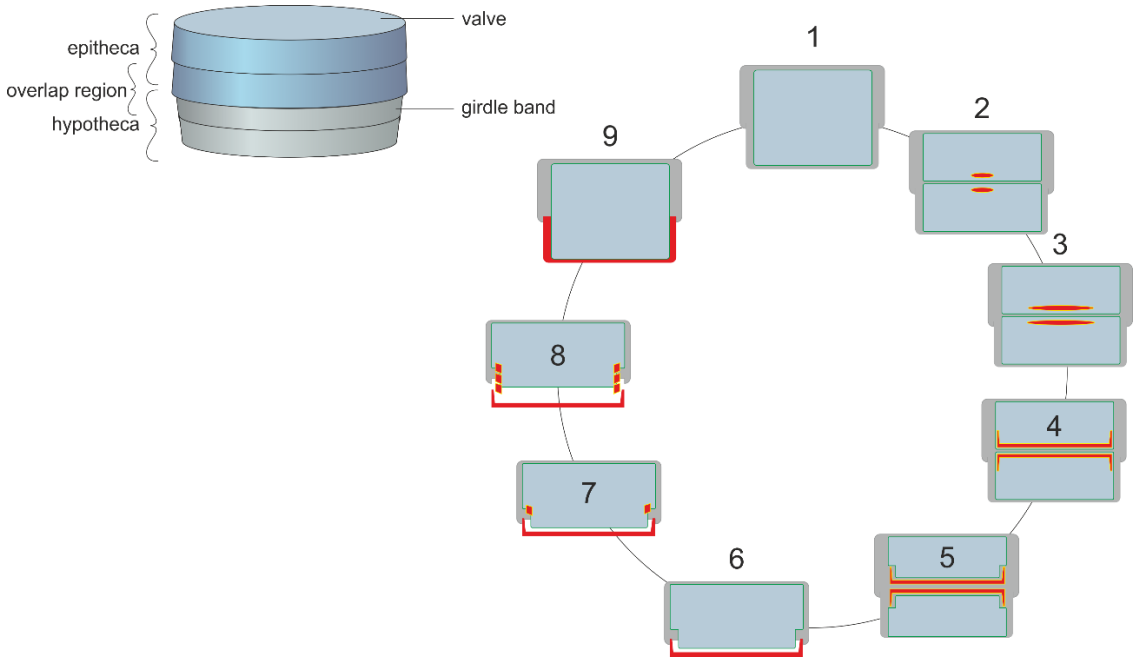

Figure 42: Schematic structure of the diatom cell (center) and diatom cell cycle. Diatom cells are shown in cross section. The gray area represents the protoplast, the green line depicts the plasma membrane. (1) Shortly before cell division the cell wall contains the maximum number of girdle bands; (2) immediately after cytokinesis new biosilica (red) is formed in each sibling cell inside a valve SDV (yellow); (3) expansion of the valve SDVs as more and more silica is deposited; (4) at the final stage of valve SDV development, each SDV contains a fully developed valve; (5) the newly formed valves are deposited in the cleavage furrow on the surface of each protoplast by SDV exocytosis; (6) the sibling cells have separated; (7+8) expansion of the protoplast in interphase requires the synthesis of new silica (red) inside girdle band SDVs (yellow); each girdle band is synthesized in a separate SDV, and after SDV exocytosis is added to the newly formed valve (hypovalve); (9) after synthesis of the final hypovalve girdle band (pleural band) cell expansion stops, and DNA replication is initiated. Scheme after [9]

The silica deposition vesicle is a distinct intracellular membrane bound compartment [1]. Its membrane, called the silica lemma consists of three layers that surround the growing silica structure [10]. Its lumen is more acidic than the rest of the cellular environment [11], a feature that most probably facilitates the polymerization of silica into a gel network that mechanically functions as a cohesive material [12]. SDV's originate most probably from the Golgi apparatus [13] but, despite vigorous efforts of isolating the organelle and further characterizing it, up till now this feat was not achieved. It has been proposed that the SDV also act as silicon transport vesicles, however, no evidence has ever been presented to underline this hypothesis [1]. The first step in the precipitation process demands the availability of silicic acid, the precursor to silica. Concentration of silicic acid in the environment of diatoms range from 10-70 µM in surface waters and oceans [14], but concentrations inside the SDV can range up to several hundred millimolar [15]. Silicic acid is transported actively into the cell via silicic acid transport proteins (SIT) as well as via passive diffusion [16]. The active transporter SIT is a protein consisting of 10 transmembrane helices and a highly conserved sequence motif of GXQ (X=Q,G,R or M) [17]. The proposed mechanism sees the highly conserved glutamine in the GXQ motif in two adjacent transmembrane domains binding and transporting silicic acid [18].

In order to understand the following process of silicification the detailed analysis of involved molecules is needed. It is most likely that the lumen of the SDV contains major players of the process. The inability to purify the SDV has, so far however, made evaluating involved molecules very hard, and only a few proteins could definitely be associated with frustule formation [19]. The best understanding of the process and its key players so far was delivered by Kröger *et al.* who took the silica frustule from *C. fusiformis*, vigorously removed all organic components from it and dissolved the frustule with hydrofluoric acid. The resulting solution was analyzed by gel electrophoresis and three distinct serine and lysine rich peptides at 4, 8 and 17 kDa could be identified. The purified material was able to precipitate silica from solution in very short time intervals. The three peptides were called silaffin-1A, -1B and -2 respectively [20]. The corresponding gene *sil1* could be cloned from a previously established cDNA library and a precursor protein, sil1p, with 265 amino acids (Figure 43) [21].

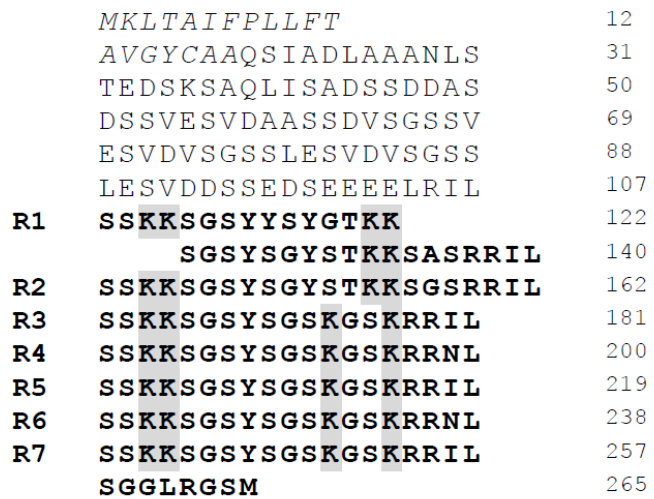

Figure 43: Primary structure of the silaffin precursor protein sil1p. The signal peptide 1-19 is shown in italics and the repetitive units R1-R7 in bold. The lysine clusters in the repetitive C-terminal parts are highlighted in grey [21].

The protein contains an N-terminal signal sequence for translocation into the endoplasmatic reticulum (amino acids 1-19) followed by an acidic N-terminal region of unknown function (amino acids 20-107). The units R1-R7 at the C-terminus are strongly basic and highly repetitive. In the mature forms of the protein the C-terminal RRIL and RRNL sequences are missing something that is consistent in other diatom associated proteins with similar RXL motifs. This hints at RXL as a general recognition motif for specific endopeptidases in diatoms that process precursor polypeptides by cleaving the RXL motif to release the individual peptides [20, 22]. Detailed chemical analysis of the silaffins revealed a peptide that has a surprising amount of extraordinary posttranslational modifications. The silaffin $1A_1$, which comprises of the R3-7 peptides for example has all lysine residues either di- or tri-methylated or coupled to a unique N-methylated oligopropylenimine modification (Figure 44) [21, 23]. A change of the extraction method from HF to acidic aqueous ammonium fluoride preserved more labile post-translational modifications proving that all serine hydroxyl groups are phosphorylated. In addition to that all trimethylated lysine residues are phosphorylated at the δ-position as well [24]. All of these modifications introduce a significant amount of positive and negative charges to the molecule making it a large zwitterionic molecule.

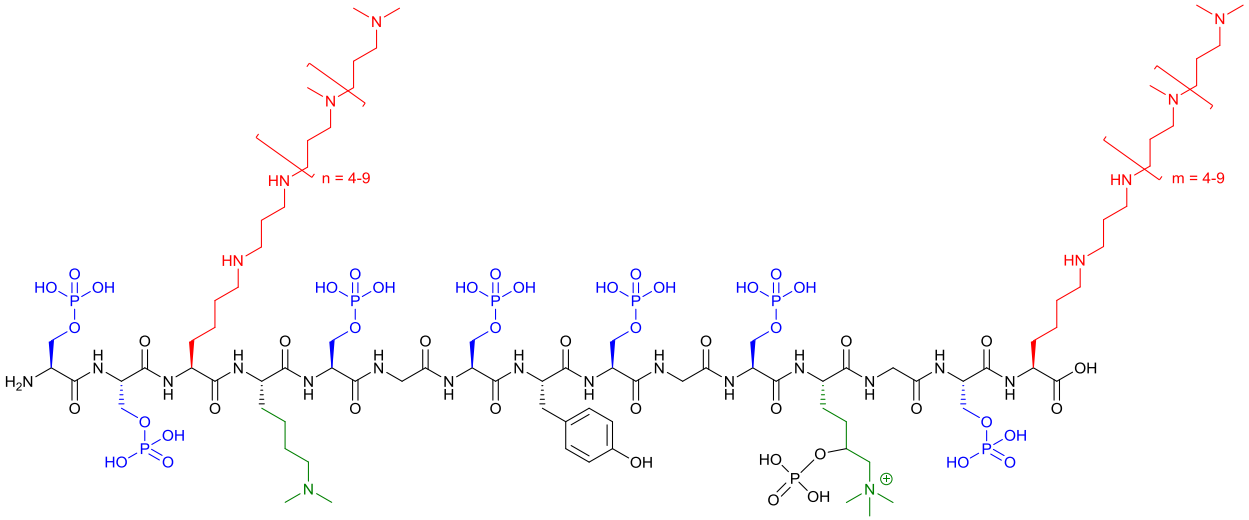

Figure 44: Chemical structure of silaffin-A_1 from C.fusiformis

Silaffins are capable of precipitating silica from a solution of silicic acid. Fully modified silaffin $1A_1$ precipitated silica at pH 5.5, whereas a silaffin 1A that lacks the serine phosphorylation, does not [23b]. Silaffin 1A precipitation ability can be restored by adding phosphate anions [24]. The R5 peptide, a synthetic silaffin variant based on the repetitive unit 5 of the sil1p without any post-translational modifications is able to precipitate silica at neutral pH in the presence of phosphate anions [25].

5.1.2 Chemical aspects of silica formation with R5

Silica precipitation is driven by a complex inorganic polymerization process with orthosilicic acids as monomeric building block. The solubility of monosilicic acid in water is limited at 2 mM at neutral pH, and a basic pH initiates deprotonation resulting in silicate anions. Nucleophilic substitution between the anions and the acid lead to condensation via the formation of siloxane bonds (Si-O-Si) [12]. This leads to dense, branched polysilicic acid species with sizes in the nanometer range. The exact morphology of these colloidal silica particles depends heavily on pH and salts present. Below pH 7 the electrostatic repulsion between the particles is weak and aggregation to fibrillary chains is possible resulting in a silica gel. From pH 7 on negative charges at the surface of the colloidal silica particles dominate, resulting in growing single particles [12, 26]. Cationic species such as polyamines however stabilize transition states of the condensation reaction, promoting flocculation [27].

Silaffins are zwitterionic due to their polyamine and phosphor modifications and self-assemble in solution with the phosphate groups serving as an intrinsic anion source [24]. R5, lacking the phosphorylation completely requires the addition of phosphate anions as cross linkers in the self-assembly process [24]. R5 also lacks the polyamine modifications but the present lysine residues step in to act as cationic species for the condensation reaction. Deprotonated amino groups accept a proton from a silicic acid molecule, resulting in the formation of a reactive silanolate group [27c]. During the nucleophilic attack of this group to a second silicic acid molecule, protonated amino groups facilitated the release of a water molecule from the attacked molecule by protonation [28]. The defined space between amino groups in peptides may help stabilize the transition state and help as pattering template. During this work a R5 with an additional N-terminal cysteine was used for possible further modification.

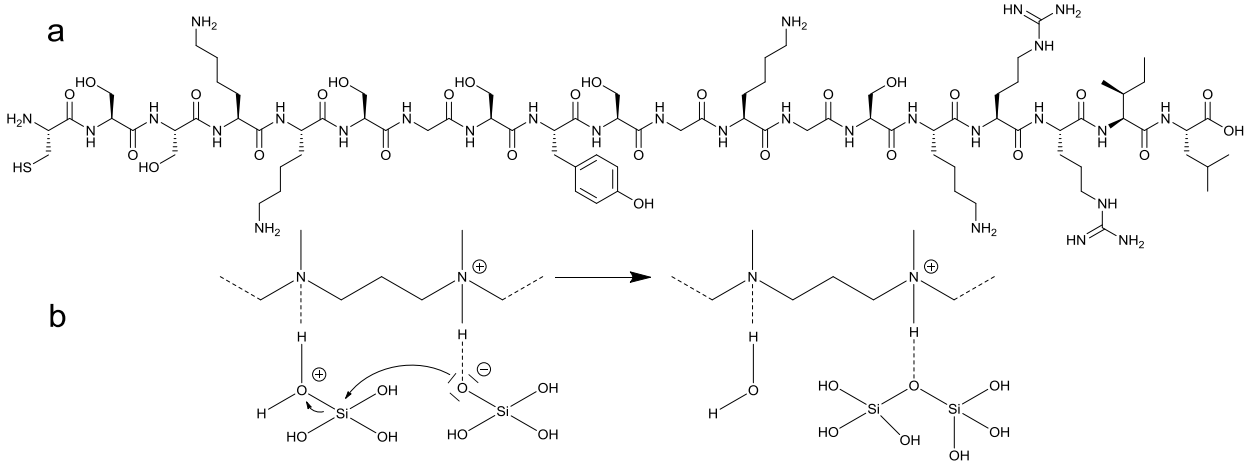

Figure 45: a) Chemical structure of R5-Cys; b) proposed mechanism for polyamine mediated condensation of silicic acid

5.1.3 Delivery with porous particles

Porous silica is a useful material for medical research due to its chemical inertness and biocompatibility. Naturally occurring porous silica materials such as zeolites however are excluded for medical research due to their small pore size, making it difficult to incorporate drugs or proteins into the material. Synthetic materials such as mesoporous silica with larger pores and synthetic routes that make it possible to fine tune the materials characteristics to the scientists needs made them very popular [29]. The loading of ibuprofen in mesoporous silica nanoparticles and the consecutive controlled release experiments garnered a lot of interest in this technique [30]. Common loading methods are either covalent linkage of the drug to the material [31] or simply soaking the particles in a solution of the drug, thus filling it with the drug like a sponge [32]. For the first a defined release chemistry, such as photo cleavage, is required for the latter loading efficiency as well as release is difficult to control [33]. Prevention of release of the drug before it reached its intended target could be achieved e.g. by sealing the pores by deposition of a lipid bilayer [34]. Other approaches of lids or "gatekeepers" as they are commonly referred have been introduced: Redox responsive systems that take advantage of the reductive environment during endocytosis [35], lactose gatekeepers that are enzymatically removed in the cell [36], pH sensitive hydrazine bonds that utilize the acidic pH in cancer cells [37] and azobenzene derivatives that are open via light induction [38].

The immobilization of enzymes within mesoporous silica materials is another application that is increasingly researched. Internalizing enzymes into the pore structure often not only retains the enzymatic activity but increases the stability versus debilitating effects, making these particles well suited biocatalysts [39]. Using self-assembly approaches such as R5 or polyethylenimine (POI), it is possible to introduce complete enzyme systems in one particle, including enzyme and cofactor in one single compartment [40]. Also multi-enzyme system can be produced to result in a hydrogen peroxide producing system as a biological anti fouling agent for ships [41].

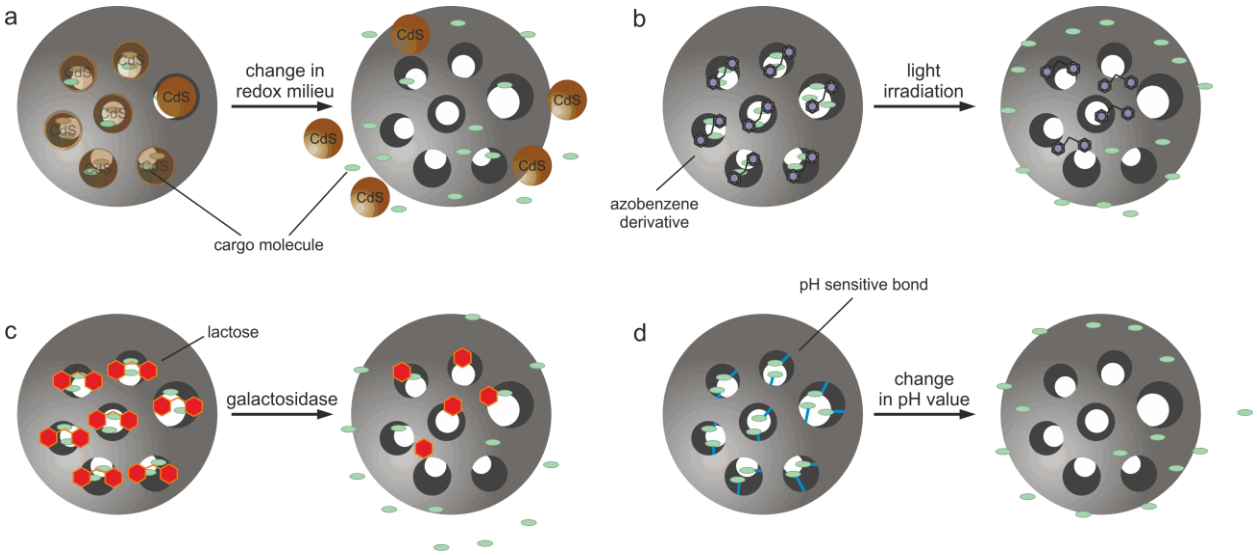

Figure 46: Controlled release of drugs from mesoporous silica nanoparticles. a) redox-responsive release of disulfide connected CdS [35]; b) light irradiation with azobenzene derivatives [38]; c) enzymatic degradation of the gatekeeper lactose via galactosidase [36]; d) pH dependent release [37]

Altogether the mesoporous silica nanoparticle approach is very promising indeed. Using controlled self-assembly methods such as R5 or POI it is possible to overcome the drawbacks of complicated syntheses and harsh reaction conditions that are normally associated with standard mesoporous silica particles. Using this approach it is also possible to design microfluidic reactors with silica immobilized nitrobenzene nitroreductase for screening for cancer prodrug activation [42]. Controlled formation and entrapment of molecules in mesoporous silica particles therefor is a superior method compared to random entrapment [43].

5.1.4 Aim

Building on work previously carried out in our group, we aim to use R5 mediated silica precipitation as a method to produce self-assembled silica particles [44]. Due to the nature of the precipitation process the R5 peptide is entrapped in the particles in large quantities resulting in a particle preloaded with the R5 peptide. Lechner *et.al.* showed that attachment of bulky molecules such as GFP to the R5 peptide does not necessarily hinder the precipitation process resulting in a particle loaded with the molecule of choice [43]. Release over time in a pH dependent manner was shown for R5 and R5 coupled to small peptides. Attaching a molecule of interest to the peptide results in its entrapment along with the R5 peptide itself in the silica particle, producing an easy to use self-assembling system to produce loaded silica particles at mild reaction conditions (Figure 47).

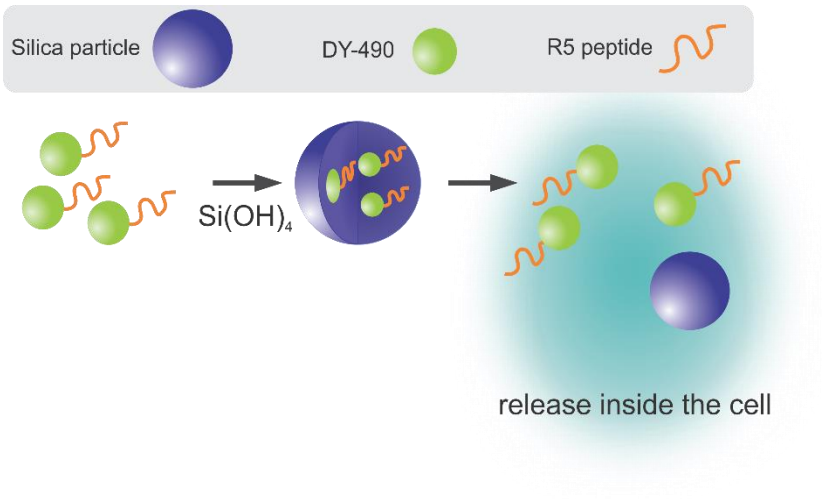

Figure 47: Scheme of the R5 delivery concept. R5, fused to a fluorescence label (DY-490) is used to precipitate silica particles and is internalized in the particle in the process. Upon entering the cytoplasm of cancer cells, the lowered pH will accelerate leaking of the R5-DY-490 conjugate into the cytoplasm.

For this work a modified R5 variant with an additional N-terminal cysteine (R5-Cys) was used for possible future modification. In this work optimizations of the already published precipitation procedure will be tested, especially in regard to replace the toxic TMOS with the less toxic TEOS. In addition we will have a look at the interaction and possible internalization of the particles into HT-29 colon cancer cells by using particles produced with fluorescence labeled R5-Cys. The precise uptake mechanism of silica microparticles is so far not understood. Nanoparticles are reported to enter cells most likely via endocytosis [45], whereas data for silica microparticles is only available for endothelia and macrophages, where phagocytic pathways are proposed as responsible for uptake [46]. Observation of uptake might provide information on which pathway might be involved.

5.2 Material and Methods

5.2.1 Chemicals

If not otherwise noted all chemicals were purchased from Sigma Aldrich, St. Louis, Missouri, USA. All amino acids were bought from Novabiochem, Darmstadt, Germany. Life cell imaging solution and CellMask plasma membrane stain, HOECHST DNA stain and all media were purchased from Thermo Fischer Scientific, Waltham, MA, USA. HT-29 cells were acquired from the DSMZ-Deutsche Sammlung von Mikroorganismen und Zellkulturen GmbH, Braunschweig, Germany.

5.2.2 Devices

Electron scanning microscopy was done using a Zeiss Supra 55 VP ESEM from Carl Zeiss AG, Oberkochen, Germany. All peptides, if not otherwise mentioned, were synthesized using a Liberty Blue microwave peptide synthesizer from CEM Corporation Matthews, NC, USA. Fluorescence microscopy was done using an ELYRA PS.1 and LSM 710 from Carl Zeiss AG, Oberkochen, Germany. HPLC analysis was done using a DIONEX Ultimate 3000 µHPLC System from Thermo Fischer Scientific Inc., Waltham, Massachusetts, USA using C4 analytical columns from Sigma Aldrich, St. Loius, Missouri, USA. Mass spectrometry analysis as well as peptide purification was done using an Auto Purification HPLC/MS system from Waters Corporation AG, Wilford, Massachusetts USA and preparative Kromasil C18 HPLC columns (250 x 21.2 mm, 5 µm particle size) from Sigma Aldrich, St. Loius, Missouri, USA. Additional mass spectrometric analysis was done using an Autoflex Speed MALDI-TOF mass spectrometer and a MAXIS Q-TOF from Bruker, Billerica, MA, USA.

5.2.3 R5-Cys peptide synthesis

Synthesis of the R5-Cys peptide was accomplished using fluorenylmethoxycarbonyl (Fmoc) chemistry on preloaded Wang-polystyrene resin in 0.1 or 0.2 mmol scale. The Fmoc-amino acids contained the following side chain protecting groups: Arg(Pbf), Lys(Boc), Ser(tBu) and Tyr(tBu). The pseudo-proline dipeptide Fmoc-Gly-Ser($\psi^{Me,Me}$pro)-OH was used at suitable positions to improve synthesis yields. Fmoc deprotection was achieved with 20% piperidine in DMF and amino acids were coupled using OXIMA and DIC). Peptides were globally deprotected and cleaved from dried resin with a mixture of TFA, triisopropylsilane and water (92.5 : 5 : 2.5) for 4 h at RT. Precipitation of crude peptides was achieved by addition of three volumes of cold diethyl ether followed by centrifugation. After washing with ether twice, precipitated peptides were dissolved in water and lyophilized. R5-Cys was purified using an Auto Purification HPLC/MS system from Waters Corporation and C4 preparative column from Kromasil (250 x 21.2 mm, 5 µm particle size)

5.2.4 Fluorescence labeled R5-Cys

Deprotected R5-Cys peptide on Wang-polystyrene resin was pre-swollen in DMF for 30 minutes. DY490 fluorescence dye with NHS ester functional group was dissolved in DMF with 4 equivalents of DIEA and added to the swollen resin. The resulting mixture was shaken overnight in the dark. The resulting modified peptide was cleaved from the resin using the same procedure as discussed in chapter 5.2.3 with no modifications. Fluorescent labeled peptide was purified using a DIONEX Ultimate 3000 µHPLC System and an analytical C18 column from Kromasil (150 x 4.6 mm, 5 µm particle size)

5.2.5 Silica precipitation assay

For silica precipitation experiments the silicic acid needs to be produced freshly every experiment. For this tetramethylorthosilicate (TMOS) is added to 1 mM HCl in a 1:9 (vol/vol) ratio, homogenized via vigorous shaking and incubated for at least 4 minutes. This silicic acid solution is added to a 100 mM R5-Cys solution in 50 mM potassium phosphate buffer at pH 7 to a ratio of 1:10 (vol/vol). The reaction mixture is incubated at RT for 30 min and precipitating silica was removed via centrifugation. The final product was washed with water three times.

5.2.6 Cell culture experiments.

HT 29 cells were cultivated in DMEM with 1 % penicillin and streptavidin and 10 % FBS. They were incubated for 96 h. Particles were added to life cell imaging solution containing 10% FBS to a final concentration of 100 µg particles per ml. The mixture was vigorously shaken and sonicated for 4 min. The particle mixture was added to the cells in medium in a 1:1 (v/v) particle suspension to cell culture ratio. Dyes were added prior to imaging according to the manufacturer's instructions.

5.3 Results

5.3.1 Silica precipitation experiments

The procedure of silica precipitation using the R5 peptide was established by coworkers in 2012 [44]. In our work we found a negative influence of changes in salt concentration as well as the presence of sodium ions. Use of sodium phosphate buffer instead of potassium phosphate buffer resulted in a loss of controlled precipitation, only powdery silica precipitated (grain size > 5 nm) (Figure 48b). An increase of salt concentrations by a factor of 10 resulted in a loss of precipitating activity as well (Figure 48d). Only well-defined cubic potassium phosphate crystals could be found in the sample.

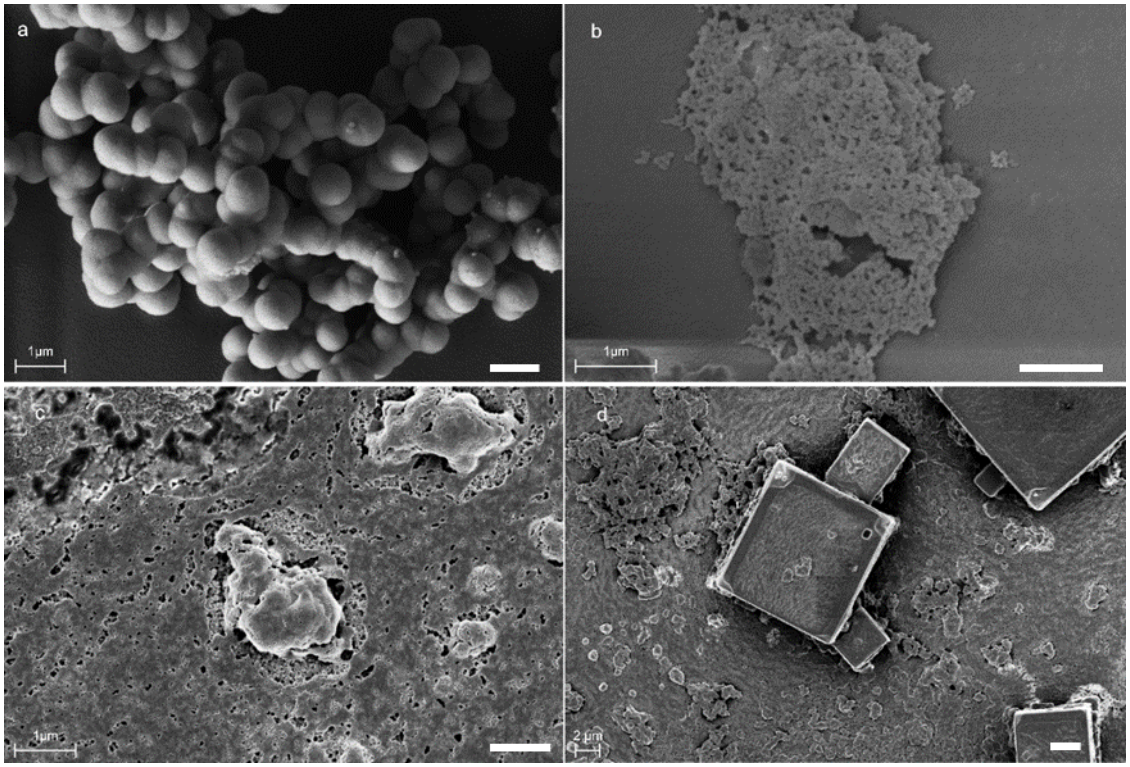

Figure 48: ESEM pictures of precipitation experiments using R5-Cys a) standard procedure b) Using sodium phosphate buffer instead of potassium phosphate buffer c) using TEOS instead of TMOS d) 10 times buffer concentration

In addition to the aforementioned observations we tried to exchange tetramethylorthosilicate (TMOS) with tetraethylorthosilicate (TEOS) due to the high toxicity of TMOS. Experiments using TEOS in identical concentrations to TMOS showed no precipitation at all in the observed time frame. Only salt crystals and gold surface grain from sample preparation could be observed (Figure 48c). Coworkers were able to discover prolonged precipitation times of 48 h or more resulted in some precipitation (data not shown).

5.3.2 Cell cultures experiments with R5-Cys-DY490

For tracking R5-Cys particles in cell culture experiments a R5-Cys variant labeled with a fluorescent dye DY490 was produced using the dye and common NHS ester chemistry. DY490 absorbs light at 491 nm and emits in the green fluorescence spectrum at 515 nm. The fluorescence labeled peptide was then used to precipitate silica particles with the R5-Cys-DY490 peptide conjugate entrapped in it. ESEM measurements as well as fluorescence microscopy pictures showed that the DY490 dye did not prevent the silica particles from forming and the resulting particles were fluorescently active (Figure 49). Slight differences seen in the ESEM of the R5-Cys-DY490 particles are due to random salt precipitations in the frame (see Figure 48c and d)

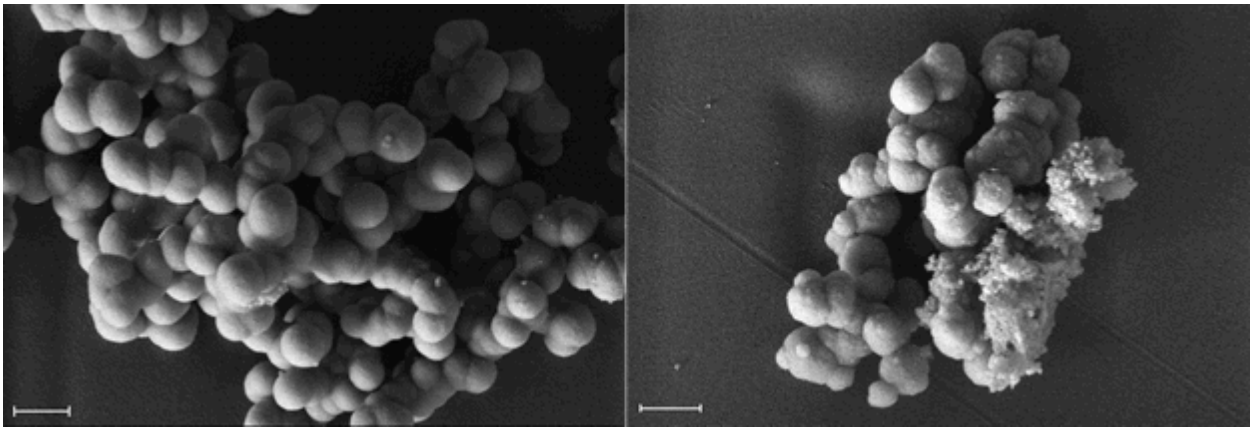

Figure 49: Comparison of R5-Cys precipitated particles (left) versus R5-Cys-DY490 fluorescence labeled peptide precipitated particles (right). Particles show the same morphology and size as the particles produced using the unlabeled R5-Cys peptide. Scale bars = 1µm

The resulting fluorescent particles were then administered to HT-29 cells and monitored for at least 24 hours via fluorescence microscopy.

In order to verify whether the R5-Cys peptide itself is able to enter HT-29 cells, we administered the R5-Cys-DY490 peptide conjugate to the cells and monitored the distribution of the conjugate via fluorescence microscopy for 24h. In the given timeframe no internalization of the peptide could be found in detectable levels (Figure 50). The peptide seems to accumulate at the bottom of the container forming a carpet of fluorescence. This carpet is situated around the cells and no fluorescence was found in or above the cells. In some rare cases however some nuclei exhibited a high amount of green fluorescence, indicating uptake of the peptide conjugate in the nucleus. Cells with subjected nuclei did however show absent or malformed cell walls indicating an apoptotic cell and interaction of the highly charged R5-Cys peptide with the negatively charged DNA of the nucleus. Healthy cells did not show any internal fluorescence even after 7 h of incubation.

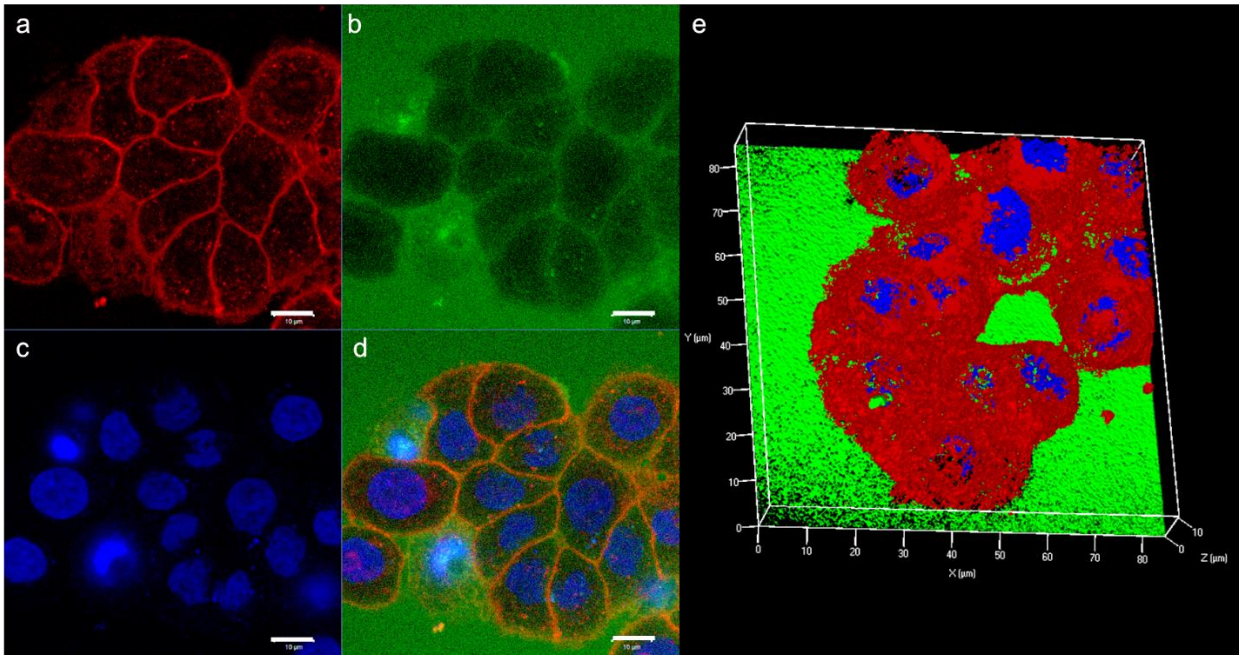

Figure 50: Fluorescence microscopy picture of HT-29 cells incubated with R5-Cys-DY490 peptide. a) CellMask plasma membranel staining. b) DY490 Fluorescence. c) HOECHST DNA staining of the cell nucleus. d) overlay of all channels. e) 3D view of the cells at 7 h incubation time. The fluorescence is still only detectable at the bottom of the dish but not in the cells on higher levels. Scale bars = 10µm

Incubating HT-29 cells with the R5-Cys-DY490 fluorescent silica particles showed a similar initial behavior as observed with the peptide conjugate itself. The particles gather in the free spaces between the cells, seldom on top of the cells or in them (Figure 51a). There seems to be no affinity of the particles towards the HT29 cell surface. After six hours incubation the first silica particles could be observed entering the cells. Directly after internalization of the particle into the cell diffuse fluorescence appears around the internalized particles. This hints at increased diffusion of the peptide in the more acidic environment of the cancer cells cytoplasm. No diffusion of peptide in the medium is observable at this time (Figure 51b). After 24 hours the amount of particles found in HT29 cells increased. Fluorescence signals are now observable in the whole cytoplasm with highest signal intensities around the particles. In the case of cells with multiple particles in the cytoplasm these particles seem to have a high tendency to aggregate in a similar fashion as observed in the medium. Again, no diffusion of fluorescent labeled peptide is observed in the medium (Figure 51c). This might however, be due to a higher diffusion of possible leaking peptide in the large volume of the medium versus the smaller contained volume of cellular cytoplasm. In some cases the leaking of peptide seems to happen in a locally concentrated way, pushing visible cell compartments like the nucleus out of their way and even deforming them to make room for the growing fluorescence sphere (Figure 51d). This might indicate that the particles are taken up via endocytic vesicles, consecutive diffusion of peptide in the vesicle results in its increase in size.

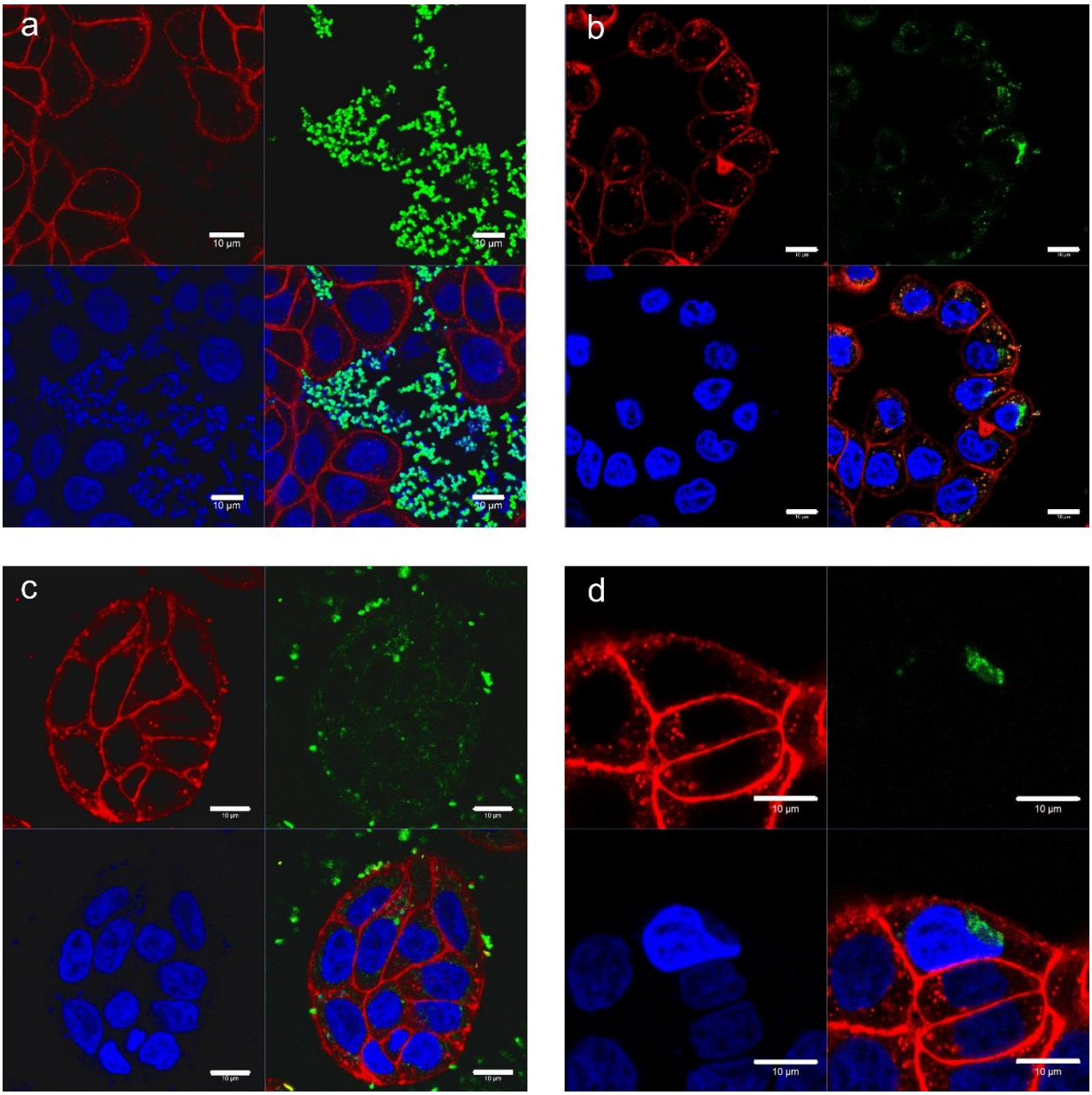

Figure 51: Samples of silica particle internalization in HT-29 cells. a) after 5 minutes. Particles are distributed in the cell free parts of the container and not to be found on top of the particles. b) after 6h incubation time. Particles start to internalize in the cells and are mostly located in the cells. c) after 24h incubation time. Particles are internalizing in the cells more and more and some clear diffuse fluorescence is found in the cells indicating leakage of the peptide into the cytoplasm. d) close up of a HT-29 cell after 12h incubation time. The particles are producing a diffuse strong area of fluorescence that pushed the nucleus back. Red Channel: CellMask plasma membrane staining. Blue channel: HOECHST DNA staining of the cell nucleus. Green: DY490 Fluorescence. Scalce bar = 10µm

Uptake is however not uniform, a majority of cells did not show any fluorescence signal at all even after 48 h. This might be due to loss of fluorescence signal of the particles. Beside the incubation time no clear indicator could be found as to why and when the cells do take the particles up.

5.4 Conclusion

We were able to synthesize the R5-Cys peptide, as well as its fluorescence labeled variant. The precipitation of silica particles using the established precipitation protocol was successful. Modifications of the R5-Cys peptide with the fluorescence dye DY-490 did not influence the precipitation process in any way. Using the R5-Cys peptide with or without DY-490 produces defined spherical silica particles with an average diameter of 800-900 nm. The precipitation is hindered by high salt concentrations as well as sodium ions in the precipitation mixture. Tetraethylorthosilicate unfortunately is no suitable substitute for the highly toxic tetramethylorthosilicate for silicic acid production. We were able to produce fluorescence labeled particles using R5-Cys covalently coupled to the fluorescence dye DY-490.

The fluorescence labeled particles were able to enter HT-29 colon cancer cells. Where the peptide itself does not enter HT-29 colon cancer cells it was shown that fluorescence labeled silica particles do. After six hours of incubation the silica particles enter the HT-29 cells successfully and start accumulating in the cells. From the time they enter the cells they start to leak peptide into the cytoplasm, an effect that could not be observed in medium even after 48 hours. Leakage of peptide into the medium might however be difficult to detect due to the high dilution the leaked peptide is subjected to. Longer incubation times resulted in an increase in fluorescence signal in cells that internalized the silica particles showing high, diffuse fluorescence all over the cytoplasm after 24 hours. Incidents of localized fluorescence diffusion in small circular compartments in the cytoplasm indicate an endocytic pathways responsible for the uptake of the particles. In summary we established a promising model of drug delivery with a controlled pH dependent release of the drug in the cell over several hours. Future work will have to focus on selectivity of the model as well as understanding the release mechanism in more detail to be able to tweak it.

5.5 Literature

[1] M. Hildebrand, *Chemical Reviews* **2008**, *108*, 4855-4874.

[2] C. Hoek, D. Mann, H. M. Jahns, *Algae: an introduction to phycology*, Cambridge university press, **1995**.

[3] P. G. Falkowski, R. T. Barber, V. Smetacek, *Science* **1998**, *281*, 200-206.

[4] F. E. Round, R. M. Crawford, D. G. Mann, *Diatoms: biology and morphology of the genera*, Cambridge University Press, **1990**.

[5] C. E. Hamm, R. Merkel, O. Springer, P. Jurkojc, C. Maier, K. Prechtel, V. Smetacek, *Nature* **2003**, *421*, 841-843.

[6] D. Losic, G. Rosengarten, J. G. Mitchell, N. H. Voelcker, *Journal of Nanoscience and Nanotechnology* **2006**, *6*, 982-989.

[7] K. S. Kopanska, B. Tesson, H. Lin, J. C. Meredith, M. Hildebrand, A. Davis, *Silicon* **2014**, *6*, 95-107.

[8] aT. Fuhrmann, S. Landwehr, M. El Rharbi-Kucki, M. Sumper, *Applied Physics B* **2004**, *78*, 257-260; bJ. Noyes, M. Sumper, P. Vukusic, *Journal of Materials Research* **2008**, *23*, 3229-3235; cS. Yamanaka, R. Yano, H. Usami, N. Hayashida, M. Ohguchi, H. Takeda, K. Yoshino, *J Appl Phys* **2008**, *103*, 074701.

[9] N. Kröger, N. Poulsen, A. K, K. P. P, G. A, *Annual Review of Genetics* **2008**, *42*, 83-107.

[10] B. E. F. Reimann, J. C. Leivin, B. E. Volcani, *Journal of Phycology* **1966**, *2*, 74-84.

[11] E. G. Vrieling, W. W. C. Gieskes, T. P. M. Beelen, *Journal of Phycology* **1999**, *35*, 548-559.

[12] R. K. Iler, *The chemistry of silica: solubility, polymerization, colloid and surface pro perties, and biochemistry*, Wiley, **1979**.

[13] J. Pickett-Heaps, A.-M. M. Schmid, L. A. Edgar, *Progress in phycological research* **1990**, *7*, 1-168.

[14] P. Tréguer, *Comptes Rendus Geoscience* **2002**, *334*, 3-11.

[15] V. Martin-Jézéquel, M. Hildebrand, M. A. Brzezinski, *Journal of Phycology* **2000**, *36*, 821-840.

[16] aM. Hildebrand, B. E. Volcani, W. Gassmann, J. I. Schroeder, *Nature* **1997**, *385*, 688-689; bK. Thamatrakoln, M. Hildebrand, *Plant Physiology* **2008**, *146*, 1397-1407.

[17] K. Thamatrakoln, A. J. Alverson, M. Hildebrand, *Journal of Phycology* **2006**, *42*, 822-834.

[18] P. Curnow, L. Senior, M. J. Knight, K. Thamatrakoln, M. Hildebrand, P. J. Booth, *Biochemistry* **2012**, *51*, 3776-3785.

[19] A. K. Davis, M. Hildebrand, B. Palenik, *Journal of Phycology* **2005**, *41*, 577-589.

[20] N. Kröger, C. Bergsdorf, M. Sumper, *European Journal of Biochemistry* **1996**, *239*, 259-264.

[21] N. Kröger, R. Deutzmann, M. Sumper, *Journal of Biological Chemistry* **2001**, *276*, 26066-26070.

[22] aA. Scheffel, N. Poulsen, S. Shian, N. Kröger, *Proceedings of the National Academy of Sciences* **2011**, *108*, 3175-3180; bS. Wenzl, R. Hett, P. Richthammer, M. Sumper, *Angewandte Chemie International Edition* **2008**, *47*, 1729-1732.

[23] aN. Kröger, R. Deutzmann, C. Bergsdorf, M. Sumper, *Proceedings of the National Academy of Sciences* **2000**, *97*, 14133-14138; bN. Kröger, R. Deutzmann, M. Sumper, *Science* **1999**, *286*, 1129-1132.

[24] N. Kröger, S. Lorenz, E. Brunner, M. Sumper, *Science* **2002**, *298*, 584-586.

[25] M. R. Knecht, D. W. Wright, *Chemical Communications* **2003**, 3038-3039.

[26] W. Ostwald, *Zeitschrift für physikalische Chemie* **1897**, *22*, 289-330.

[27] aT. Coradin, O. Durupthy, J. Livage, *Langmuir* **2002**, *18*, 2331-2336; bK. M. Delak, N. Sahai, *Chemistry of materials* **2005**, *17*, 3221-3227; cT. Mizutani, H. Nagase, N. Fujiwara, H. Ogoshi, *Bulletin of the Chemical Society of Japan* **1998**, *71*, 2017-2022.

[28] S. Mann, P. Behrens, E. Bäuerlein, *Handbook of biomineralization: Biomimetic and bioinspired chemistry, Vol. 2*, John Wiley & Sons, **2009**.

[29] aJ. Beck, J. Vartuli, W. J. Roth, M. Leonowicz, C. Kresge, K. Schmitt, C. Chu, D. H. Olson, E. Sheppard,

Journal of the American Chemical Society **1992**, *114*, 10834-10843; bC. Kresge, M. Leonowicz, W. Roth, J. Vartuli, J. Beck, *nature* **1992**, *359*, 710-712.
[30] M. Vallet-Regi, A. Ramila, R. Del Real, J. Pérez-Pariente, *Chemistry of Materials* **2001**, *13*, 308-311.
[31] aR. Mortera, J. Vivero-Escoto, I. I. Slowing, E. Garrone, B. Onida, V. S.-Y. Lin, *Chemical Communications* **2009**, 3219-3221; bA. Schlossbauer, D. Schaffert, J. Kecht, E. Wagner, T. Bein, *Journal of the American Chemical Society* **2008**, *130*, 12558-12559.
[32] C. Charnay, S. Bégu, C. Tourné-Péteilh, L. Nicole, D. Lerner, J.-M. Devoisselle, *European Journal of Pharmaceutics and Biopharmaceutics* **2004**, *57*, 533-540.
[33] A. Nieto, M. Colilla, F. Balas, M. a. Vallet-Regí, *Langmuir* **2010**, *26*, 5038-5049.
[34] aV. Cauda, H. Engelke, A. Sauer, D. Arcizet, C. Bräuchle, J. Rädler, T. Bein, *Nano Letters* **2010**, *10*, 2484-2492; bS. A. Mackowiak, A. Schmidt, V. Weiss, C. Argyo, C. von Schirnding, T. Bein, C. Bräuchle, *Nano Letters* **2013**, *13*, 2576-2583.
[35] C.-Y. Lai, B. G. Trewyn, D. M. Jeftinija, K. Jeftinija, S. Xu, S. Jeftinija, V. S. Y. Lin, *Journal of the American Chemical Society* **2003**, *125*, 4451-4459.
[36] A. Bernardos, E. Aznar, M. D. Marcos, R. Martínez-Máñez, F. Sancenón, J. Soto, J. M. Barat, P. Amorós, *Angewandte Chemie International Edition* **2009**, *48*, 5884-5887.
[37] C.-H. Lee, S.-H. Cheng, I. P. Huang, J. S. Souris, C.-S. Yang, C.-Y. Mou, L.-W. Lo, *Angewandte Chemie International Edition* **2010**, *49*, 8214-8219.
[38] S. Angelos, E. Choi, F. Vögtle, L. De Cola, J. I. Zink, *The Journal of Physical Chemistry C* **2007**, *111*, 6589-6592.
[39] aH. R. Luckarift, J. C. Spain, R. R. Naik, M. O. Stone, *Nat Biotech* **2004**, *22*, 211-213; bR. R. Naik, M. M. Tomczak, H. R. Luckarift, J. C. Spain, M. O. Stone, *Chemical Communications* **2004**, 1684-1685.
[40] L. Betancor, C. Berne, H. R. Luckarift, J. C. Spain, *Chemical Communications* **2006**, 3640-3642.
[41] J. B. Kristensen, R. L. Meyer, C. H. Poulsen, K. M. Kragh, F. Besenbacher, B. S. Laursen, *Green Chemistry* **2010**, *12*, 387-394.
[42] C. Berne, L. Betancor, H. R. Luckarift, J. C. Spain, *Biomacromolecules* **2006**, *7*, 2631-2636.
[43] C. C. Lechner, C. F. W. Becker, *Biomaterials Science* **2015**, *3*, 288-297.
[44] C. C. Lechner, C. F. W. Becker, *Chemical Science* **2012**, *3*, 3500-3504.
[45] J. REJMAN, V. OBERLE, I. S. ZUHORN, D. HOEKSTRA, *Biochemical Journal* **2004**, *377*, 159-169.
[46] R. E. Serda, J. Gu, R. C. Bhavane, X. Liu, C. Chiappini, P. Decuzzi, M. Ferrari, *Biomaterials* **2009**, *30*, 2440-2448.

5.6 Appendix

5.6.1 R5-Cys synthesis data

R5-Cys was synthesized using standard SPPS procedures with a Liberty Blue peptide synthesizer
R5-Cys was purified by RP-HPLC using a preparative C4, 20 mL/min flow rate, 5 % to 65 % buffer B (ACN + 0.08 % TFA) in buffer A (ddH20 + 0.1 % TFA) in 40 min, yielding R5-Cys (39 % yield).

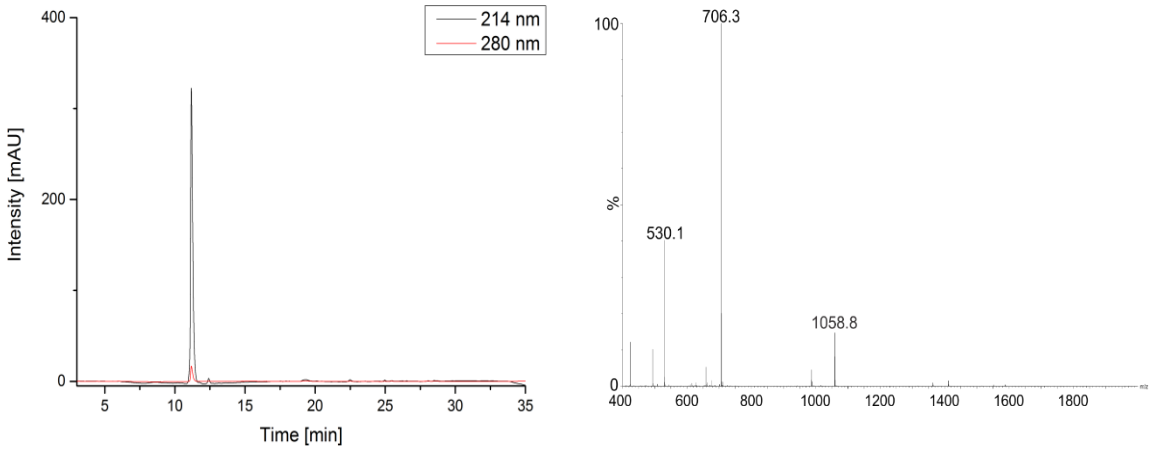

Figure 52: Analytical RP-HPLC spectrum of R5-Cys; right) ESI-MS spectrum of R5-Cys with a calculated mass of $[M+H]^{+}$ = 2116.14, $[M+2H]^{2+}$ = 1058.07 and $[M+3H]^{3+}$ = 705.38, $[M+4H]^{4+}$ = 529.03

5.6.2 R5-Cys-DY490 synthesis data

R5-Cys-DY490 was synthesized using standard SPPS procedures with a Liberty Blue peptide synthesizer. DY-490 was attached via standards NHS-ester chemistry on resin. R5-Cys-DY490 was purified by RP-HPLC using an analytical C4, 1 mL/min flow rate, 5 % to 65 % buffer B (ACN + 0.08 % TFA) in buffer A (ddH20 + 0.1 % TFA) in 30 min, yielding R5-Cys-DY490 (8.5 % yield).

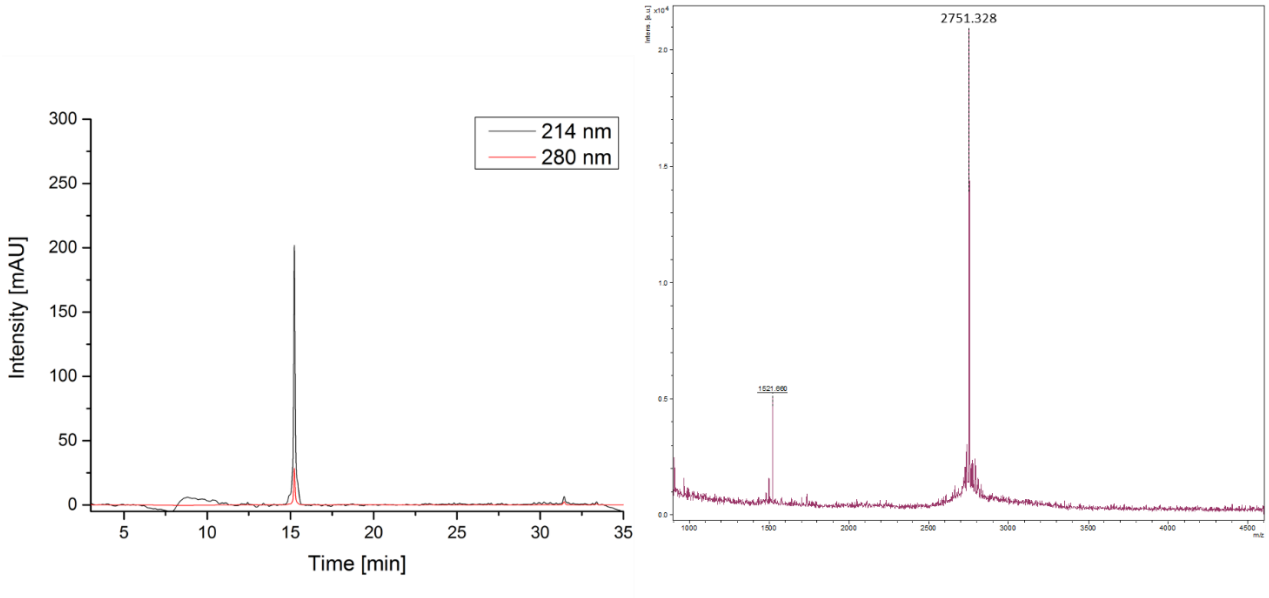

Figure 53: Analytical RP-HPLC spectrum of R5-Cys-DY490; right) negative mode MALDI-TOF spectrum of R5-Cys-DY490 with a calculated mass of $[M-H]^-$ = 2753.15